A New Limit on the Flux of Cosmic Antihelium

宇宙線反ヘリウムの流束における新しい制限

佐伯学行

①

A New Limit on the Flux of Cosmic Antihelium

By
Takayuki Saeki

Department of Physics, Faculty of Science,
University of Tokyo

1996

Abstract

This dissertation describes the search for antihelium in cosmic rays by the analysis of the data obtained from the three balloon flights of BESS[1] which were performed in 1993, 1994, and 1995. In the analysis, events with a single track in the tracking chamber were selected and identification of heliums and antiheliums were based on the measurements of magnetic rigidity, time of flight, and energy loss in the plastic scintillators. The selected events were further checked on the quality of data, especially the tracking qualities, and also on the consistency among the responses from the different detectors. After these careful checks and the quality requirements, no antihelium candidate was found below rigidity of 16 GV. Taking into account the detector efficiencies and the absorption of antiheliums and heliums in the air and the instrument, this analysis sets a 95% confidence level upper limit on the $\overline{\mathrm{He}}/\mathrm{He}$ flux ratio of 2.0×10^{-6} at the top of the atmosphere in the rigidity region from 1 to 16 GV, which is equivalent to a region from 0.14 to 7 GeV per nucleon in terms of kinetic energy. This result is about a factor of 45 improvement over the previous best limit by Golden et al.

[1]Balloon-borne Experiment with a Superconducting magnet rigidity Spectrometer

Contents

List of Tables

List of Figures

Chapter 1

Introduction

The existence of antimatter was first proposed by Dirac in the early 1930s [1] from relativistic quantum mechanical considerations. It was clear from his argument that all the particles in the world should have corresponding antiparticles. Following the discovery of positrons by Anderson [2] and antiprotons by Chamberlain and Segre [3], now it is well known that every elementary particle has its antiparticle. At the accelerators it was found that antiprotons and antineutrons indeed form antideuterons [4, 5, 6, 7, 8].

According to the current understanding of Big Bang, at the very beginning of the Universe there should have been the same amount of matter and antimatter. If this is correct, it seems rather accidental that the Earth is composed of negative electrons and positive protons. It is even conceivable that stars composed of positrons and antiprotons exist in the Universe. Thus, it is a mystery that antimatter such as antihelium and heavier antinuclei have not been observed in cosmic rays.

In the modern grand unified theories (GUTs), the matter-antimatter asymmetry in the present Universe, which is equivalent to the baryon-antibaryon asymmetry, is conventionally explained by the difference in the decay characteristics between X-particle and its antiparticle in the early universe. X-particle is a boson whose existence is predicted by the GUTs. X-boson has mass M_X of $\sim 10^{15}$ GeV and carries the forces between quarks and leptons. It can mediate reactions like the proton decay (e.g., $p \to e^+\pi^0$) with a proton lifetime of order of $\tau_p \geq 10^{30}$ yr. If at the end of inflation the Universe was hot enough to produce X-particles, then, when it cooled, the X and $\bar{X}$ would have been able to decay into pairs of quarks $(q+q)$ or a quark plus a lepton $(\bar{q}+l)$ and X-bosons induce lepton-quark transitions $qq \to X \to \bar{q}l$. Let us suppose that we have two dominant modes of decay:

$$X \to q+q \quad or \quad X \to \bar{q}+l, \qquad \bar{X} \to \bar{q}+\bar{q} \quad or \quad \bar{X} \to q+\bar{l}$$

Defining r ($\bar{r}$) as the fraction of X ($\bar{X}$) decays in $q+q$ ($\bar{q}+\bar{q}$), and thus $(1-r)$ as the fraction of decays in $\bar{q}+l$, in the presence of C and CP violation we have $r \neq \bar{r}$; hence we can end up with an excess of quarks over antiquarks. Another necessary condition is to be not in thermodynamic equilibrium to avoid the inverse reactions like $qq \to X$ or $\bar{q}l \to X$ having the same rate. Both these conditions can be realized in the Big Bang theory, justifying the hypothesis of baryon-antibaryon asymmetric

universe. The annihilation of the q and $\bar{q}$ leads to the production of radiation. The slight excess of remaining q and l provides the matter of which the present universe is made. In this scheme the numbers of baryons (n_b) and photons (n_γ) are

$$n_b \propto (n_q - n_{\bar{q}}), \qquad n_\gamma \propto (n_q + n_{\bar{q}}),$$

where n_q and $n_{\bar{q}}$ are the numbers of q and $\bar{q}$. Experimentally, the baryon-to-photon ratio is quoted as

$$n_b/n_\gamma = 10^{-9\pm1}.$$

In the framework of Big Bang theory and GUTs, a parameter of the CP violation can be adjusted to fit the baryon-to-photon ratio to the above experimental value.

The above theory is the most generally accepted one for the universe evolution and it is based on the CP violation in GUTs. But it is important to note that we do not know what kind of CP violation should be expected in GUTs. Brown and Stecker [9], and Sato [10] have proposed models of baryon symmetric universe in the framework of the Big Bang and GUTs. These are called Baryon Symmetric Big Bang (BSBB) model. They considered the hypothesis of CP violation coming from spontaneous symmetry breaking with a scalar field that takes complex vacuum expectation values during the cooling of the Universe. The idea was later developed and, the interesting thing is that, when symmetry breaking occurs, say at time t_u, the CP violation can have different signs in causally disconnected regions (regions separated by distance greater than ct_u). We do not know the number of the different disconnected CP regions that can remain after inflation but, if they are more than one, they could be matter and antimatter regions. Each disconnected region is called a domain and the structure of the Universe that is constructed by many separated domains is called the domain structure. Given the fact that there are $\sim 10^8$ clusters of galaxies in our visible universe, the baryon-antibaryon symmetry can be existent at the galaxy cluster level (e.g. clusters of galaxies made of matter and, well separated, clusters of antigalaxies made of antimatter). Recently, models of baryogenesis in the early universe have been improved introducing the baryonic charge condensate $\langle\chi\rangle$ [11] and the generic coupling of χ to the inflation field Φ [12]. In these theories it is possible that antibaryonic regions exist. If these theories are correct, cosmic rays from antimatter domains might be able to diffuse across intergalactic space and enter our Galaxy.

The above mentioned sources of antimatter are supposed to be outside our Galaxy. But even in our Galaxy there might exist sources of antimatters. Such possibility was first considered by E. Witten [13], who introduced superconducting strings that have superconducting electrical currents on them. This consideration is very significant because by that time strings had been thought to be detected only by gravitational effects, for example, through a gravitational lens effect. But if strings have electrical currents, they can be detected by electromagnetic effects. In his presentation, he also suggested that the superconducting strings may manufacture complex antimatter nuclei. This situation would be realized if the string is in an antimatter mode and is surrounded by a dense antimatter plasma of its own making. These strings are so small that they could exist in our Galaxy. Then if the

flux is large enough, the produced antimatter may be observed in cosmic rays. The estimate of a production rate or any numerical consideration has not been done. But, if this is possible and is done, the limit on the existence of superconducting strings can be obtained.

The limit on the separation between matter and antimatter can be obtained from the observations of cosmic γ rays, because if matter and antimatter are in contact they annihilate and produce γ rays. Steigman [14] has made an exhaustive study on the presence of antimatter on a variety of scale from γ-ray observations. In his article, a quantity f is defined as the fraction of the system that could be composed symmetrically of matter and antimatter, and $\langle n^2 \rangle$ as the mean intergalactic gas density. His study gave upper limits on $f\langle n^2 \rangle$ for the distance between 10 to 3000 Mpc varying the temperature of the gas from 10^4 to 10^8 K. However, if matter and antimatter are well separated, this f gives no information about the fraction of antimatters. As mentioned above, matter and antimatter could be separated as domains. Then f is not a good parameter to test the BSBB models. Nevertheless, his study gave $f < 10^{-3}$ in the Local Group for $n \sim 10^6$ cm^{-3} and $T \sim 10^7$ K so that the antimatter region is unlikely to exist at least within 10 Mpc. Stecker [15, 16] speculated that the bump of gamma ray spectra seen around the energy region of 1 to 10 MeV can be explained by the BSBB models. Gao [17] proposed that intrinsic anisotropies in the extragalactic gamma-ray background (EBG), which should be detectable with the Gamma Ray Observatory (GRO), can be used to test the BSBB models. But there has been no evidence of antimatter domains yet.

The γ-ray measurements are only indirect tests for the BSBB models. An experimentally more direct method is to search for antimatter in cosmic-rays. Antihelium and heavier antinuclei in cosmic rays can exist only under symmetric or very exotic hypotheses, while positrons and antiprotons can be produced also via standard interactions between elementary particles. These secondary antiparticles have been already detected and their fluxes were measured in some experiments [18, 19, 20, 21]. Antihelium could be produced in pp collisions with a probability of 10^{-12} or less. This estimate is based on the observation by Dorfan et al. [4] of the production of 4-6 GeV/c antideuterons by using a beryllium target with 30-GeV/c proton beam, and by Antipov et al. [6] of the production of 20 GeV/c anti-^{3}He by 70 GeV-proton beam and an aluminium target. They concluded that the production of antideuteron (anti-^{3}He nucleus) is approximately 5×10^{-8} (2×10^{-11}) times that of negative pion production. A series of experiments followed them. According to their results, the production ratio of $\bar{d}/\pi^-$ arises from 10^{-8} to 10^{-6} as the beam energy increases from 10 GeV to 1500 GeV [7, 8]. On the other hand, the value $(\bar{d}/\pi^-)/(\bar{p}/\pi^-)^2$ remains almost constant of the order of 10^{-3}, regardless of the beam energy. In cosmic-ray interactions, essentially all negative pions produced will decay into electrons. If all cosmic-ray electrons are originated in the negative pions and if these negative pions are all produced in collisions which could produce antibaryons, approximately 2×10^{-11} anti-^{3}He nuclei could reach the Earth for every electron which arrives. As cosmic rays contain 10 times as many heliums as electrons, the relative flux of antiheliums with respect to heliums is of the order of 10^{-12} or less if they come from the secondary production.

As a result, any flux of antihelium which could possibly be measured by present instruments could only be primary or spallation product of still heavier antinuclei. However, when one antihelium candidate is observed, the possibility of secondary production can not be eliminated. Thus, the most evident proof of the symmetric universe would be the detection of antinucleus heavier than helium because it could not have been synthesized in the Big Bang, nor produced in proton collisions with interstellar gas. In other words, the detection means the existence of anti-star well condensed to produce such antinuclei. But at this stage of research, antihelium is the most practical possibility to be detected because antihelium would be most abundant nuclei in antimatter regions. Moreover, the absorption cross sections of heavier antinuclei are too large for them to reach the Earth, and conversely, the resultant spallations would help the flux of antihelium increase.

The first attempts to detect antimatter directly were made by observing cosmic-rays with stacks of nuclear emulsions [22], in which antimatters can be identified by the tracking topology deriving from their annihilation characteristics. Evenson [23] used instrumentation which contains a magnetic spectrometer with spark chambers to be photographed by two cameras. It also contained a time of flight measurement system using scintillation counters and NaI crystals to measure the deposited energy. Smoot et al. [24] also used a combination of spark chambers with a magnet and scintillators. Buffington et al. [25] used spark chambers, however, without a magnet. They designed their instrument in such a way that incident antimatters can be identified by their annihilation vertices in the spark chamber. Badhwar et al. [26] and Golden et al. [27] used multiwire proportional counters with a magnet, scintillators, a calorimeter, and a Čerenkov counter. By now the best confident limits of antihelium to helium ratio are $\overline{\mathrm{He}}/\mathrm{He} \leq 1.6 \times 10^{-4}$ in the rigidity region ($10 \sim 33$) GV [26], $\overline{\mathrm{He}}/\mathrm{He} \leq 9 \times 10^{-5}$ in the rigidity region ($1 \sim 20$) GV [27], and $\overline{\mathrm{He}}/\mathrm{He} \leq 2.2 \times 10^{-5}$ in the rigidity region ($1 \sim 2$) GV [25]. Table 1.1 and Figure 1.1 summarize known $\overline{\mathrm{He}}/\mathrm{He}$ limits so far. However, these limits are not satisfactory enough to test the theories.

Table 1.1: Summary of experiments setting upper limit on $\overline{\mathrm{He}}/\mathrm{He}$.

Rigidity (GV)	$\overline{\mathrm{He}}/\mathrm{He}$ limit	Reference	Technique
< 2.7	$< 7 \times 10^{-3}$	Aizu *et al.* (1961) [22]	annihilation-emulsion
$1 \sim 10$	$< 1 \times 10^{-3}$	Evenson *et al.* (1972) [23]	permanent magnet
$10 \sim 25$	$< 8 \times 10^{-3}$	Evenson *et al.* (1972) [23]	permanent magnet
$4 \sim 33$	$< 5 \times 10^{-4}$	Smoot *et al.* (1975) [24]	permanent magnet
$33 \sim 100$	$< 2 \times 10^{-2}$	Smoot *et al.* (1975) [24]	permanent magnet
$5 \sim 10$	$< 8.8 \times 10^{-5}$	Badhwar *et al.* (1978) [26]	superconducting magnet
$10 \sim 33$	$< 1.6 \times 10^{-4}$	Badhwar *et al.* (1978) [26]	superconducting magnet
$1 \sim 20$	$< 9 \times 10^{-5}$	Golden *et al.* (to be published) [27]	superconducting magnet
$1 \sim 2$	$< 2.2 \times 10^{-5}$	Buffington *et al.* (1981) [25]	annihilation-counter

To search for $\overline{\mathrm{He}}$ down to a $\overline{\mathrm{He}}$/He of $\sim 10^{-6}$, a new balloon-borne experiment, named "a Balloon-borne Experiment with a Superconducting magnet rigidity Spectrometer (BESS)", has been designed based on several new concepts: (1) precise measurement of momentum by a magnetic spectrometer using a thin superconducting solenoid and (2) use of large tracking detectors having a large geometrical acceptance. After the construction and detailed performance checks of the detectors, cosmic-rays were first measured and $\overline{\mathrm{He}}$ search was done in the summer of 1993. Based on this first flight data, the detector was further optimized for the search and the next flight was also successfully done in '94. In the next year, TOF system was improved in the resolution and the flight was also successfully done. In this dissertation, the experimental results of our search for $\overline{\mathrm{He}}$ from the BESS '93, 94, and '95 flight data will be described.

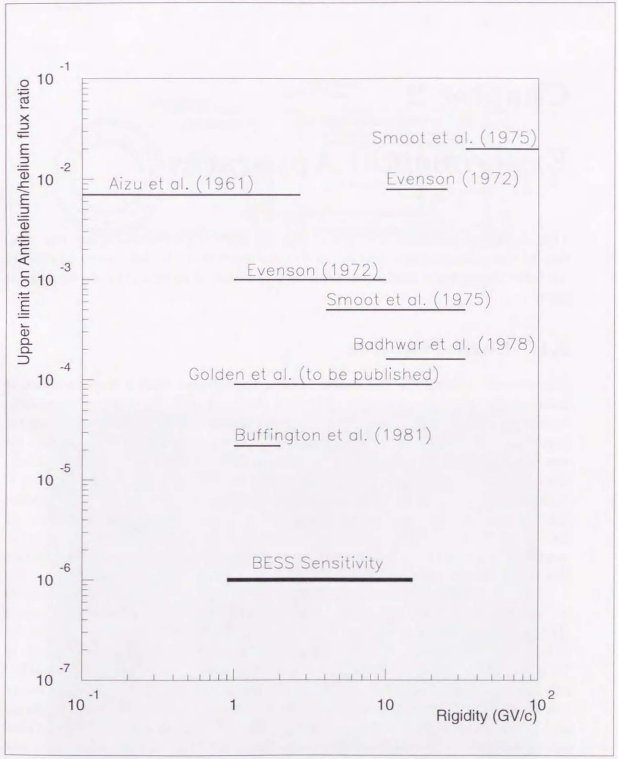

Figure 1.1: Summary of the experiments setting upper limit on $\overline{\mathrm{He}}$/He. Badhwar *et al.* (1978) [26], Buffington *et al.* (1981) [25], Golden *et al.* (to be published) [27], The sensitivity of BESS is shown as a bold line.

Chapter 2

Experimental Apparatus

This chapter provides an overview of the employed experimental apparatus. Section 2.1 describes the basic features and design concept of the detector system, while the following sections discuss in detail its individual detectors and data acquisition system.

2.1 Basic Features

The detector system for the Balloon-borne Experiment with a Superconducting Solenoidal magnet Spectrometer (BESS) is designed with the primary purpose to investigate high energy cosmic particles, i.e. , cosmic antimatter, especially antiheliums and $\bar{p}$'s. BESS has a large geometrical acceptance and high capability for executing precise event recognition suitable for distinct detection of rare cosmic antimatter existing among an abundance of protons and heliums. Such efficiency is realized by combining three key technologies: a thin superconducting magnet, a cylindrical-configured tracking detector, and a rapid data acquisition system. In fact, these features also enable searching for other kinds of rare cosmic rays, e.g., positrons, gamma-rays, and isotopes, as well as precisely measuring the absolute flux of primary protons and heliums.

Figure 2.1 shows a cross-sectional view and photograph of the BESS instrument in '93 flight, being comprised of a jet-type drift (JET) chamber, inner drift chambers (IDCs), superconducting solenoid, outer drift chambers (ODCs), and a time of flight (TOF) counter. Figure 2.2 shows a cross-sectional view of the BESS instrument in '94 flight, where a Čerenkov counter was added outside of the pressure vessel and the other detectors remained the same as '93. Figure 2.3 shows a cross-sectional view of the BESS instrument in '95 flight, where a new pressure vessel with larger capacity and 2.5-mm wall thickness was provided. Then a Čerenkov counter was installed inside the vessel. The remarkable improvement in BESS '95 instrumentation was the installation of new TOF system, in which the width of each paddle became half the size of old one. In the results, about three times as good resolution was obtained for the timing measurement.

These components are arranged radially from the center of the device, and along with the front-end electronics and microcomputers, are enclosed by a 2-mm-thick

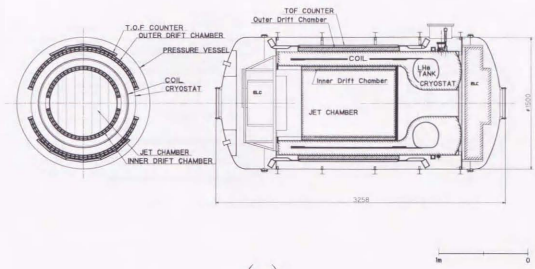

(a)

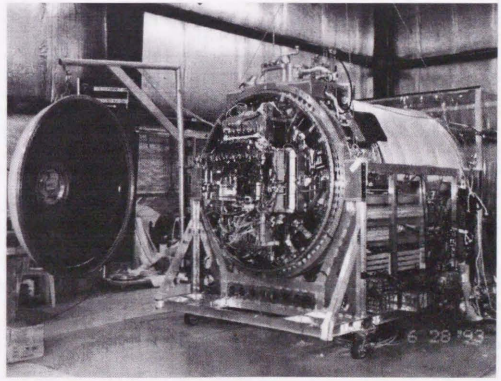

(b)

Figure 2.1: (a) Cross-sectional view and (b) photograph of the BESS instrument ('93).

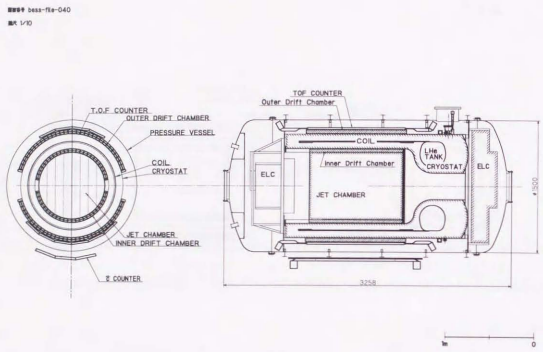

Figure 2.2: Cross-sectional view of the BESS instrument ('94).

aluminum pressure vessel that keeps the inside pressure as the sea level during flights. Situated outside the vessel are an 8-mm tape storage device shielded by iron containers, a power supply system, and a consolidated instrument package (CIP) communication unit which handles communications between the payload and ground station. For the BESS '93 and '94 instrumentation the entire unit weighs 2.1 t. The dimension is 1.5 m in diameter and 3.3 m in length. For the BESS '95 instrumentation, the entire unit was extended to 1.7 m in diameter and 3.8 m in length provided with the new pressure vessel. Then the weight increased to 2.2 t. When suspended from a 2.7-Mft^3 balloon, they were compact and light enough to travel at an altitude of about 35 km.

A thin entrance wall of about 7.5 g/cm^2 enables low energy particles to pass through the detectors, while a cylindrical configuration provides large tracking volume and a geometrical acceptance of $\sim$ 0.4 m^2 sr for '93 and '94 instrumentation. This became $\sim$ 0.32 m^2 for '95 instrumentation due to the dimension of new TOF counter. The JET chamber is capable of precisely detecting particles and measuring their rigidities. Since the tracking device is equipped with 32 measurement positions, even a complicated event having interactions inside the detector can easily be monitored. Table 2.1, 2.2, and 2.3 summarize the main specifications of BESS instrument and difference among the three flights.

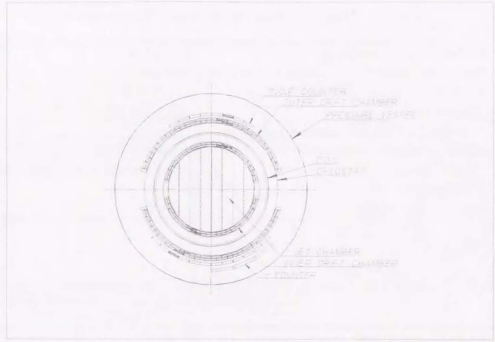

(a)

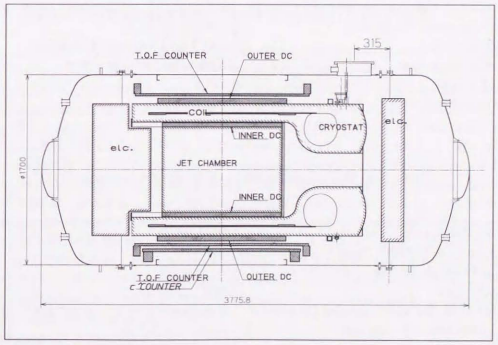

(b)

Figure 2.3: (a) Cross-sectional front and (b) side views of the BESS instrument ('95).

Table 2.1: Main specifications of BESS '93 instrument.

Geometrical acceptance	0.4 m^2 sr
Maximum detectable rigidity in tracking	200 GV
Rigidity range for $\overline{\mathrm{He}}$ identification	1 – 16 GV
Trigger rate	100 – 200 Hz
Material in the spectrometer (per wall)	7.5 g/cm^2
Pressure vessel dimension	1.5 mϕ × 3.3 m
TOF counter	top 4 and bottom 6 paddles
Total weight	2.1 t
Power consumption	1.2 kW

Table 2.2: Main specifications of BESS '94 instrument.

Geometrical acceptance	0.4 m^2 sr
Maximum detectable rigidity in tracking	200 GV
Rigidity range for $\overline{\mathrm{He}}$ identification	1 – 16 GV
Trigger rate	100 – 200 Hz
Material in the spectrometer (per wall)	7.5 g/cm^2 (+ 2.5 g/cm^2 for Č at bottom)
Pressure vessel dimension	1.5 mϕ × 3.3 m
TOF counter	top 4 and bottom 6 paddles
Čerenkov counter	3 paddles outside vessel
Total weight	2.1 t
Power consumption	1.2 kW

Table 2.3: Main specifications of BESS '95 instrument.

Geometrical acceptance	0.32 m^2 sr
Maximum detectable rigidity in tracking	200 GV
Rigidity range for $\overline{\mathrm{He}}$ identification	1 – 16 GV
Trigger rate	100 – 200 Hz
Material in the spectrometer (per wall)	7.5 g/cm^2 (+ 2.5 g/cm^2 for Č at bottom)
Pressure vessel dimension	1.7 mϕ × 3.8 m
TOF counter	top 8 and bottom 12 half-width paddles
Čerenkov counter	3 paddles inside vessel
Total weight	2.2 t
Power consumption	1.2 kW

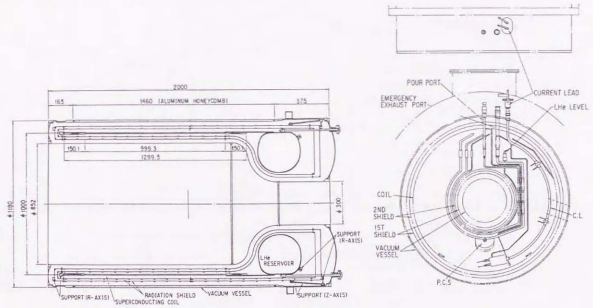

Figure 2.4: Cross-sectional view of the superconducting solenoidal magnet.

2.2 Superconducting Solenoidal Magnet

Figure 2.4 shows cross-sectional views of the superconducting solenoidal magnet (MAG), which has a 0.8 mϕ × 1.0 m warm bore that encloses the JET and inner drift chambers. A magnetic field of 1 T (maximum 1.2 T) is generated inside the bore at a nominal current of 520 (540) A, with the resultant field uniformity being ±15%. A solenoid coil (1 mϕ × 1 m (ℓ) × 5.4 mm (t)) made of aluminum-stabilized superconductor NbTi(Cu) is installed inside the double thermal shielded cryostat, and is indirectly cooled through the aluminum cylinder by a toroidal-shaped liquid helium reservoir tank with 150-ℓ capacity (static indirect cooling method) [28]. This method has an advantage over the bath cooling method in that it allows using a thinner cryostat wall. The MAG's thickness including the cryostat is 0.21 radiation length per wall and its total weight with helium is 430 kg. The amount of stored energy at 1 T is 815 kJ. Pure aluminum strips (PAS [28]) are attached to the inner surface of the solenoid for quenching, i.e. , they rapidly conduct thermal energy in the axial direction and homogenize the thermal distribution. Table 2.4 summarizes the main specifications of the MAG.

The magnet is equipped with a persistent current switch (PCS) fabricated from a superconductor and heater. It is heated up to break the superconduction during magnet excitation, then cooled and automatically shortcut after being charged. The current from the magnet is subsequently able to pass through the PCS. Since the decay constant of this current is more than 900 years, if helium is filled to its maximum level, the current persists for as long as 6 days with no energy supply to

Table 2.4: Main specifications of the superconducting solenoidal magnet (MAG).

Dimensions	
Coil diameter	1.0 m
length	1.3 m
coil thickness (center)	5.2 mm
(end notch)	10.4 mm
Cryostat diameter	1.18 m
length	2.0 m
Useful aperture diameter	0.85 m
length	1.0 m
Central field	1.0 T
Current	500 A
Maximum field	1.2 T
Stored energy	815 kJ
Wall thickness	0.21 X_0 per wall
	4 g/cm^2 per wall
Total weight	430 kg
Conductor	Nb/Ti/Cu
Stabilizer	Pure Al(99.999%)

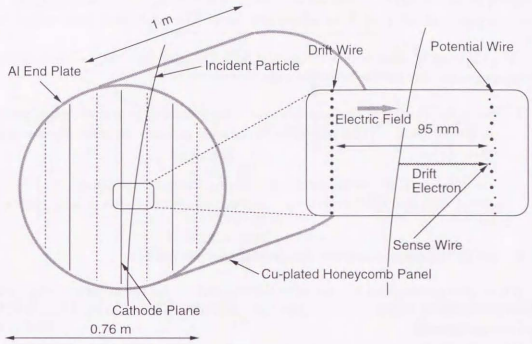

Figure 2.5: Schematic view of the JET chamber.

the magnet. The magnet can be safely discharged by switching off the PCS and shunting the magnet current into a resistor located external to the vessel.

2.3 JET chamber

The JET chamber is a cylindrical drift chamber situated inside the magnet, (Fig. 2.5) having a tracking volume of 0.754 mϕ $\times$ 1 m.

Cathode planes partition the chamber into four sections, with each plane consisting of 100 aluminum wires with a 200-μm diameter. The wires are laid out, though actually they are stretched, at 6.7-mm intervals, and a high voltage of -10.8 kV is applied to produce a constant electric field which drifts ionized electrons to the sense wires. At the center of each section, the sense and potential wires are alternately laid out at 13.4-mm intervals. The sense and potential (cathode) wires are respectively 20-μmϕ gold plated tungsten-rhenium wires and 200-μmϕ gold-plated aluminum wires, and are stretched with a tension of 40 and 350 gw. To minimize wire loosening due to creep, before being soldered, the wires were pre-stretched with a tension of 15 and 100 gw, respectively. The sense wires are staggered by 0.5 mm to resolve left-right ambiguity. The outer two sections have 32 sense and 33 potential wires, while the inner two correspondingly have 52 sense and 53 potential wires. The maximum drift distance of ionized electrons is 95 mm.

The cylindrical side walls are made of alamyd core honeycomb to minimize material thickness and weight. The inner surface of the honeycomb panel is made of a

copper-plated KAPTON sheet, on which the field-shaping patterns are etched. The two end-plates are 25-mm-thick aluminum discs. The chamber's total weight is 60 kg.

The chamber is filled with a mixture of 90% CO_2 and 10% Ar, being suitable for this experiment due to the following reasons:

1. The drift velocity of this gas mixture is slow enough to achieve good position resolution using a relatively slow electronics package designed for low power consumption.

2. Due to a small diffusion coefficient, timing fluctuations caused by the longitudinal diffusion of the electron cloud are small even after a long drift of 95 mm.

3. The gas mixture is non-flammable and easy to handle.

This mixture was used for the other drift chambers for the same reasons, in fact, the entire vessel is filled with it so that any chamber suffering a small gas leak will remain operational.

The signals from the sense wires are picked up by 112 preamplifier channels mounted on the end-plates, then amplified and converted into voltage signals that are directly fed into 28.5-MHz flash-type analog-to-digital converter (FADC) modules. A FADC module has sixteen channels in it and sixteen modules can be installed at the maximum for JET and IDC readout. Eight modules for '93 instrument and nine modules for '94 and '95 instruments were installed for JET readout. Each channel amplifies the signals and digitizes them into 8-bit digits every 35 ns. The output data of each FADC channel contains information on the charge and timing for every 35 ns, in other words, four-hundred sets of the charge and timing data for 14 μs of the full drift time. Since a typical single pulse has a pulse width of about 400 ns, multiple hits in a single wire can be well separated and recognized. However, the total amount of FADC data is too large to record all, and consequently, on-line zero-suppression circuits are employed to reduce the data amount, where digitized data is discriminated by a digital comparator and only data above a threshold value is accumulated into first-in-first-out (FIFO) memory. Furthermore, a data compressor circuit sequentially reads all FIFO memories of the FADC channels and compresses them into formatted data-packet, where the timing, total integrated charge, width, rising shape, and readout channel number of a pulse signal were packed into a 8-byte formatted data, however the entire pulse shapes were lost. This data compression scheme reduced the data size of an event by a factor of 3 and it takes 200 μs for the compressor to scan all channels and complete the process for an event of the typical data size.

The position of the hits are three-dimensionally measured by the timing and charge of the signals. In this dissertation, cylindrical coordinates ($r\phi z$) are used, with the magnet field direction being defined as the z-axis and the perpendicular plane to the z-axis as the $r\phi$ plane. The hit position in the $r\phi$ plane is calculated by its drift time. Although drift length x and drift time t are nearly proportional,

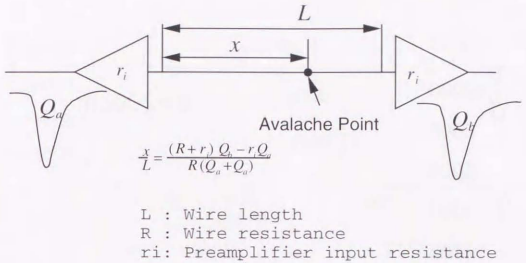


```
L : Wire length
R : Wire resistance
ri: Preamplifier input resistance
```

Figure 2.6: Circuit model of the charge division method used for determining the z-coordinate.

some nonlinear effects nevertheless exist due to distortion of the electric field and inclination of the track in the cell. Such nonlinearity, however, is corrected by fitting the deviation of the hit position to a third-ordered polynomial. The hit position along the z-coordinate is obtained by applying the charge division method, where Fig. 2.6 shows the employed circuit model. To minimize errors, the internal resistor and gain of the preamplifier are calibrated and adjusted using the actual flight data.

The FADCs read signals from 80 sense wires, some of which are read from both ends to determine the z-coordinate via charge division method. 32 wires were read from both sides in '93 flight. This number increased to 48 wires in '94 and 95 flights by installing one additional FADC module. As the tracks pass through the central region, where the signals can be read through the two longer columns of wires, a maximum of 24 positions can be measured in the $r\phi$ plain. As for z direction, 16 positions and 24 positions can be measured in '93 and '94-'95 flights, respectively. Based on the residuals obtained from the fitted track (Fig. 2.7), the overall resolution of $r\phi$ plane is estimated to be 200 μm. These resolutions are dependent on the drift length due to the diffusion of electrons. Figure 2.8 shows the resolution as a function of the drift distance (a) and the angle of the track trajectory across the cathode wire plane (b), where both resolutions are gradually degraded according to the drift distance and angle.

The resolution of the z-coordinate measurement is 2.5 cm for single-charged particles (Fig. 2.9 (a)), being worse than the expected value of 1 cm, since all the charge information below the threshold value is lost using the zero-suppress and compress scheme, and cannot be precisely corrected. On the other hand, 1.5-cm resolution is obtained for multiple-charged particles (Fig. 2.9 (b)) because they reduce the threshold effect.

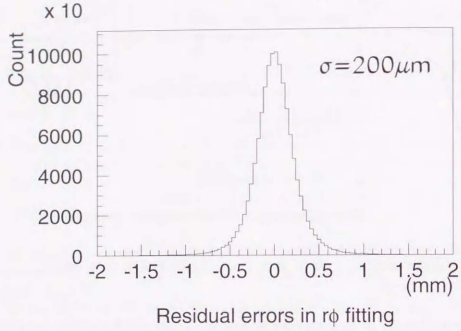

Figure 2.7: Residual distribution of the JET $r\phi$ hit points.

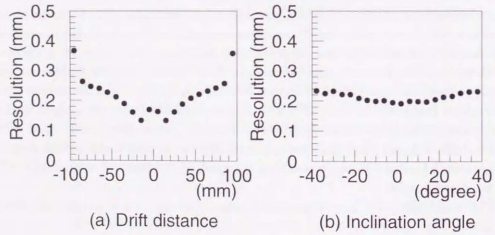

Figure 2.8: JET chamber $r\phi$ resolution as a function of (a) the drift distance, and (b) the angle ϕ across the cathode wire plane.

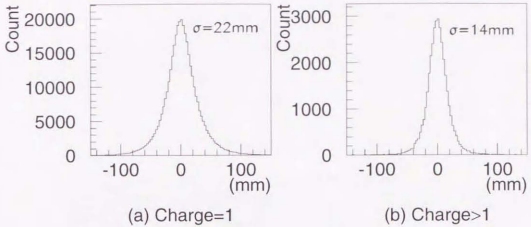

Figure 2.9: Residual plot of the JET chamber along the z-coordinate for (a) single-charged and (b) multiple-charged particles

2.4 Inner and Outer Drift Chamber

The inner drift chamber (IDC) and the outer drift chamber (ODC) are cell-type arc-shaped drift chambers located inside and outside the magnet, respectively (Fig. 2.10). The IDC (ODC) is a 1.06-m-long (1.18 m) and 36-mm-thick (44 mm) chamber located between the radii of 384 mm (594 mm) and 420 mm (638 mm) covering a polar angle from 8 (18) to 172 (162) degrees. Both chambers are identical except for their dimensions and magnetic field strength, i.e. , 1 T for the IDC and about 0.1 T for the ODC. The mechanical structure of each chamber is composed of four alamyd core honeycomb panels with end and side plates made of engineering plastic (G10). Figure 2.11 depicts a cross-sectional view of the $r\phi$ plane, where the surface of the panel is made of 18- and 125-μm-thick copper and KAPTON sheets, respectively. The outer surface of the Cu sheet is covered with a 0.5-mm-thick Al sheet to increase mechanical strength. The inner KAPTON sheet is etched at 3-mm interval to form a 1.5-mm-wide and 18-μm thick electric field shaper, and corresponding pairs of 7.5-mm-wide and 18-μm-thick diamond-shaped vernier pads surround the sense wires to detect the z-coordinate position. The inside of the chamber is divided into two 12-mm-thick layers. At the center of each layer, sense wires and field wires are alternately laid out in about 50-mm spacing intervals. This wire configuration also acts to calibrate the drift velocity which is obtained by adjusting the sum of the drift length of both layers to the wire spacing, i.e. , 50 mm.

The sense and field wires are respectively gold-plated 25-μmϕ tungsten-rhenium and 250-μmϕ aluminum wires. They are stretched with a tension of 55 gw and 400 gw, respectively. To minimize wire loosening due to creep, before being soldered, the wire were pre-stretched with a tension of 15 and 40 gw, respectively.

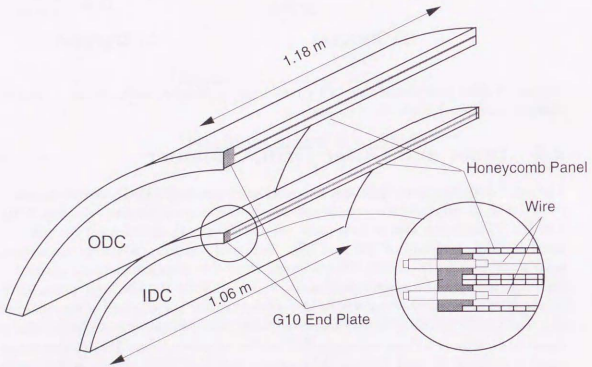

Figure 2.10: Diagram showing a cross-sectional view of IDC and ODC.

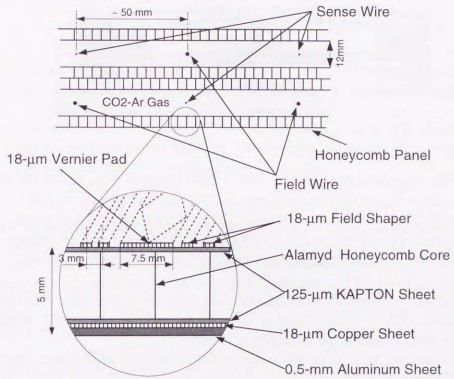

Figure 2.11: Diagram showing a cross-sectional view of the IDC and ODC in $r\phi$ plane.

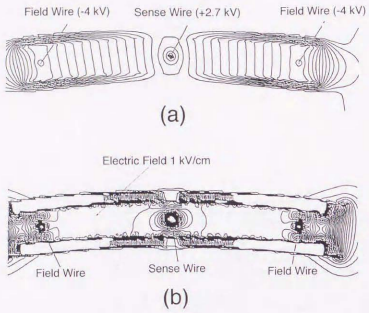

Figure 2.12: (a) Equipotential and (b) electric field strength contours of the IDC.

A high voltage of 2.7 kV (2.6 kV) is applied to the sense wires of the IDC (ODC), while –4.0 kV (–4.5 kV) to the field wires and field shapers. Figure 2.12 shows contours of the equipotential and electric field strength of the IDC. The electric field is inclined 5.5° to the drift direction to compensate for the Lorentz angle produced by the magnetic field, and is constant across most of its drift region. The shape of the ODC's electric field is almost the same as the IDC's, with the exception that the Lorentz angle is negligibly small.

Both chambers are filled with the same gas mixture used in the JET chamber (90% CO_2, 10% Ar).

The chamber signals from the sense wires and vernier pads are both amplified by preamplifiers mounted on an aluminum plate attached to the end-plate. Figure 2.13 shows a diagram depicting the read-out scheme of the IDC and ODC, where one signal is read from each IDC sense wire, two for each ODC sense wire, and four signals are read from each corresponding pair of vernier pads. Thus, a total of five or six signals are obtained per IDC or ODC sense wire. As explained next, these signals are distributed among amplifier and discriminator (AMP/DISCRI) modules, analog-to-digital converter (ADC) and time-to-digital converter (TDC) modules, and flash-type analog-to-digital converter (FADC) modules.

1. The IDC and ODC sense wire signals are amplified and discriminated in the AMP/DISCRI modules. If the discriminated signal in the inner and outer layer of each chamber coincide, they are fed through the track trigger (TT) module, which performs a rapid analysis of their rigidity (see Section 2.8.1).

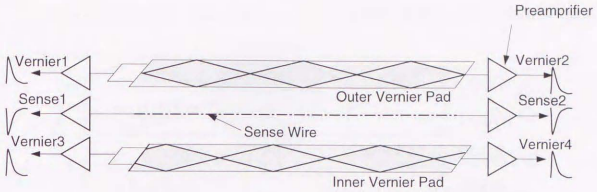

Figure 2.13: Read-out scheme for IDC and ODC signals.

2. The ODC sense wire signals are then fed to the TDC modules which convert their timing into 12-bit digits, while the ODC vernier signals are processed by the ADC modules which integrate their charge during a 500-ns gate and convert them into 12-bit digits. The timing information is utilized for determining the hit position of the ODC in the $r\phi$ plane, while the charge information for determining the hit position along the z-axis.

3. The IDC vernier signals are processed and converted into timing and charge information by 28.5-MHz FADC modules and compressors in the same manner as the signals from the JET sense wires. Hit positions in the $r\phi$ plane and along z-axis are respectively determined using the timing and charge information.

The hit positions of the IDC (ODC) in the $r\phi$ plane are determined using the measured drift time. Briefly, the drift velocity is calibrated using the sum of the drift times of the inner and outer layers of the IDC (ODC), after which the polynomial corrections are applied to minimize errors in the tracks. The overall resolution of the $r\phi$ plane is estimated to be 200 μm based on the residuals obtained from the fitted track (Fig. 2.14). Figure 2.15 shows the IDC's $r\phi$ resolution as a function of the drift distance (a) and the angle of the track trajectory with respect to the axial direction (b), where both resolutions are gradually degraded according to the drift distance and angle.

The hit position along z-axis is measured using the signals generated on the corresponding sets of vernier pads, i.e. , each pad is situated on the inner and outer KAPTON sheet such that they surround one sense wire. Each set is cut as shown in Fig. 2.16, having a cycle of 100 mm for the IDC (120 mm for the ODC). The corresponding set of pads are situated such that one is shifted along z-direction by a quarter cycle with respect to another.

When the drifted electrons avalanche near a sense wire and deposit their charge on it, induced signals are generated on the corresponding set of pads. The charge on each pad is divided into the two parts (A and B) of the pad and the both charge are separately read out. We define the normalized charge ratio of A and B for each

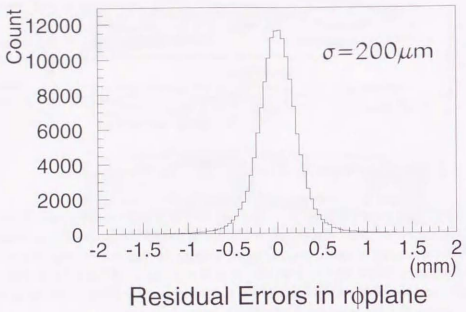

Figure 2.14: Residual distribution of the IDC $r\phi$ hits.

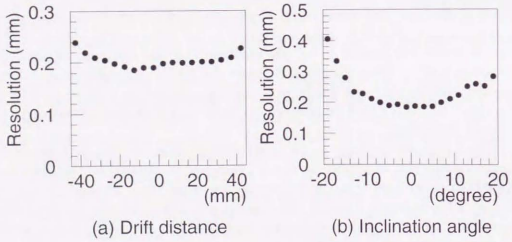

Figure 2.15: IDC $r\phi$ resolution as a function of (a) drift distance, and (b) angle ϕ with respect to the axial direction.

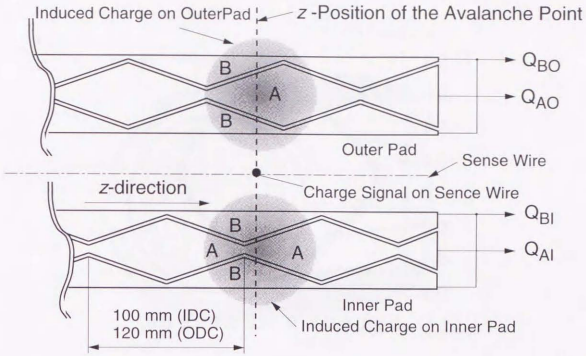

Figure 2.16: Corresponding sets of vernier pads.

pad as:

$$\varepsilon_{I(O)} = \frac{Q_{AI(O)} - Q_{BI(O)}}{Q_{AI(O)} + Q_{BI(O)}}$$

where $Q_{AI(O)}$, $Q_{BI(O)}$ are the charge on A and B for inner pad (outer pad). Each ε parameter is linearly related to the z-axis position of the avalanche point. Figure 2.17 shows the scatter plot of the ε parameter. One cycle around the round square locus represents a movement of 100 mm (120 mm) along z-axis. The line in the figure shows the ε_I and ε_O calculated numerically for various z-position. We can then derive the hit position along the z-coordinate by comparing the measured ε pair to the numerical calculation. The spread of the measured ε values around the numerical line provide the estimation of the z-axis resolution (Fig 2.18). When the coarse z-position obtained by the charge division of the JET chamber, absolute z-position can be determined by the precision of 350 μm.

2.5 Time of Flight Hodoscope in BESS '93 and '94 instrumentation

In BESS '93 and '94 instrumentation, the Time of Flight hodoscope (TOF) consists four upper and six lower plastic scintillation counters which are placed just outside the ODC at the radius of 65 cm, as shown in Fig. 2.19. The dimension of each

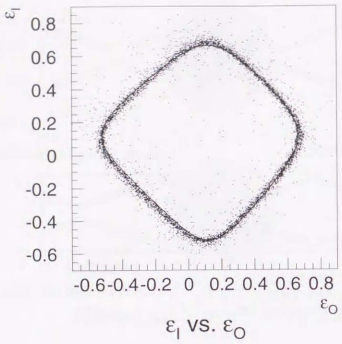

Figure 2.17: Scatter plot of the ε parameter of the inner and outer pad.

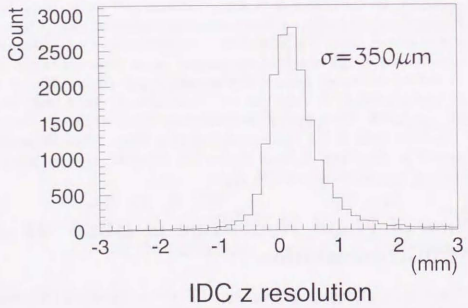

Figure 2.18: Spatial resolution of the z-coordinate measurement in the IDC.

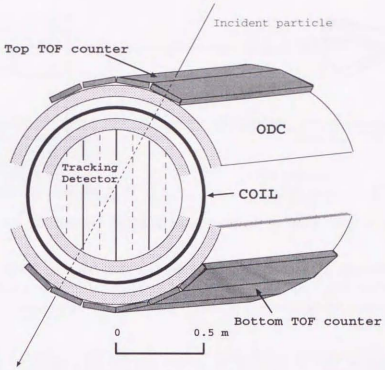

Figure 2.19: Layout of time of flight hodoscope in BESS '93 and '94 instrument.

scintillator is 110 cm × 20 cm × 2 cm, and Figure 2.20 shows the schematic view of the single TOF counter.

When an incident particle passes through a TOF plastic scintillator, the ionization loss of the energy is converted into light. The light signals are transmitted in the scintillator and are guided adiabatically through the twisted-strip acrylic light guide to the photo-multiplier tubes (PMTs) on both ends. For a daily check and calibration use, there equipped a light-emitting-diode (LED) at the center of the scintillator, and the connector for the laser light are fixed on the side of the light guide. The whole counter is wrapped with one layer of aluminized mylar and two layers of black vinyl sheet to reflect the light and to shield the light from outside, respectively.

Since the PMTs are operated in the magnetic field of 1.8 kG, where ordinary PMTs could not be used, we use PMTs with 19 stages of mesh-typed dynodes, H2611SX (Hamamatsu photonics), which is specially designed for usage in a high magnetic field. Besides, to reduce the effect of the field, the axis of the PMT is aligned with the field direction by 15 degrees. The test of PMT in the 1.8 kG reveals that the PMT gain increases by at most 10% and the timing shifts by 100 ps, however, no degradation in the timing resolution is observed.

Various high voltage values between 1.8 kV and 2.3 kV are applied to adjust the gains of all PMTs to the same value.

The output signals of the counter are utilized for three different purposes; a

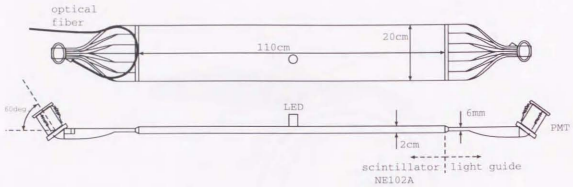

Figure 2.20: Time of flight counter of BESS '93 and '94 instrument.

timing measurement, a charge measurement, a fast trigger. To avoid interference with each other, three signals are extracted separately from the anode, 19th dynode, and 18th dynode, respectively (Fig. 2.21). Each signals are processed in the following ways:

- The anode signals are used for generating the stop signal in the timing measurement. They are discriminated by a CAMAC discriminator (DSC) module and fed into the CAMAC TDC through a 50-ns delay cable. The threshold of the DSC can be set via CAMAC command in 0.23 mV step. Although the minimum threshold of DISCRI can be set as low as 5 mV, a value of 10 mV is selected to compromise between the timing resolution and the probability of spurious stop signal due to noise of the electronics. The TDC is a modified version of Lecroy 2208, which accepts eight ECL-level signal from the DSC and one NIM-level start signals from a T0 trigger module. The dynamic range is 11-bits and conversion gain is 50 ps/count. According to the test, the timing resolution of 70 ps and the linearity of 0.1% over a full scale are obtained. Since inductive parts are used in the oscillator circuit, the timing conversion gain is shifted by 2.5% in the actual operating field. However there is no effect on TDC resolution and linearity.

- The 19-th dynode signals are used for generating a fast trigger signal. First each PMT signal at the both ends is summed up after integration with time constant of 20 ns to reduce the position dependence of the signal amplitude. The summed signals are fed into the two-level discriminator (2LD) modules, which has a capability of setting two level thresholds for all eight channels. One threshold is set to 15 mV, which corresponds to half of the minimum ionizing pulses. The other is set to 50 mV for the multiple charged particles. Four kinds of the DSC outputs, i.e., top low-threshold (LOW), top high-threshold (HIGH), bottom LOW, bottom HIGH are ORed separately in the 2LDs. The resultant four signals are fed into the T0 trigger module to generate a fast trigger pulse by combining them. Detailed trigger scheme will be described

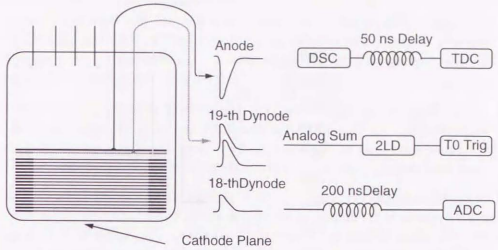

Figure 2.21: Read-out scheme PMT signals

later in Section2.8.1.

- The 18-th dynode signals are utilized for the charge measurement. It is fed to a charge-to-voltage type analog-to-digital-converter (ADC) module through a 200 ns analog delay line. The charge is integrated during the gate width of 50 ns and converted into 12-bit digits. The conversion gain is 0.6 pC/count. The integrated nonlinearity is below 1 count over the full-scale, which provide a wide dynamic range of charge measurement, from 1/20 to 100 times as large as the charge corresponding to minimum ionizing particles. The intrinsic resolution of the charge measurement is 10% for minimum ionizing particles, which is dominated by photo-electron statistics in the PMT.

The gain and timing of each counter were first calibrated using the beams from the proton synchrotron at KEK before the installation. Protons and pions with 1 GeV/c is used to determine the high-voltage applied to each counter and parameters for a time-walk correction.

After installation into the BESS instrument, the gain and the timing are monitored and calibrated both in the ground and in the flight situation by the following three ways:

1. The laser light pulsar (Hamamatsu PLP-02) is used for the precise measurement of the TDC conversion gain and timing offset for each counter in the actual operating condition. The output light has a wave length of 410 nm and is led into the counter through a 1-mm-diameter quartz fiber. The excellent stability of the pulse height and the timing of laser pulse enable to calibrate the timing and gain of each counter, though this calibration scheme is not available when the endcap is closed.

2. The blue LED light is also used to monitor the gain and timing of the counters. Although LED signals have slower rise-time and less stability than the laser signals, there are two advantages in the calibration with the LED. Calibration can be performed even after the pressure vessel closed. PMTs at both ends are simultaneously calibrated and the their gain can be relatively adjusted.

3. In the flight situation, cosmic-rays are used to determine all calibration parameters used in the off-line analysis. Since both the gain and the timing fluctuate according to the temperature during the flight, we divided the flight data into several runs and calibrate them in the individual run.

The performance of the TOF counter is studied using the '93 flight data samples. Figure 2.22 shows the z-dependence of the PMT charge measured for the proton samples with above 3 GeV/c. Figure 2.22-(a) shows the charge distribution versus the z position. The line in the figure indicates the fitted curve for the peak of the distribution using the following equation, i.e., $a + be^{cz}$, where a,b, and c are parameters to be fitted. Figure 2.22-(b) shows the charge distribution at z =0. The resolution determined from the distribution below peak is about 10% at the center of the counter, which means that about forty photo-electrons are obtained for energetic protons. Figure 2.23-(a) shows the timing resolution of the PMT versus the z position. At the center of the counter, the timing resolution of 300 ps is observed. Figure 2.23-(b) shows the timing resolution versus square root of the number of the photo-electrons (N_{pe}). The linear correlation between two variables is clearly observed. Figure 2.24 shows the residuals of measured TOF from the expected TOF for proton sample and helium sample in BESS 93 flight data. These are calculated by following equation.

$$\Delta\text{TOF} = \text{TOF(directly measured)} - (\text{path length})/\text{velocity} \tag{2.1}$$

$$\text{velocity} = c\,(p/E) \tag{2.2}$$

where c is the light velocity, p is the measured momentum, and E is the energy calculated from equation $E = \sqrt{p^2 + \text{mass}^2}$. The curves in the figure are the results of Gaussian fit and the resultant sigmas are 270 ps for the proton sample and 190 ps for the helium sample respectively. For helium sample the rigidity region is restricted in greater then 7 GV in order to decrease the effect of ^{3}He mixing, although there still exists a slight discrepancy from the Gaussian in negative region. Figure 2.25 shows the residuals of measured TOF for proton sample and helium sample in BESS 94 flight data. The sigmas are 300 ps for the proton sample and 210 ps for the helium sample, respectively.

2.6 Time of Flight Hodoscope in BESS '95 instrumentation

In order to obtain better timing resolution, TOF system was improved in BESS '95 instrument, where eight upper and twelve lower plastic scintillation counters with

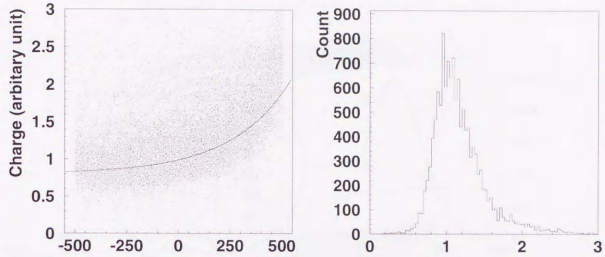

Figure 2.22: (a) z-position dependence of the PMT charge measured. (b) Charge distribution at the center of the counter ($z = 0$) ('93).

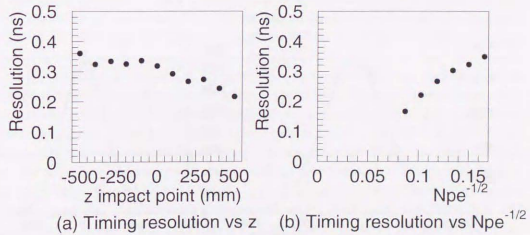

Figure 2.23: (a) Timing resolution of the PMT vs. the z-position. (b) Relation between the timing resolution and square root of N_{pe} at the center ('93).

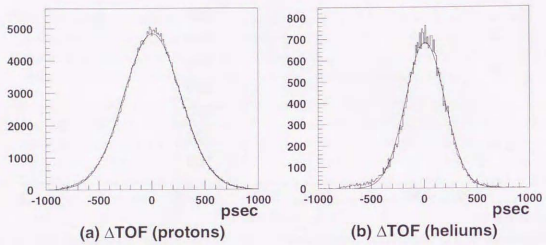

Figure 2.24: ΔTOF (a) for proton sample and (b) for helium sample ('93).

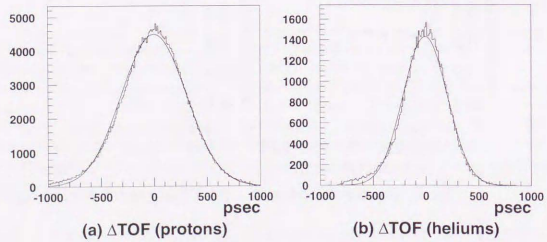

Figure 2.25: ΔTOF (a) for proton sample and (b) for helium sample ('94).

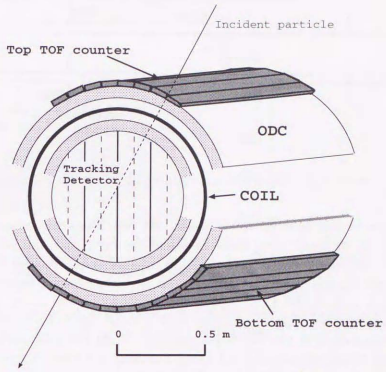

Figure 2.26: Layout of time of flight hodoscope in BESS '95 instrument.

a dimension of 95 cm × 10 cm × 2 cm were installed as shown in Fig. 2.26. The schematic view of a single new TOF counter is also shown in Figure 2.27.

For the design of a new TOF counter, an optical simulation program GUIDE 7 [29] was used. From the simulation, it was concluded that the width of scintillator should be much narrower for better timing resolution, and the fish-tail type light guide is more efficient than the twisted-strip type. Careful considerations resulted that the LED should not be fixed to the new counter because the hole defect of mylar sheet would degrade the reflection efficiency. From the constraints of the number of the readout electronics and the power dissipation, the width of a single paddle was determined as 10 cm. Then some proto-type counters which had Bicron BC404 and BC420 scintillators with various types of light guide, were made, employing the same PMT as '93 and '94 instrumentation, i.e. H2611SXA. Related with the direction of the magnetic field, the PMT attachment angles of 60 and 90 degrees were tested using proton and pion beams with momentum of 1.1 and 2.0 GeV/c at KEK PS. From these beam tests, it was concluded that BC404 is preferable than BC420, the angle of the attachment should be 90 degrees, and then the timing resolution of 100 ps might be expected in a real scientific flight. Finally the design of new TOF counter was determined as shown in Fig. 2.27 and they were fabricated. Then the scintillator part of a new TOF paddle was wrapped with one layer of imobiron and the light guides at both ends were wrapped with one layer of aluminized mylar to obtain good efficiency of the reflection. Furthermore, a part of the light guide near the PMT

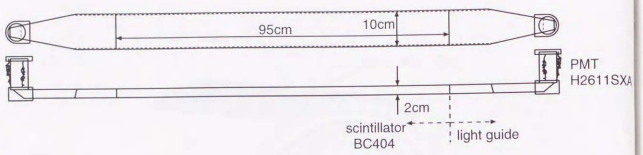

Figure 2.27: Time of flight counter of BESS '95 instrument.

is wrapped with one layer of silver mylar. At last, the entire counter is wrapped with two layers of black vinyl sheet to shield the light from outside. The readout method was not changed except that the number of the TDC and ADC electronics were doubled. On the other hand, in order to save the power consumption, the high voltage supply unit of the TOF system was improved in the conversion efficiency.

After simple calibration of the new TOF counter with the beam test data, the system was installed in the BESS instrument. Then the gain and timing of each counter were thoroughly calibrated using the data obtained from cosmic-ray runs by the whole detectors on the ground. Then various high voltage values between 1.6 kV and 2.1 kV were applied to adjust the gains of all PMTs to the same value.

The performance of the TOF counter is studied using the '95 flight data samples. Figure 2.28 shows the z-dependence of the PMT charge measured for the proton samples with above 3 GeV/c. Figure 2.28-(a) shows the charge distribution versus the z position. The line in the figure indicates the fitted curve using equation $a+be^{cz}$. Figure 2.28-(b) shows the charge distribution at z =0. The resolution determined from the distribution below peak is about 6% at the center of the counter, which means that about one-hundred-twenty photo-electrons are obtained for energetic protons. Figure 2.29 shows the residuals of measured TOF from the expected TOF for proton and helium samples in BESS 95 flight data. The curves in the figure are the results of Gaussian fit and the resultant sigmas are 110 ps for the proton sample and 100 ps for the helium sample, respectively. For the helium sample, the rigidity region is restricted in greater then 7 GV in order to decrease the effect of ^{3}He mixing, although there still exists a slight discrepancy from the Gaussian in negative region.

2.7 Čerenkov counter

BESS was designed for the purpose of search for antiproton, as well as antihelium. From the results of '93 flight, the $\bar{p}/p$ ratio flux ratio was shown up below the kinetic energy of 0.5 MeV [21]. In order to determine the flux ratio up to 1 GeV, Čerenkov counter was designed for BESS '94 instrument. A proto-type counters were made and tested by the $\pi 2$ beam line of KEK PS. Then, it was concluded that up to the

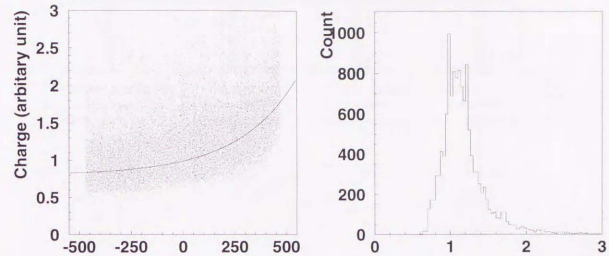

Figure 2.28: (a) z-position dependence of the PMT charge measured. (b) Charge distribution at the center of the counter ($z = 0$) ('95).

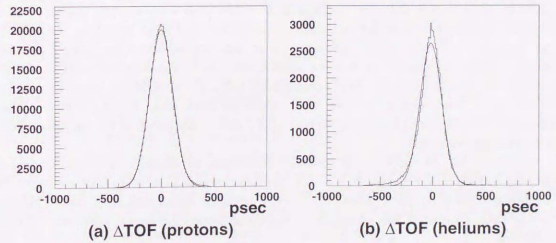

Figure 2.29: ΔTOF (a) for proton sample and (b) for helium sample ('95).

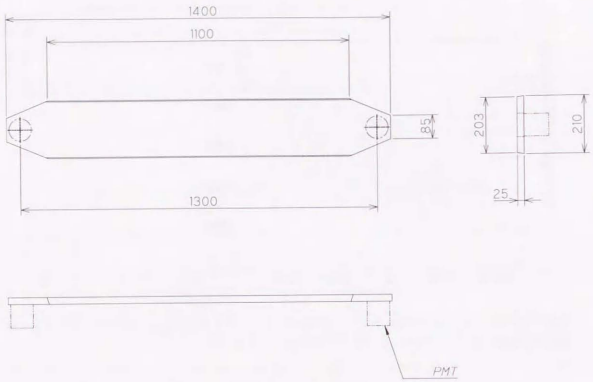

Figure 2.30: Čerenkov counter of BESS instrument.

momentum of 1.7 GeV, protons can be clearly separated from lighter particles, i.e. mainly pions.

Figure 2.30 shows a schematic view of a single Čerenkov counter. The single counter, 1500 mm × 240 mm × 23 mm, is made with UVT acrylic plastic, and is wrapped in aluminized mylar to obtain good efficiency of light reflection. Originally, the pressure vessel of BESS '94 instrument was not designed to carry Čerenkov counter inside. In a result, it was installed outside to be operated in vacuum. Three paddles of Čerenkov counter were arranged cylindrically around the vessel at a radius of 820 mm. Each single counter was viewed on both ends by two vacuum-proof photomultiplier tubes (Hamamatsu R5542SP), whose diameter of the photo-cathode is more than 64 mm.

In BESS '95 instrument, the pressure vessel was extended so that the Čerenkov counter was installed inside. In a result, the counter was arranged much closer to the the bottom TOF counter, where no more aluminum vessel wall of 2-mm thickness. In addition, wrapping was changed to Millipore sheets for better efficiency of light reflection.

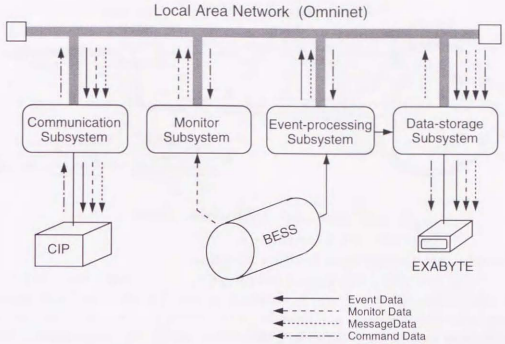

Figure 2.31: Schematic diagram of the data acquisition system

2.8 Data Acquisition System

The BESS data acquisition system (DAQ) is designed and specialized for this balloon-borne experiment, using a unique parallel multi-processor method, custom-made hardwire circuits, low-power CAMAC modules, FADC modules and so on.

Because of a large geometrical acceptance, a primary trigger rate of the BESS detector exceeds a few thousand per second. This is far above the maximum storage rate of about 200 Hz. The BESS DAQ needs to process these large amount of data and to reduce both the number of events and the data size. The hard-wired data compression scheme reduces event data size by a factor 1/3 and fast hard-wired trigger logic eliminates most of unwanted backgrounds. In addition, multi-processor system gather and packs the event data into an average size of 1 kbyte in 1 ms. Thus the data are reduced to the acceptable rate of 80–90 Hz.

On the other hand, it is also important for the balloon-borne experiment to reduce the power consumption. A larger power consumption demands additional batteries and results in a larger total weight or in a shortening flight time. Besides, the heat generated by the electronics is accumulated in the payload and might damage the detectors and electronics. To avoid these problems, most of the electronics, for example CAMAC modules and FADC modules, are custom-made to minimize the power consumption while keeping the processing speed fast.

Figure 2.31 shows general scheme of the BESS DAQ. Four subsystems functions for following four purposes; event-process, data-storage, monitoring, and communication[30]. Each subsystem is controlled by a microprocessor(NEC-V40 or V50) and is linked

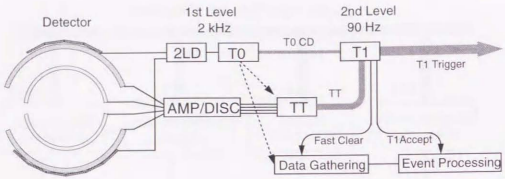

Figure 2.32: BESS trigger scheme

with each other through serial bus-lines (Omninet).

Event-process subsystem gathers and processes the event data from each detector when the trigger signal initiates the data acquisition. The processed data are sent to the data-storage subsystem and recorded in two 8-mm EXABYTE tapes. The house keeping data such as temperature or pressure are handled by the monitor subsystem and are transferred to the data-storage subsystem to be recorded in the tapes. The communication subsystem manages communication between the ground station and the payload. Some of the recorded data are telemetered to the ground over a radio link to monitor the detector status during the flight. The commands to control the detector are transmitted to the payload by the communication subsystem.

In following sections, each component of the DAQ is described in detail.

2.8.1 Trigger

BESS trigger system is designed with a primary objective to detect efficiently $\bar{p}$ and antihelium signals while rejecting most of proton and helium backgrounds. It also accepts some portion of other cosmic-ray species such as gamma rays, electrons, positrons, deuterons, tritons, and other heavy isotopes as well as protons and heliums.

Trigger consists of two levels (Fig. 2.32). The first level is a fast "T0 trigger" where the combined signal of the top and the bottom scintillators initiates data acquisition cycle. The second level is a "T1 Trigger" where event reduction is performed through a "track trigger" (TT) or "count down" (CD) logic. The TT scheme selects preferably negative-charged particles judging from the chamber hit pattern, while the CD logic reduces the event rate irrespective of the event configuration. If the event is judged to be accepted by either the TT or CD logic, the T1 trigger approves further data processing. Otherwise the data acquisition cycle is discontinued and all electronics are cleared for the next cycle.

Table 2.5: Summary of the T0 trigger ('93).

Mode	Top Low	Top High	Bottom Low	Bottom High	Ext	Count Down	Single Rate	T0 Out
T0 Low	1	*	1	*	*	1/1	2.3 kHz	2.3 kHz
T0 High	*	1	*	1	*	1/1	610 Hz	610 Hz
T0 gamma	0	0	1	*	*	1/256	19 kHz	70 Hz
T0 extern	*	*	*	*	1	0	0	0

1 : Signal should be asserted.
0 : Signal should be negated.
* : Signal is not concerned.

T0 Trigger

The T0 trigger process is done by the T0 trigger module which is controlled by CAMAC commands. The T0 trigger signal comprises four modes for the different physics targets. The first mode is a "T0 Low" aimed for single-charged particles. This mode requires both top and bottom scintillators signal above the low threshold of the 2LD. The second one is a "T0 High" for multiple charged particles. This mode requires both the top and bottom scintillators above the high threshold. The third one is a "T0 gamma" for gamma rays. Gamma-rays can be detected when they are converted to e^+e^- pair at the upper part of the MAG. To accept the events with such a configuration, this mode requires that there is null hit in top scintillators and at least one hit in bottom scintillators. The last one is a "T0 external" which is generated synchronously by the external pulse. This is only used for the calibration.

Logical-OR signal of those four modes initiates data gathering and the track trigger process. The T0 trigger module then locks out the further trigger process until the data acquisition cycle is completed.

The T0 trigger module is equipped with the CD logic for all modes to reduce the trigger rate unconditionally. If the count down number N_{cd} is set for a certain mode, trigger output comes once every N_{cd}. In all science flights, a countdown number of 256 was selected for the "T0 gamma" mode to reduce the event rate from 20 kHz to 80 Hz. For "T0 Low" and "To High", the count down number is unity to accept all events at this level.

Table 2.5, 2.5, 2.5 summarize the T0 triggers and their trigger rates in the three science flights.

Track Trigger

Fig 2.33 shows the basic concept of the TT. First the sense wire signals of each layer are discriminated and fed into the coincidence (COIN) modules. They are then combined into "cell-hit" signals by requiring the coincidence in both layers to

Table 2.6: Summary of the T0 trigger ('94).

Mode	Top Low	Top High	Bottom Low	Bottom High	Ext	Count Down	Single Rate	T0 Out
T0 Low	1	*	1	*	*	1/1	2.2 kHz	2.2 kHz
T0 High	*	1	*	1	*	1/1	340 Hz	340 Hz
T0 gamma	0	0	1	*	*	1/256	18 kHz	70 Hz
T0 extern	*	*	*	*	1	0	0	0

Table 2.7: Summary of the T0 trigger ('95).

Mode	Top Low	Top High	Bottom Low	Bottom High	Ext	Count Down	Single Rate	T0 Out
T0 Low	1	*	1	*	*	1/1	2.0 kHz	2.0 kHz
T0 High	*	1	*	1	*	1/1	260 Hz	260 Hz
T0 gamma	0	0	1	*	*	1/256	18 kHz	70 Hz
T0 extern	*	*	*	*	1	0	0	0

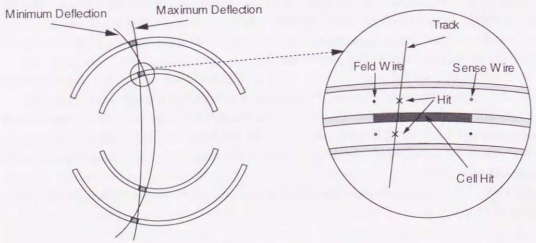

Figure 2.33: Basic scheme the track trigger

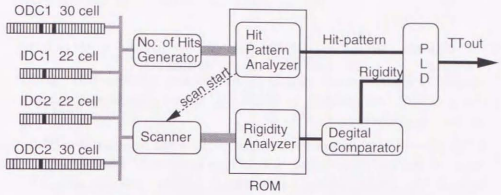

Figure 2.34: Block diagram of TT process.

eliminate spurious hits caused by electronics noise or local radio-active sources. Total of 30 and 22 cell-hit signals are generated for each ODC and IDC, respectively. Each cell-hit gives coarse position information by the precision of the cell size, i.e. , about 50 mm. A Combination of three or four cell-hit positions provides rough estimation of the rigidity of the track. The two tracks in Fig. 2.33 illustrate the maximum and the minimum possible deflection ($\equiv$rigidity^{-1}) for a certain combination of cell-hits. We define a deflection of the cell-hit combination as the mean value of these two deflections. By calculating the deflection for all cell-hit combinations and storing them in the look-up table beforehand, a quick rigidity analysis is possible without any time-consuming calculation.

A Track Trigger (TT) module carries out these tasks using a 2-Mbyte read-only memory (ROM) and a microcode-programmable sequencer (Fig. 2.34). The TT module selects events in two stage; hit-pattern selection and rigidity selection as follows:

- hit-pattern selection

  To eliminate the cell combination which have no possible track or too many hits to scan, event selections based on the cell-hit pattern are applied.

  They are divided into following eight categories depending on the number of cell-hits in the upper ODC (ODC1), upper IDC (IDC1), lower IDC (IDC2), and lower ODC (ODC2):

  1. $\bar{p}$ clear : only one hit in each chamber (1111).
  2. $\bar{p}$ dirty : two hits in one chamber, and only one in others (1112_p).
  3. $\bar{He}$ clear : only one hit in each chamber (1111).
  4. $\bar{He}$ dirty : two hits in one chamber, and only one in others (1112_p).
  5. Missing : no hit in one chamber and one in others (0111_p).
  6. Multi clear : multi-hits in the IDC2 and ODC2 (1113,1123,1124)

7. Multi dirty : two hits in ODC1 and multi-hit in the IDC2 and ODC2 (2113, 2123...).
8. Gamma : no hit in ODC1 and one or two in others (0111~0222).

where four digit numbers denote the number of cell-hits in the ODC1, IDC1, IDC2, ODC2, respectively, and suffix 'p' means that a permutation of these numbers is allowed.

A "number of hits generator" calculates the total number of cell-hits for each chamber and feed them into a "hit-pattern analyzer". The hit-pattern analyzer looks-up the ROM content and examine whether the hit-pattern belongs to any of the above categories. If the pattern is acceptable, a "scan-start" signal is sent to the scanner to initiate the rigidity analysis.

Most of the shower events or empty JET events are rejected by this selection.

- Rigidity selection

  The events that have passed through the hit-pattern selection are then subject to the rigidity selection. All possible combinations of cell-hits are scanned and fed to the rigidity analyzer, which is the other half of the ROM look-up table. The output deflection is digitally compared to the seven threshold values, each of which corresponds to the hit-pattern category, except that the thresholds for Multi-clear and Multi-dirty are common. If the deflection is above some of the thresholds, i.e., the track has more negative deflection than the threshold, TT signals are generated. The resultant eight signals, which correspond to the eight categories, are fed into the T1 trigger module to be combined with charge information from the TOF.

Figure 2.35 shows the efficiency of the rigidity selection as a function of deflection calculated by the simulation. The threshold values indicate the deflections where the efficiency become 50%. The left figure is for the threshold used for the $\bar{p}$ selection in the '93 flight. The right figure is for the threshold used for an antihelium selection. The curve for the $\bar{p}$ selection is set being shifted to the negative direction compared to that for the antihelium selection because a large number of protons should be cut more tightly by the rigidity selection.

T1 Trigger and Fast Clear

The TT only concerns the number of cell-hits and deflection of the track. The T1 trigger module combines the charge information from the T0 trigger module and the track information from the TT.

The T1 trigger module generates also unbiased trigger signals which bypass the TT selection. Each T1 trigger output reduced the number via a CD logic as is done in the T0 trigger module.

Finally the T1 trigger signal is generated as ORed signal of above twelve signals. If no T1 trigger signal is generated, a fast clear signal is sent to a "fast clear" module.

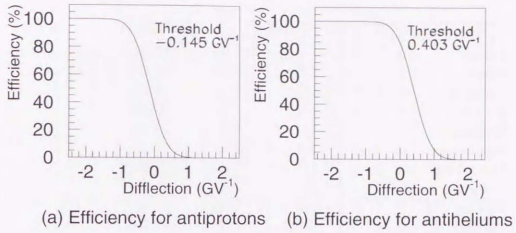

(a) Efficiency for antiprotons (b) Efficiency for antiheliums

Figure 2.35: Track trigger efficiency (a) for an $\bar{p}$ search (b) for an antihelium search.

The fast clear module sends the clear signal to all FADC and CAMAC modules and end up its task by unlocking the T0 module to accept the next event.

Table 2.8, 2.9, 2.10 summarize T1 trigger modes, their CD factors, and their trigger rates in the three scientific flights.

2.8.2 Event Processing with Transputer

Figure 2.36 shows a block diagram of event processing. The shadowed boxes are transputers[1], each of which has a processing speed of 20 MIPS and a carrying out capability of parallel tasks with the hardware. Total 20 transputers are used in the FADC system, the CAMAC system, the event builder (EVB), and the transputer bank.

Each transputer is connected via a serial bus line "serial link", which has maximum transmitting rate of 1 Mbyte/s. Four links equipped in each transputer can be configured in a versatile and flexible manner to construct a complicated network. The command line and the event data line are divided in the most part of this system and the command can be received or issued while transmitting the event data. In addition, the rapid data transmission is easily achieved since a link connects directly one transputer to another and there is no need for arbitration of the data way.

Thus, all transputers work concurrently and cooperatively to realize a fast event processing.

[1]product of INMOS corp.

Table 2.8: Summary of T1 trigger ('93).

T1 Mode	T0 Trig			CD	Trig rate[a]	Trig rate[b]
$\bar{p}$ clear	0	1	0	1/1	12 Hz	12 Hz
$\bar{p}$ dirty	1	1	1	1/1	18 Hz	18 Hz
He clear	0	1	0	1/1	3 Hz	3 Hz
He dirty	0	0	0	1/1	6 Hz	6 Hz
Missing	1	0	1	1/1	3 Hz	3 Hz
Multi clear	0	0	1	1/1	16 Hz	16 Hz
Multi dirty	0	0	0	1/1	8 Hz	8 Hz
Gamma	0	0	1	1/1	1 Hz	1 Hz
T0 Low CD	1	0	0	1/140	1.7 kHz	12 Hz
T0 High CD	0	1	0	1/40	500 Hz	12 Hz
T0 Gam CD	0	0	1	1/100	50 Hz	0.5 Hz
T0 Ext CD	–	–	–	–	–	–

[a]Before count down
[b]After count down

Table 2.9: Summary of T1 trigger ('94).

T1 Mode	T0 Trig			CD[a]	Trig rate[b]	Trig rate[c]	CD[d]	Trig rate[e]	Trig rate[f]
$\bar{p}$ clear	0	1	0	1/1	30 Hz	30 Hz	1/1	21 Hz	21 Hz
$\bar{p}$ dirty	1	1	1	1/1	14 Hz	14 Hz	1/1	10 Hz	10 Hz
He clear	0	1	0	1/1	11 Hz	11 Hz	1/1	10 Hz	10 Hz
He dirty	0	0	0	1/1	8 Hz	8 Hz	1/1	7 Hz	7 Hz
Missing	1	0	1	1/1	9 Hz	9 Hz	1/1	10 Hz	10 Hz
Multi clear	0	0	1	1/1	32 Hz	32 Hz	1/1	24 Hz	24 Hz
Multi dirty[g]	0	0	0	1/1	–	–	1/1	–	–
Gamma	0	0	1	1/1	1 Hz	1 Hz	1/1	1 Hz	1 Hz
T0 Low CD	1	0	0	1/60	1.4 kHz	23 Hz	1/120	1.6 kHz	13 Hz
T0 High CD	0	1	0	1/15	200 Hz	14 Hz	1/30	220 Hz	7 Hz
T0 Gam CD	0	0	1	1/100	40 Hz	0.4 Hz	1/100	40 Hz	0.4 Hz
T0 Ext CD	–	–	–	–	–	–	–	–	–

[a]first half of flight
[b]Before count down
[c]After count down
[d]last half of flight
[e]Before count down
[f]After count down
[g]Multi dirty was not used

Table 2.10: Summary of T1 trigger ('95).

T1 Mode	T0 Trig			CD	Trig rate[a]	Trig rate[b]
$\bar{p}$ clear	0	1	0	1/1	34 Hz	34 Hz
$\bar{p}$ dirty	1	1	1	1/1	27 Hz	27 Hz
He clear	0	1	0	1/1	11 Hz	11 Hz
He dirty	0	0	0	1/1	10 Hz	10 Hz
Missing	1	0	1	1/100	8 Hz	0.1 Hz
Multi clear	0	0	1	1/3	16 Hz	16 Hz
Multi dirty[c]	0	0	0	1/1	–	–
Gamma	0	0	1	1/10	1 Hz	0.1 Hz
T0 Low CD	1	0	0	1/90	1.2 kHz	13 Hz
T0 High CD	0	1	0	1/20	260 Hz	8 Hz
T0 Gam CD	0	0	1	1/256	43 Hz	0.2 Hz
T0 Ext CD	–	–	–	–	–	–

[a]Before count down
[b]After count down
[c]Multi dirty was not used

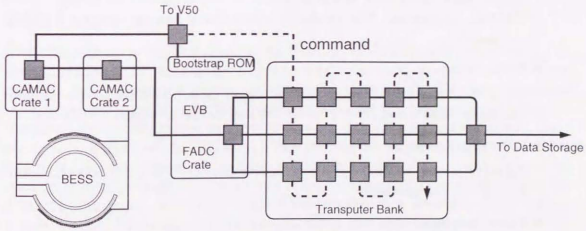

Figure 2.36: The block diagram of the data processing system using transputer network.

FADC System

The FADC system is comprised of a crate controller, FADC modules, and a compressor module. A FADC module has sixteen channels. Fifteen and Sixteen FADC modules are installed in '93 flight and '94 flight respectively.

The FADC modules read data from the JET chamber and the IDC, and convert them into 8-bit digit in the 35 ns sampling. The digitized data are successively accumulated in the fast-in-fast-out (FIFO) after zero-suppression. The compressor module then reads, compresses and writes the data to another FIFO. The transputer controls the FADC and compressor modules. If the crate controller receives the T1 trigger signals, the transputer transfers the data from the FIFO to the EVB. Otherwise a fast clear signal is received and then all modules are reset to the initial state.

CAMAC System

The CAMAC system consists of two CAMAC crates. Each crate is controlled by an intelligent crate-controller, which employs a transputer inside [31]. Thanks to transputer, two crate controllers can gather and transfer data in parallel at high speed.

In the crates, the following modules are installed and controlled by the crate-controller.

- Read-out electronics for the TOF counter and the ODC

  The discriminators, TDCs, and ADCs convert signals from the TOF and the ODC into the digital data.

- Trigger modules (T0, TT, T1)

  Trigger parameters such as CD numbers or TT thresholds are configured via CAMAC commands. The resultant trigger status can be read via CAMAC commands.

- 24-bit scalars

  Total 24-channel scalars count various trigger rates, which are used to monitor the trigger status and later used for the calculation of trigger efficiencies.

- Event-timing module

  An event-timing module includes a milli-second clock and measure the event-timing by 1-ms precision.

- Gate generators

  Gate generators are passive modules, i.e. , not controlled by CAMAC. They generate the gates with various widths and delays for use in other modules.

All data from above modules are transferred to the EVB via serial links.

Event Builder (EVB)

The data collected individually by the CAMAC and FADC system are fed to the EVB through the serial links. The EVB merges these data into the event structure. The event-building processes can be executed in parallel with the data-gathering process by the CAMAC and FADC crate-controller. The event data has a size of 1 kbyte typically and the EVB can handle them 1 kbyte per 1 ms, i.e., the maximum processing cycle of the EVB is 1 kHz. The built data are sent to the transputer bank for further processing.

Transputer Bank

The transputer bank receives the data from the EVB through three serial links. Fifteen transputers are arranged in a matrix way and process the event data simultaneously. All transputers execute the same program to process an event, which is flown from the up-stream to the down-stream. If the up-stream transputer is busy, the event data is passed to the down-stream transputer in sequence.

The main role of the transputer bank is to clean up and sieve the event data using the whole detector information. Events with null data of the TDCs and small hits of FADC are removed here. The processes also reject events using inconsistency between IDC and ODC hits and TOF hits, events with less than 8 JET hits, and events with data sizes of more than 3 kbyte. About 2% event rate are reduced by these processes. Each transputer executes the above task in 20 ms and therefore the whole bank can accept the event rate of 1 kHz.

In addition to the filter process, one of the transputer makes various histograms concerning the filter processes. The resultant histograms are sent to the ground together with CAMAC scalar data in a second interval. These histograms are utilized to watch the status of the triggers and event filtering.

2.8.3 Data Storage

The data storage subsystem receives the data via OMNI-net and serial links. The event-, monitor-, and message-data from each subsystem are recorded into the 8-mm magnetic tape. Three transputers are employed for this task. The first transputer receives the command and the data from the OMNI-net and then sorts and transmits them into the second transputer through another link. The second transputer plays a role as a buffer, which receives commands from one link and data from other two links, and send them to the third transputer though the last link. The third transputer interprets the commands and then controls a SCSI bus for recording the data. The maximum recording rate is 500 kbyte/s, which is limited by the SCSI bus transfer speed. The maximum storage capacity is 10 Gbyte in two tapes.

2.8.4 Communication

A communication subsystem manages communication between the payload and the ground station. The communication is carried out through the CIP, which provided

by the national scientific balloon facility (NSBF). The commands to the DAQ are transmitted from the ground to the CIP via a radio link. The CIP converts the commands into 16-bit parallel data and send them to the communication subsystem. On the other hand, the message data and the event data are sent to the CIP via a serial line and then transmitted to the ground station through another channel of the radio link.

Although the maximum rate of transmission to the ground is 10 kbyte/s, the event data are transferred by a rate of 0.1 Hz, i.e., 100 byte/s with some margins. Commands are sent by a rate of 1 byte/s.

2.8.5 Monitor

A monitor subsystem handles the house-keeping data from the sensors. The monitor module has 64 individual differential-amplifiers and one analog-to-digital converter to digitize various sensor signals: temperatures (16 points), pressures (10 points), a magnet status (16 points), a chamber high voltage status (10 points), and a solar sensor and clinometers. The digitized data are transmitted to the ground station via the radio link and utilized to check the detector status during the flight.

Chapter 3

Scientific flights

This chapter describes the courses of the BESS '93, '94, and '95 scientific flights and the house keeping data during the flights.

3.1 BESS '93 scientific flight

BESS was successfully launched by a balloon from Lynn Lake, Manitoba, in Northern Canada, on Jul. 26 in 1993, which was a first scientific flight of BESS. The balloon of 29 Mf^3 lifted BESS into an altitude of 36.5 km (residual atmosphere of 5 g/cm^2) for 17 hours and conveyed it to Peace River which located 1000 km east from Lynn Lake. During this level flight, a scientific data taking run were carried out for 13 hours. Total of 10^8 charged cosmic rays were triggered at T0 level and 3.6×10^6 of these triggers were recorded. After the scientific run, the balloon flight was terminated by cutting off balloon under the condition of both magnetic field and power off. The BESS instrument was landed by parachute and was safely recovered by the next day. Figure 3.1 shows a balloon trajectory of '93 flight. The latitude varied from 56°48'N to 57°52'N while longitude from 101°25'W to 117°30'W. The corresponding cut-off rigidity varied from 0.34 GV to 0.43 GV.

Figure 3.3 illustrates a change of the magnetic field strength and typical temperatures during the flight. The temperature at the center of the detector varied between 10°C and 38°C. Figure 3.2 shows gravitational acceleration at the moment of launching, termination , landing, and during recovery. The maximum value of acceleration was 11.7 g at the landing. With all rigorous operating conditions, no significant damage was observed both in the structure and in the performance according to the check after the recovery.

3.2 BESS '94 scientific flight

In the '94 instrument, a Čerenkov counter was added outside of the pressure vessel, however, the flight procedure was very similar to the previous one. BESS was successfully launched by a balloon from Lynn Lake air port, at 21:30 local time on Jul. 31, in 1994. The balloon lifted BESS into the altitude of 36.5 km (residual

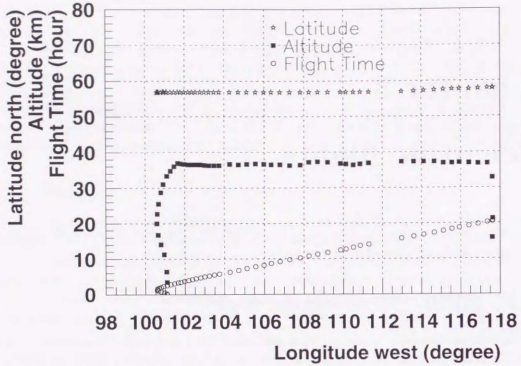

Figure 3.1: BESS '93 flight path in altitude, latitude vs. longitude

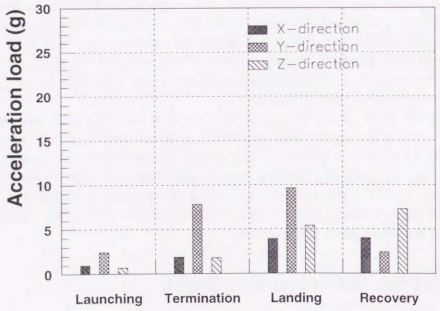

Figure 3.2: Acceleration loads during '93 flight.

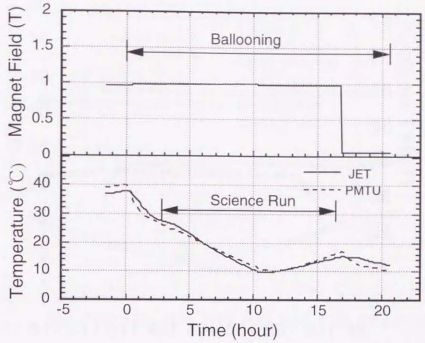

Figure 3.3: House-keeping data on magnetic field, temperature of TOF and Jet chamber.

atmosphere of 5 g/cm^2) for 23 hours. During the level flight, that includes 12 hours scientific data taking time, total of 10^8 charged cosmic rays were triggered at T0 level and 4.7×10^6 events were recorded. The instrument was landed by parachute near Slave lake in Peace River, and BESS was safely recovered within two days. Figure 3.4 shows a balloon trajectory of BESS '94 scientific flight. The latitude varied from 56°48'N to 55°89'N while longitude from 101°25'W to 114°06'W.

Figure 3.5 shows gravitational acceleration at the moment of launching, termination , landing, and during recovery. The maximum value of acceleration was 29 g at the termination. During the recovery, the instrument was carried crossing a creek which was running between the landing point and the road. Because a bottom part of the vessel were submerged, the power supply unit and Čerenkov counter, which were installed outside the vessel, were partially damaged. After the carriage to Japan, they were carefully fixed. The detectors inside the vessel were completely safe. Finally it was confirmed that no significant damage was observed both in the structure and in the performance according to thorough checks.

3.3 BESS '95 scientific flight

The third scientific flight of BESS was also successfully performed. The launching was done at Lynn Lake, at 21:04 on Jul. 25, in 1995. During the level flight, the altitude was also 36.5 km (residual atmosphere of 5 g/cm^2). After 24 hours flight,

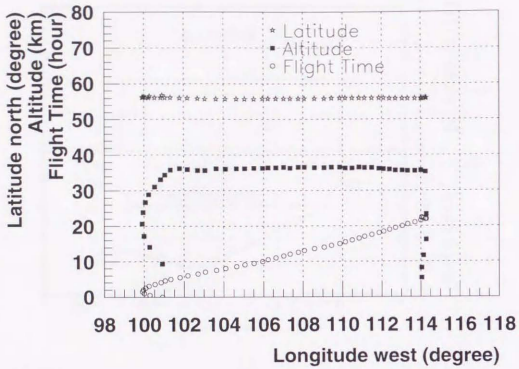

Figure 3.4: BESS '94 flight path in altitude, latitude vs. longitude

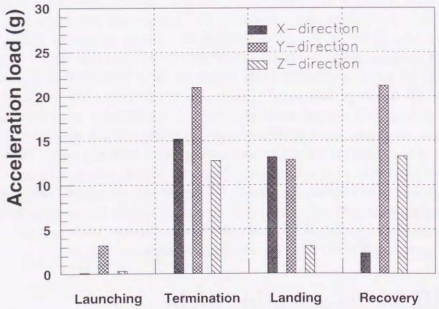

Figure 3.5: Acceleration loads during '94 flight.

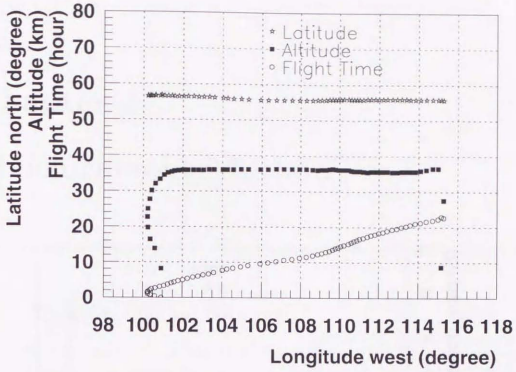

Figure 3.6: BESS '95 flight path in altitude, latitude vs. longitude

that includes 14 hours scientific data taking time, the instrument was landed to the east of Peace River. The BESS instrument was safely recovered in two days. Total of 10^8 charged cosmic rays were triggered at T0 level and 4.6×10^6 events were recorded. Figure 3.6 shows a balloon trajectory of BESS '95 scientific flight. The latitude varied from 56°51'N to 55°32'N while longitude from 101°04'W to 115°06'W. Figure 3.7 shows gravitational acceleration at the moment of launching, termination , landing, and during recovery. The maximum value of acceleration was 26 g during the recovery. No significant damage was observed both in the structure and in the performance according to the check after the recovery.

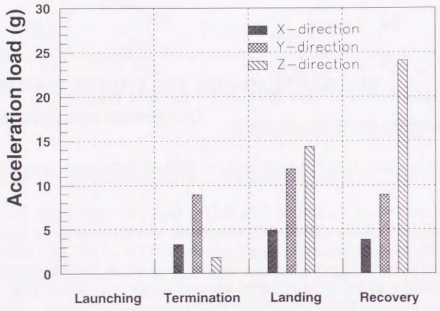

Figure 3.7: Acceleration loads during '95 flight.

Chapter 4

Measurement Method

This chapter provides an overview of measurement methods of rigidity, timing, and dE/dX.

4.1 Rigidity Measurement

A rigidity of the particle is measured by the JET and IDCs. First the transverse rigidity (R_t), i.e., the rigidity component perpendicular to the magnetic field direction is determined by a circular fitting in the $r\phi$ plane (Fig. 4.1 (a)). We use the following algorithms to eliminate the unconnected hits to the track in the fitting process.

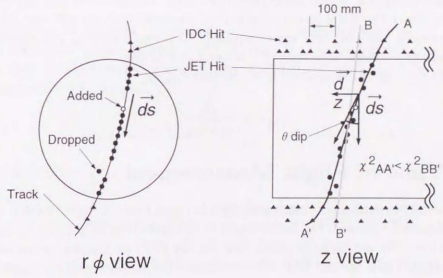

Figure 4.1: Method of the rigidity measurement.

1. Select good hits, which are defined as hits with enough charge and width, in the JET chamber and the IDCs.

2. Find tracks by connecting the good hits in the JET chamber and perform circular fitting using them.

3. Extrapolate the track to the IDC. If there are any good IDC hits near the extrapolated track, they are associated to the track.

4. Perform the circular fitting again using all hit points in the JET and IDCs which are associated to the track. We use a "KARIMAKI method"[33] for the fitting algorithm at this stage.

5. Scan all of good hits in the JET chamber and check if they are well near the track, i.e., within 5 times the distance of the position resolution. If the hit has a residual error of more than 5 σ, it is discarded. On the contrary, if the hits that are not yet associated to any track are laid within 5 σ from the track, it is added to the track.

6. Repeat step 4) and 5) twice.

The resultant R_t should be then corrected for non-uniformity of the magnet field of about 10%. From detailed study using M.C. simulation in the exact magnetic field, the correction using the simple function of the track position, path length, and mean strength of B field is found to be able to correct the rigidity within an accuracy of 1%.

To convert R_t into the total rigidity (R), we find the dip angle $\theta_{\rm dip}$, which is defined as an angle between the $r\phi$-component ($\vec{ds}$) and the z-component ($\vec{dz}$) of R, by fitting in the yz plane (Fig. 4.1). We use a similar iterative procedure as used in the $r\phi$ fitting to eliminate irrelevant hits. The selected hits are fitted to a sine-curve. Since the IDCs provide the only z positions modulo 100 mm, all possible combinations of the IDC hits are examined. The resultant $\theta_{\rm dip}$ are obtained from the combination having minimum χ^2 value in the fitting.

Finally rigidity R are derived from R_t and $\theta_{\rm dip}$ as,

$$R = \frac{R_t}{\cos\theta_{\rm dip}}.$$

4.2 Time of Flight Measurement

Figure 4.2 illustrates the measurement scheme of time-of-flight (TOF). The TOF between top and bottom TOF hodoscopes is calculated for each track by the following procedure. We use here the suffix 'elec' for the PMT on the side of the electronics and the suffix 'tank' for the PMT on the side of the helium reservoir tank.

1. Correct a timing walk using the charge information for each PMT. We use following formula:

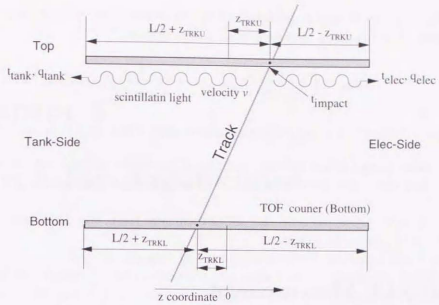

Figure 4.2: Method of the TOF measurement.

$$\hat{t}_{\rm elec} = t_{\rm elec} - a\sqrt{q_{\rm elec}},$$

and

$$\hat{t}_{\rm tank} = t_{\rm tank} - a\sqrt{q_{\rm tank}},$$

where $t_{\rm elec,tank}$ is the measured timing, $\hat{t}_{\rm elec,tank}$ the timing after the correction, q the measured charge of the PMT. Parameter a was determined by the beam test.

2. Derive the timing that the particle passed through the counter ($t_{\rm impact}$) from the corrected timing of each PMT. Using the z-impact point ($z_{\rm trku}$, $z_{\rm trkl}$) of the particle which is calculated by extrapolating the combined track, $t_{\rm impact}$ is obtained for elec-side as,

$$t_{\rm impact\_elec} = \hat{t}_{\rm elec} - \frac{\frac{L}{2} - z_{\rm trku,trkl}}{v_{\rm eff}} - t_{\rm offset}(z_{\rm trku,trkl}),$$

and for tank-side as,

$$t_{\rm impact\_tank} = \hat{t}_{\rm tank} - \frac{\frac{L}{2} + z_{\rm trku,trkl}}{v_{\rm eff}} - t_{\rm offset}(z_{\rm trku,trkl}),$$

where $v_{\rm eff}$ is the effective light velocity in the counter and L is the length of the paddle. The second term is the propagation time for the scintillation light to reach to each PMT. The last term $t_{\rm offset}(z)$ is the timing offset as a function of the z position. This is introduced to correct the velocity variation depending

on the z position and is determined by calibration for each counter. Timing of both sides are then averaged with the weight as,

$$t_{\text{impact}} = \left(\frac{1}{\sigma_{\text{elec}}(z)^2} t_{\text{impact\_elec}} + \frac{1}{\sigma_{\text{tank}}(z)^2} t_{\text{impact\_tank}} \right),$$

where $\sigma(z)$ is the timing resolution of the each PMT as a function of z.

3. The value t_{impact} is individually calculated for both top and bottom counters, and then the TOF is obtained as the time difference between them.

The $\beta \equiv v/c$ of the particle can be determined from the TOF and the path length calculated from the track.

4.3 $\mathrm{d}E/\mathrm{d}X$ Measurement

The $\mathrm{d}E/\mathrm{d}X$ of the particles in the scintillator is derived from charge value measured by each PMT as following:

1. Subtract the pedestal value from the measured charge value and correct the gain difference for each PMT.
2. Correct the z dependence of the signal amplitude due to the attenuation or loss of scintillation light using the z-impact position of the track. The detailed study in the beam test shows that the measured charge (q_{measured}) has the z-dependence as follows:

$$q_{\text{measured}} \propto a + be^{cz},$$

where a, b, c are parameters that should be determined by the calibration.

3. Average the charge value of PMTs at both ends after the correction of step 2.
4. Divide the averaged charge value by the path length in the scintillator through which the particle passed. This gives $\mathrm{d}E/\mathrm{d}X$ in the TOF counters.

We finally normalize the $\mathrm{d}E/\mathrm{d}X$ such that the mean value of the $\mathrm{d}E/\mathrm{d}X$ distribution for the minimum ionizing particles is unity.

Chapter 5

Search for Antihelium

This chapter provides the analysis to search for antiheliums using the BESS '93, 94, and '95 flight data. § 5.1 summarizes the data sample taken in the three flights. § 5.3 shows the method to process the flight data. Before search for antiheliums, preselection described in § 5.4 is applied. This rejects potential backgrounds due to the mis-measurement of the rigidity and TOF. The general performances are presented in § 5.5 using the data samples which pass through the preselection. Section 5.6 describes the method of albedo event rejection which separates downward moving particles from upward moving particles. The β cut is applied to extract events with charge/mass = 2 in § 5.7. Section 5.8 provides identification of heliums and antiheliums using $\mathrm{d}E/\mathrm{d}X$ selection, which select events of particle with charge = 2. By the sample which passed through all the above mentioned selections, antihelium search is done in § 5.9.

5.1 Flight Data Sample

Trigger parameters (CD factors and TT thresholds) were carefully adjusted to the design values using the data taken in the short pilot run just before the level flight. One-third of the triggers were the unbiased events which bypassed the TT and two-thirds were biased events selected by the TT.

An on-line pedestal run was carried out to re-adjust the FADC threshold every 1 hour during the all flights because the FADC module has a slight temperature dependence. In addition, all calibration parameters, such as a timing conversion gain or a chamber drift velocity, varies according to the drifts of the temperature and pressure. They have to be calibrated in a short interval. Thus all data samples are divided into some data sets such that each data set includes at least 1 pedestal run. Table 5.1, 5.2, and 5.3 summarize the number of data in each run and flight.

In the tables "T0 lock" denotes the number of the events which were triggered at T0 level and started the TT process. "T1 accept" is the number of the events which were accepted by the T1 trigger logic and initiated the data gathering. The right side of the tables show the breakdown of the recorded data, each of which corresponds to the T1 trigger mode (see Table 2.8, 2.9, and 2.10).

Table 5.1: Summary of BESS '93 flight data

run #	DAQ time	T0 lock	T1 accept	Record	$\bar{p}$ total	He total	others	T0 low CD	T0 high CD
13	3293	5819205	288681	284358	101362	28725	154271	40914	41861
14	2801	4949154	245070	241298	87358	24904	129036	34913	35662
15	3802	6695102	330457	325301	117514	32906	174881	47113	48065
16	2903	5108301	251336	247685	88783	24553	134349	35968	36635
17	3541	6246253	298337	293602	104476	28254	160872	43980	44639
18	4207	7382223	349531	343572	121234	32144	190194	52182	52382
19	4062	6929533	344137	339427	112146	27699	199582	48913	48979
20	4580	7723902	389954	383187	136519	36454	210211	54747	54824
21	3457	5889110	309112	303837	108311	30210	165316	41524	41395
22	2156	3665944	193283	189993	67299	19292	103402	25899	25546
23	3529	5410472	287415	314841	111536	32162	171143	42436	41789
24	4057	6887654	374161	368041	135373	39474	193194	48532	47400
total	42389	72706853	3661474	3635139	1291911	356777	1986451	517121	519177

Table 5.2: Summary of BESS '94 flight data

run #	DAQ time	T0 lock	T1 accept	Record	$\bar{p}$ total	He total	others	T0 low CD	T0 high CD
6	3810	5505364	537204	526430	210467	89431	226532	92854	54091
7	3213	4661007	454352	445217	175695	76826	192696	78500	46389
8	3044	4417817	430768	421951	165701	72373	183877	74633	43811
9	3317	4721082	461355	451795	176277	78404	197114	79524	47003
10	3735	5412926	523350	511076	195241	89338	226497	91219	53888
13	2163	3156732	300536	292578	108222	52605	131751	53076	31271
15	3111	4978340	323482	318214	161072	81726	75416	41215	23745
16	5441	8760763	554306	544908	272781	142735	129392	72444	40912
17	3138	4999147	313612	308027	153233	81598	73196	41242	22996
18	2340	3804162	236192	232048	115504	61165	55379	31348	17091
19	3495	5674366	351575	345340	171464	91749	82127	47036	25349
20	3273	5330760	329730	323804	161115	85655	77034	44125	23545
total	40079	61422466	4816462	4721388	2066772	1003605	1651011	747216	430097

Table 5.3: Summary of BESS '95 flight data

run #	DAQ time	T0 lock	T1 accept	Record	$\bar{p}$ total	He total	others	T0 low CD	T0 high CD
7	3259	4406346	358689	356528	211541	71191	73796	48724	26164
8	3409	4524813	368222	366205	216744	73917	75544	49884	27347
9	2559	3121620	254576	253159	149148	51464	52547	34325	19239
10	2557	3097168	250387	247125	144716	50138	52271	34104	19157
11	3910	4817987	389034	386605	225634	79062	81909	53262	30194
12	4414	4152285	335065	333336	194111	68980	70245	45723	25906
13	3109	3815047	306728	305143	177536	63102	64505	42008	23648
14	475	612989	49167	48937	28452	9935	10550	6770	3729
15	3605	4769170	381353	379440	221300	77575	80565	52641	28578
16	3200	4385297	349405	347483	202518	70703	74262	48480	25961
17	3320	4421076	352546	350943	204805	71409	74729	48783	25700
18	3344	3944596	312631	307927	179565	62193	66169	43461	22443
19	5310	3888883	307297	299741	174957	60000	64784	42932	21515
20	2884	4075373	321395	316869	185721	63068	68080	44930	22143
22	2346	3306413	260483	256416	150665	51323	54428	36349	17841
total	47702	57339063	4596978	4555857	2667413	924060	964384	632376	339565

5.2 Dead time evaluation

The dead time of the BESS instrument is caused by two processes. One is the data gathering process, which gathers event data from all detectors and packs them into a formatted packet to be recorded, and the other is the fast clear process, which clears whole the data acquisition system when an event is rejected by the T1 trigger logic. The occurring rates of the fast clear and data gathering processes in Hz, and the total dead time can be obtained from the scalar. However, the fractional dead times by the data gathering and fast clear processes cannot be obtained separately from the scalar. In order to obtain these fractional dead times, we need some calculations. First, we have the following equation.

$$T_{\text{data}} \times R_{\text{data}} + T_{\text{fast}} \times R_{\text{fast}} = TDT \tag{5.1}$$

where

- T_{data} = Mean time consumed by a data gathering process in second.
- T_{fast} = Mean time consumed by a fast clear process in second.
- R_{data} = Occurring rate of data gathering process in Hz.
- R_{fast} = Occurring rate of the fast clear process in Hz.

Table 5.4: Summary of the dead time

flight year	data gathering	fast clear	DAQ error	dead time
'93	1.4 ms × 90 Hz = 0.13	84μs × 1.7 kHz = 0.14	–	0.27
'94 first half	1.8 ms × 150 Hz = 0.27	84μs × 1.3 kHz = 0.11	–	0.38
'94 last half	1.8 ms × 102 Hz = 0.18	84μs × 1.5 kHz = 0.13	–	0.31
'95	2.0 ms × 110 Hz = 0.22	84μs × 1.2 kHz = 0.10	0.08	0.40

- TDT = Total dead time.

Utilizing this equation and the fact that the trigger condition was changed in the middle of the BESS '94 flight, $T_{\rm fast}$ and $T_{\rm data}$ for the BESS '94 flight can be obtained. Because we know $R_{\rm data} = 150$ Hz, $R_{\rm fast} = 1.3$ kH, and $TDT = 0.38$ in the first half of the flight, and $R_{\rm data} = 102$ Hz, $R_{\rm fast} = 1.5$ kH, and $TDT = 0.31$ in the last half of the flight from the scalar, we have two independent equations as follows.

$$T_{\rm data} \times 150{\rm Hz} + T_{\rm fast} \times 1.3{\rm kHz} = 0.38 \quad (5.2)$$
$$T_{\rm data} \times 102{\rm Hz} + T_{\rm fast} \times 1.5{\rm kHz} = 0.31 \quad (5.3)$$

Resolving these equations gives $T_{\rm data} = 1.8$ ms and $T_{\rm fast} = 84\mu$s. Since $T_{\rm fast}$ should be the same among all flights, $T_{\rm data}$ for '93 and '95 flights can be obtained from equation 5.1 again. The dead times of the three flights are summarized in table 5.4.

These dead times for three flights are related to the status of the instruments during the flights. As for '94 flight, the chambers were noisy due to a bad gas condition and the average event data size increased. As a result, the mean data gathering time became longer than previous year. In BESS '95 flight, the doubled number of readout electronics for the new TOF hodoscope increased the data gathering time. In addition to this factor, DAQ errors happened due to one bad FADC channel and this caused another 8 % of dead time. Then, the total dead time amounted to 40 % in BESS '95 flight.

From the DAQ times in table 5.1 to 5.3 and the dead times obtained above, the live time in hour , i.e., the exposure time, can be obtained from an equation (exposure time) = (DAQ time) × (1 - dead time). The exposure times of the three flights are summarized in table 5.5.

5.3 Data Processing Method

The data recorded during a flight (RAW data) is composed of the event data, housekeeping data, command log, and message data in a compressed format. To analyze the data and then search for antihelium among them, we should process the RAW

Table 5.5: Summary of the exposure time

flight year	exposure time (hour)
'93	8.6
'94	7.3
'95	8.0

data to extract physics properties of each event. For this purpose, we utilized a ZEBRA system [32] due to following reasons:

- The ZEBRA system provides dynamical memory handling and enables to create the slots called BANK, which is useful for storing various information and processing.
- Data structure can be easily constructed hierarchically. We can develop the analysis routine for each detector according to the individual data structure.
- A data-base program (HEPDB) is available in the ZEBRA environment.

The first step of the data processing is to decompress and unpack the RAW data, and to convert them into a file in the ZEBRA format event by event (STEP 1 in Fig 5.1). This file, which has a size of 15 Gbyte for a flight, is called reformat (RFT) data file, and has only DA bank where only the RAW data is stored. Using the RFT data file, we performed rough calibration of each detector, and the resultant calibration parameters were stored in the data-base which can be managed by the HEPDB program (STEP 2). In the next step (STEP 3), data were processed with the calibration data, creating several banks and filling them with various information from detectors, such as hit positions or charges of hits etc. Such jobs were performed by analysis routines corresponding to each detector. The resultant data structure is composed of following eight banks:

- DA bank – RAW data.
- TR bank – Trigger information of the events.
- JC bank – Event information concerning the JET chamber.
- IC bank – Event information concerning the IDC.
- OC bank – Event information concerning the ODC.
- TF bank – Event information concerning the TOF.
- CK bank – Event information concerning the Čerenkov counter.
- SC bank – 24-channels of 24-bit scalar data.

- TK bank – Event properties using the whole detector information.

They were written into the zebra-formatted files as processed (PRC) data, which amounts to 100 Gbyte (STEP 3).

The PRC data contain useful information for physics analysis, however, the size is huge and costs of I/O handling are too high. The core information was extracted from each bank and stored into the Data summary tape (DST) as a fixed-formatted file (STEP 4). The main structure of the DST corresponds to the banks in the PRC data. Using the DST, detector performances were checked. If there were problems or improvements in calibration, then STEP 2 $\sim$ 4 were executed iteratively (STEP 5). In the present study, most parts of physics analysis were done using the DST data.

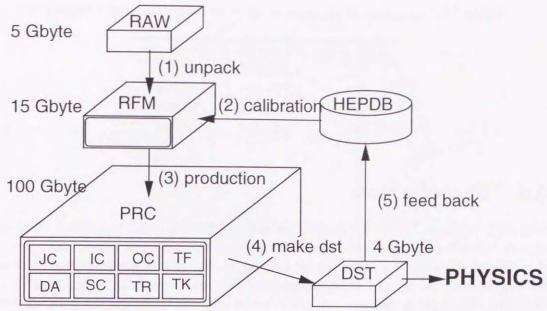

Figure 5.1: BESS data process method for one flight data.

Table 5.6: Summary of the number of events after the single track cut

flight year	All sample	CD sample
'93	1,968,974	163,454
'94	2,786,426	144,184
'95	2,946,843	116,091
Total	7,702,243	423,729

5.4 Preselection

The DST contains 12,912,384 events, including 1,288,833 "unbiased T0 high trigger sample" which were recorded irrespective of the track trigger conditions. Among them there are some events which do not exhibit the proper performance to search for antiheliums in certain reasons, such as the multi-track or interaction in the detector. We applied the selection prior to the analysis to ensure the good detector performance by rejecting those events.

5.4.1 Selection for Good Single Track

About half of the events exhibited either multi-tracks, or shower, or empty hit in the JET chamber. Following cuts were applied to reject these events and to select good single track events which passed through the fiducial region of JET chamber.

i) $N_{\rm track} = 1$.

Number of tracks found in the JET chamber should be exactly one.

ii) JET fiducial region cut.

The fiducial region of the JET chamber are defined in Figure 5.2 as not shadowed region. The shadowed region is close to the wall of JET chamber, where the distortion of the electric field is not negligible. Then in the shadowed region the position measurement is less accurate than the central region. The track found in the JET chamber should not touch through this shadowed region. This cut avoids the mis-measurement of rigidity, and then the mis-measurement of the sign of charge.

After this selection, we have exactly one track in an event to analyze. Total 7,702,243 events, including 423,729 unbiased trigger events, passed through this cut. Table 5.6 summarizes the number of events which passed the single track selection.

5.4.2 Track Quality Cut

Following cuts were then applied to ensure a good quality of the single track. The track were defined as the combined fit using hit points of the IDC and the JET chamber data.

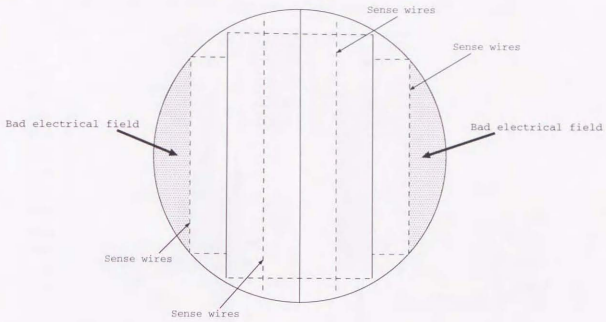

Figure 5.2: Fiducial region of JET chamber.

i) $N_{r\phi\rm fit} \geq 14$,

where $N_{r\phi\rm fit}$ is the number of JET hits used for the final track fitting in $r\phi$ plane.

ii) $\chi^2_{r\phi}$ cut.

$\chi^2_{r\phi}$ is the reduced chi-square of the combined fitting in $r\phi$ plane. In figure 5.3, figure 5.4, and figure 5.5, the cut positions of $\chi^2_{r\phi}$ are indicated in the solid lines for three-flight data. The $\chi^2_{r\phi}$ value should be below these curves and the cuts are rather tight in the high rigidity region. Histograms sliced by rigidity regions are shown in figure 5.6, 5.7, and 5.8. These cuts are slightly different among three flight data, because the calibration of chamber data depends on status of pressure and temperature of gas, which are changing through all runs and flights.

iii) $N_{\rm IDC1r\phi} \geq 1$, $N_{\rm IDC2r\phi} \geq 1$.

This requires that at least one good hit in each of upper two and lower two layers of IDCs are used in the $r\phi$ fitting.

Figure 5.3 to figure 5.4 show the histograms of these track-quality variables based on the jet chamber data together with the cut positions for '93, '94, and '95 flight data. Figure 5.9 shows track-quality cut based on IDC hit numbers for three-flight data combined. Open histograms are for the events that pass through the single-track selection, and the shadowed histograms are for the events that survived after

Table 5.7: Summary of the number of events after the track quality cut.

flight year	All sample	CD sample
'93	1,638,359	129,330
'94	2,217,787	111,661
'95	2,434,245	90,195
Total	6,290,391	331,186

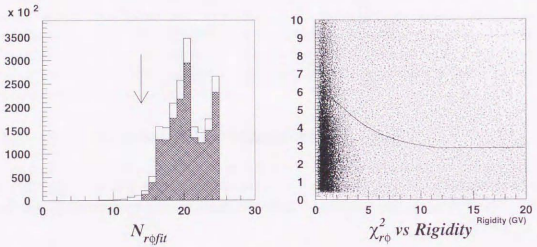

Figure 5.3: Track quality cut based of JET chamber ('93).

the track-quality cut. Total 6,290,391 events, including 331,186 unbiased trigger events, passed through these cuts. Table 5.7 summarizes the number of events which passed the track quality cut.

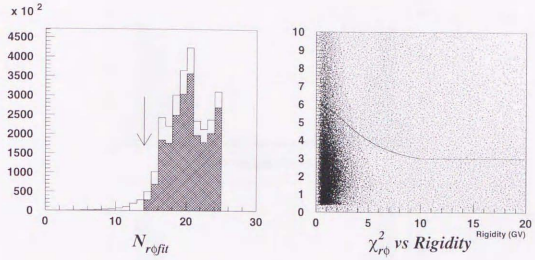

Figure 5.4: Track quality cut based on JET chamber ('94).

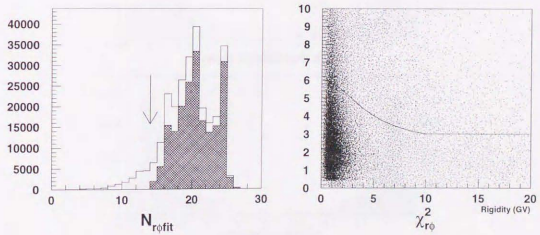

Figure 5.5: Track quality cut based of JET chamber ('95).

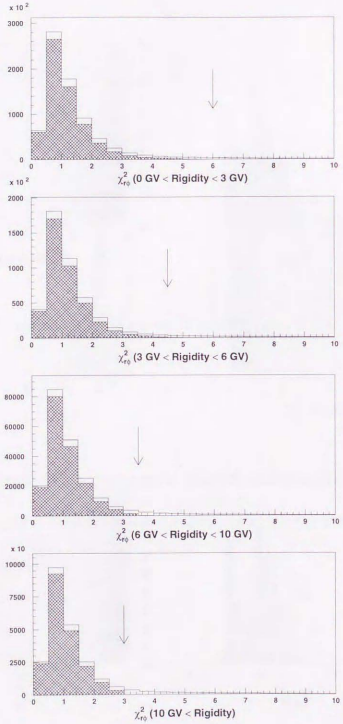

Figure 5.6: Sliced histogram of $\chi^2_{r\phi}$ cut. ('93).

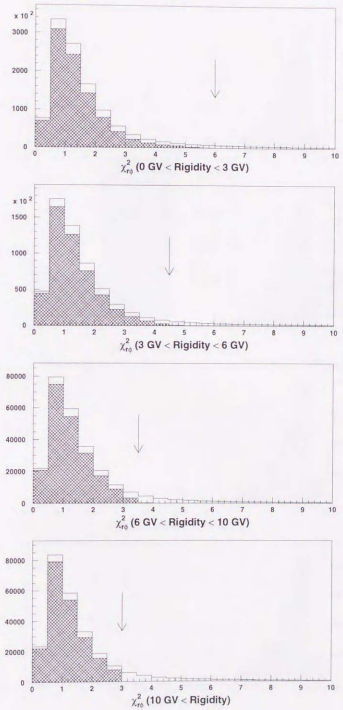

Figure 5.7: Sliced histogram of $\chi^2_{r\phi}$ cut. ('94).

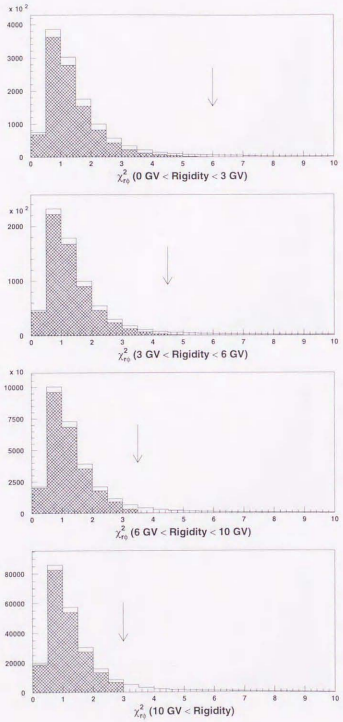

Figure 5.8: Sliced histogram of $\chi^2_{r\phi}$ cut. ('95).

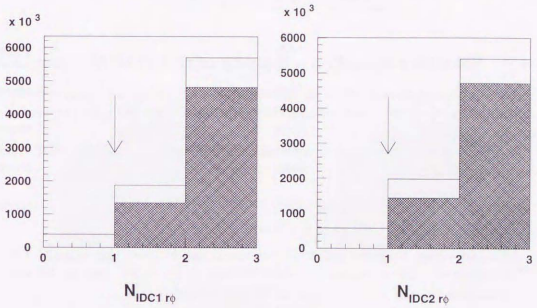

Figure 5.9: Track quality cut based on IDCs ('93+'94+'95).

Table 5.8: Summary of the number of events after the TOF quality cut.

flight year	All sample	CD sample
'93	1,356,730	100,038
'94	1,669,792	85,375
'95	2,134,983	79,814
Total	5,161,505	265,227

5.4.3 Selection Based on a Quality of the TOF Measurement

The timing measurements might be disrupted by the accidental particle or by the local radio-active source which hit the TOF scintillator together with the cosmic ray particle.

To ensure correct timing measurements, the following cuts on the TOF quality were applied at this stage.

i) $|z_{\mathrm{TRKU}}| < 500$ mm , $|z_{\mathrm{TRKL}}| < 500$ mm ('93,'94).

$|z_{\mathrm{TRKU}}| < 470$ mm , $|z_{\mathrm{TRKL}}| < 470$ mm ('95).

This requests that the extrapolated track should pass through the fiducial z-region of TOF scintillators, which extend to $|z| = 550$ mm in '93 and '94 instruments, and $|z| = 475$ mm in '95 instrument.

ii) $|z_{\mathrm{TOFU}} - z_{\mathrm{TRKU}}| < 100$ mm , $|z_{\mathrm{TOFL}} - z_{\mathrm{TRKL}}| < 100$ mm .

This requires that z determined by the left-right time difference matches the z-impact point of the extrapolated track within the resolution of z_{TOF}.

Figure 5.10 and 5.11 illustrate the histograms of these variables together with the cut positions for '93 and '94 flight data combined, and '95 flight data. Open and hatched histograms, respectively, are for the events which survived the single track selection and subsequently the track quality cut. Shadowed histograms are for the events that passed through all of the TOF quality cut, too. Total 5,161,505 events, including 266,277 unbiased trigger events, pass through these cuts. Table 5.8 summarizes the number of events which passed the TOF quality cut.

5.4.4 Summary of the Event Selection

Table 5.9 summarizes the selection criteria and the number of the events that survive after each stage.

5.5 General Data Quality after Preselection

The quality of the detector performance can be checked by utilizing the event sample that passed through the above selection.

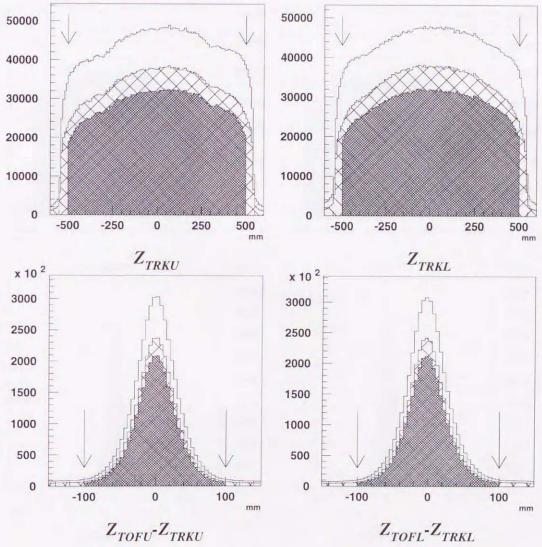

Figure 5.10: TOF quality cut ('93+'94).

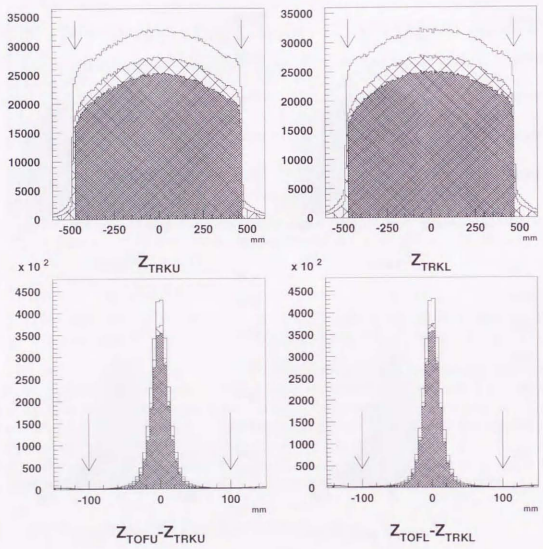

Figure 5.11: TOF quality cut ('95).

Table 5.9: Summary of preselection.

Cut No.	Variable	Quantity	No.of events (unbiased)
		Total Number of Events	
			12,912,384 (1,288,833)
		Good Single Track selection	
1.....	$N_{goodtrack}$	1	
2.....	JET fiducial region		
			7,702,243 (423,729)
		Track Quality Cut	
1.....	$N_{r\phi-fit}$	≥ 14	
2.....	$\chi^2_{r\phi}$		
3.....	$N_{IDC1_{r\phi}}, N_{IDC2_{r\phi}}$	≥ 1	
			6,290,391 (331,186)
		TOF quality Cuts	
1.....	$\lvert z_{TRKU}\rvert, \lvert z_{TRKL}\rvert$	< 500 mm ('93,'94), < 470 mm ('95)	
2.....	$\lvert z_{TOFU} - z_{TRKU}\rvert, \lvert z_{TOFL} - z_{TRKL}\rvert$	< 100 mm	
			5,161,505 (265,227)

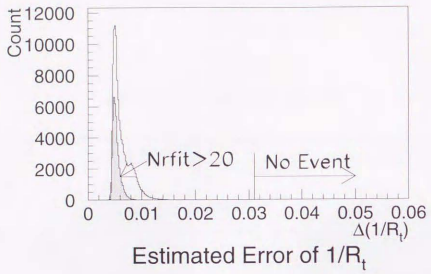

Figure 5.12: The estimated error of $1/R_t$ in the $r\phi$ fitting.

The estimated errors of the rigidity measurement were obtained in the final combined $r\phi$-fitting process. Figure 5.12 shows the estimated error of the $1/R_t$ for BESS 93 flight data. The plane histogram is for all the events that passed through the selection and the shadowed histogram is for the case that $N_{r\phi-\mathrm{fit}} > 20$. Both histograms have a clear peak around $\Delta(1/R_t) \sim 0.005$. According to the following relation,

$$\Delta\left(\frac{1}{R_t}\right) = \frac{\Delta(R_t)}{R_t^2} = \frac{\Delta(R_t)}{R_t}\frac{1}{R_t},$$

the $\Delta(1/R_t)$ is decomposed into fractional errors of rigidity ($\Delta(R_t)/R_t$) and inverse rigidity ($1/R_t$). The value of 0.005 thus indicates the particles with the transverse rigidity of up to 200 GV are at least 1σ away from the particles with the opposite charge. It is noted that no event with $\Delta(1/R_t)$ of more than 0.031 – were observed and therefore all events with rigidity below 1 GV are more than 30σ away from the negative rigidity region. Figure 5.13 shows the mean of the $\Delta(1/R_t)$ distribution as a function of the absolute rigidity for the case that $N_{r\phi-\mathrm{fit}} > 20$. Almost constant values are obtained in the entire rigidity range.

The quality of the TOF and β measurement can be checked by utilizing the unbiased trigger CD sample. Figure 5.14 (a) and (b) show β^{-1} versus rigidity plot for the unbiased trigger CD sample of BESS 93 flight data and the Monte Carlo (M.C.) data sample, respectively. The M.C. data are produced by isotropically injecting the protons having the same rigidity spectrum into the simulated BESS detector. Distribution of the particles including albedo are well reproduced in the M.C. data except for the energetic electron, He, and isotopes of proton. It is clear from both figures that the downward moving particles in the positive β^{-1} region are

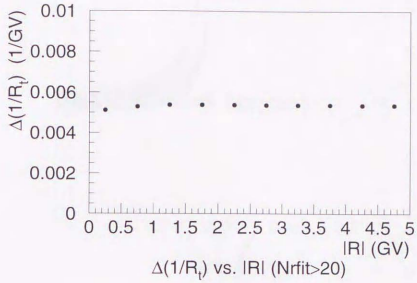

Figure 5.13: $\Delta(1/R_t)$ as a function of the absolute rigidity.

unambiguously separated from the upward moving albedo particles in the negative β^{-1} region. Various particles can be clearly identified up to the rigidity of a few GV.

Two independent measurement errors contribute to the resolution of β^{-1} as follows:

$$\frac{\Delta\beta^{-1}}{\beta^{-1}} = \frac{\Delta t}{t} + \frac{\Delta \ell_{\mathrm{path}}}{\ell_{\mathrm{path}}},$$

where t is the measured TOF and ℓ_{path} is the path-length of the particle between the top and the bottom TOF counter. Figure 5.15 shows fractional $1/\beta$ resolution as a function of β for the unbiased data and the M.C. data. The open boxes in the figure are for the real data and the black dots are for the M.C. data. Both exhibit a reasonable agreement with the expected value shown as a solid curve, which is calculated based on the following assumptions.

- $\Delta t/t$ is inversely proportional to the number of detected photo-electrons in the scintillation paddle (dashed curve).
- $\Delta\ell_{\mathrm{path}}/\ell_{\mathrm{path}}$ is almost constant over the entire energy range (dotted curve).

Figure 5.16 and 5.17 show β^{-1} versus rigidity plot for the unbiased trigger CD sample of BESS 94 and 95 flight data, respectively. Apparently, band widths in Figure 5.17 are narrower than Figure 5.16 due to the improvement of the TOF counter.

With regard to the dE/dX measurement, Figure 5.18 to 5.20 show the dE/dX measured by the TOF scintillators for the unbiased trigger CD samples of BESS 93, 94, and 95 flight data. We can clearly observe the clear bands of protons, muons/pions/electrons deuterons, ^{3}He, and ^{4}He in both top and bottom counter,

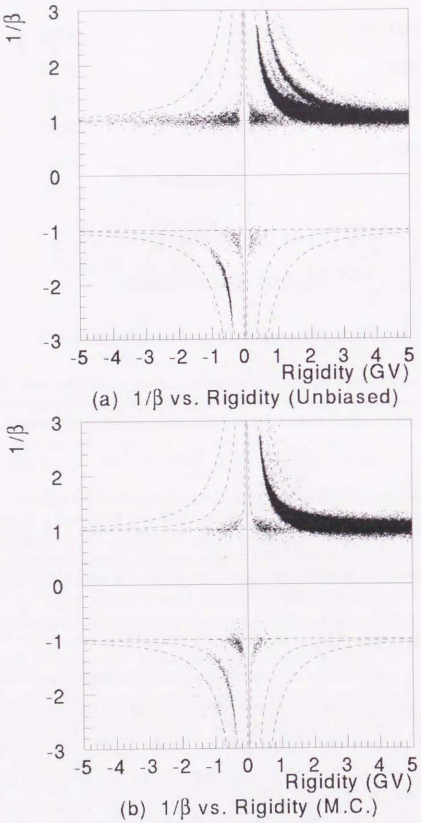

Figure 5.14: $1/\beta$ vs. rigidity of (a) unbiased data sample and (b) M.C. data sample ('93).

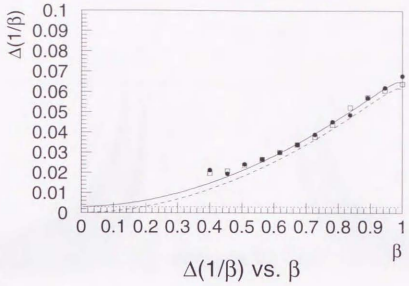

Figure 5.15: Fractional $1/\beta$ resolution vs. *beta*.

i.e. (a) and (b) in the figures. It is noted that the top and the bottom scintillators show different dE/dX behavior in the low rigidity region, where the energy loss in the detector becomes significant.

5.6 Albedo Rejection

In search for antihelium, we have to carefully reject albedo particles since upward moving positive particles have the same event configuration as downward moving negative particles except for the sign of the velocity. The TOF system can clearly separate upward moving and downward moving particles using the sign of the particle-velocity as shown in Fig. 5.14, 5.16, and 5.17 of section 5.5. We reject all upward moving albedo particles at this stage, and limit further analysis to the downward moving particles.

5.7 Selection by β

The velocity β of the observed particles can be calculated from the mass m, charge e, and rigidity R as

$$\frac{1}{\beta^2} = \left(\frac{m}{e}\right)^2 \frac{1}{R^2} + 1.$$

Then we have a band structure in a plot for $1/\beta$ vs. rigidity according to the value of (m/e) as shown in Figure 5.21 to 5.23 for three flight data. Only the positive velocity regions are shown in these figures. The bands in the figures correspond

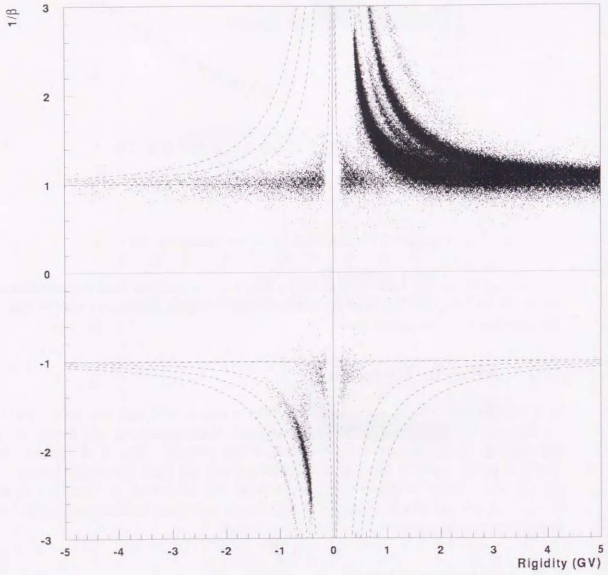

Figure 5.16: $1/\beta$ vs. rigidity of unbiased data sample ('94).

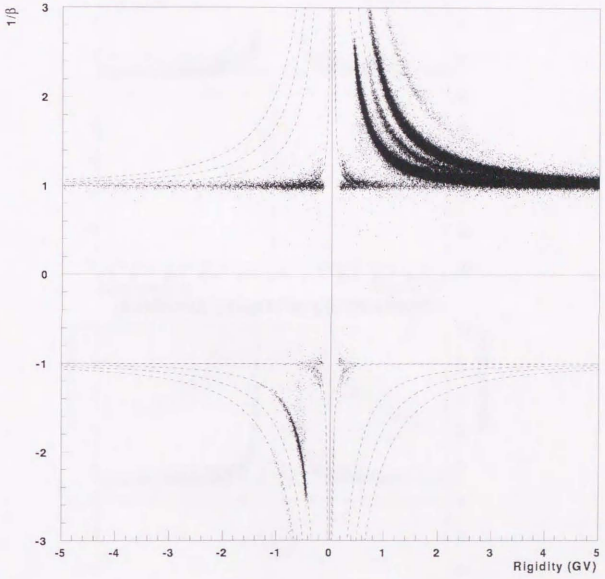

Figure 5.17: $1/\beta$ vs. rigidity of unbiased data sample ('95).

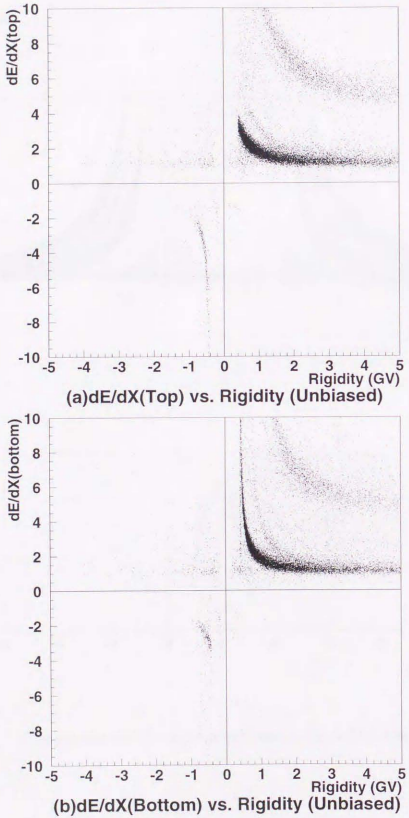

Figure 5.18: $\mathrm{d}E/\mathrm{d}X$ vs. rigidity of unbiased data sample ('93)

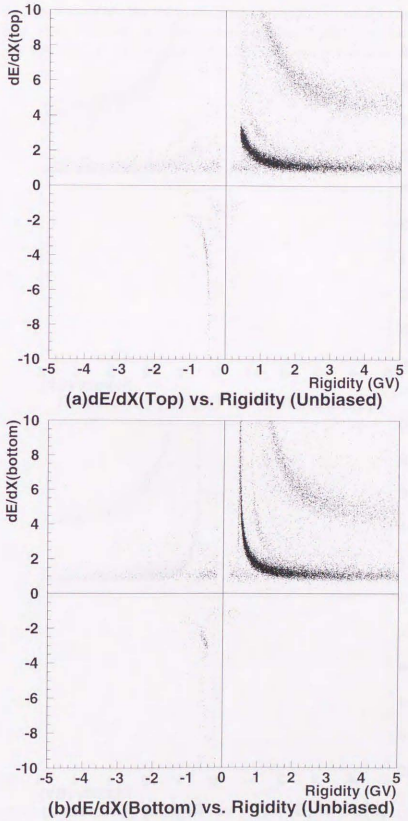

Figure 5.19: $\mathrm{d}E/\mathrm{d}X$ rigidity of unbiased data sample ('94)

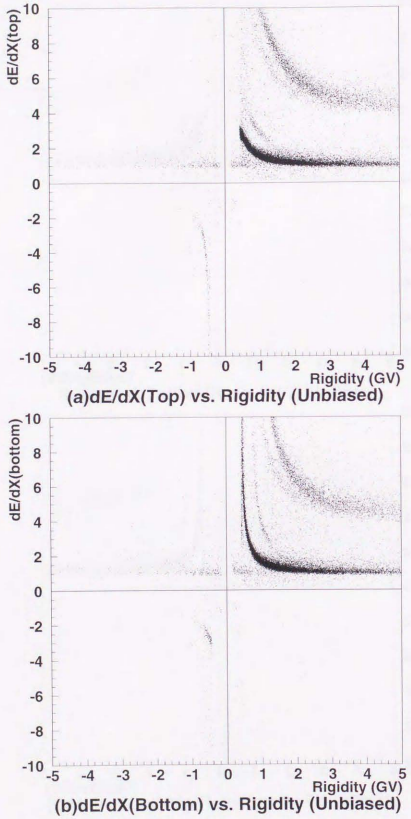

Figure 5.20: $\mathrm{d}E/\mathrm{d}X$ vs. rigidity of unbiased data sample ('95)

in the down-to-up order to electron, muon/pion, proton, ^{3}He, deuteron/^{4}He, and tritium. Theoretical values for these species are denoted in dashed lines in the plot. It is manifest that deuteron and ^{4}He are duplicated in the same band. To extract ^{4}He and ^{3}He samples, a cut indicated by the solid lines is applied.

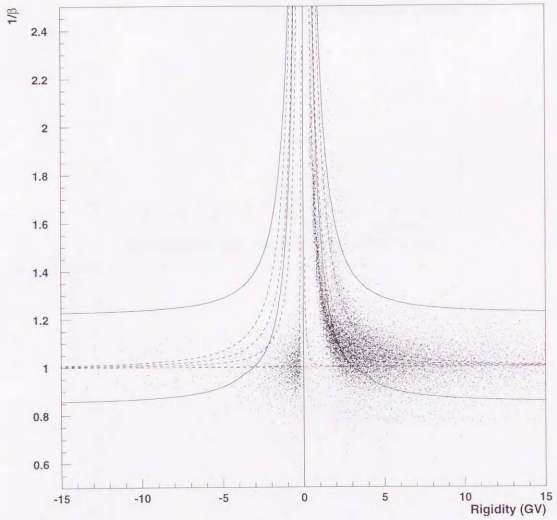

Figure 5.21: β^- vs. rigidity ('93).

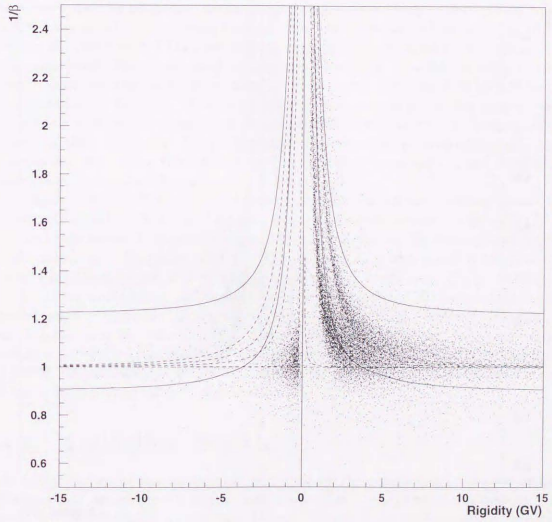

Figure 5.22: β^- vs. rigidity ('94).

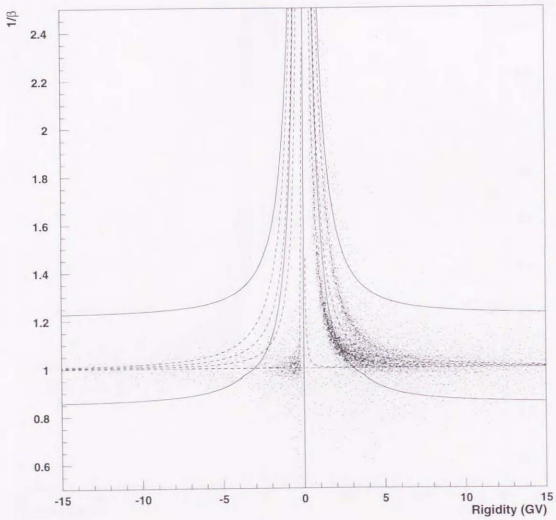

Figure 5.23: β^- vs. rigidity ('95).

5.8 Selection by dE/dX

We utilize a band structure of dE/dX to extract only heliums and antiheliums among all particle species which are observed. Figure 5.24 to 5.29 show dE/dX-versus-rigidity plots of '93, '94, and '95 flight data for the top and bottom scintillators, where events are already selected by the β cut. Because dE/dX is proportional to the square of the charge of an incident particle, we have two main bands in the plots. Lower one is for particles with charge = 1 and upper one is for particles with charge = 2. Theoretical values for muon/electron, proton, and helium are indicated in dashed lines in all plots. In the lower band, narrow part in the rigidity below 1 GV corresponds to deuterons that survived the β cut as well as heliums. In the region of rigidity over 1 GV, protons/muons/positrons/deuterons are duplicated in the same band. The upper band corresponds to heliums. In order to extract rather pure helium samples, we have two solid cut lines as shown in figur 5.24 to 5.26 for the top scintillator. We select the events inside of these two curves, which means events of particle with exactly charge = 2. For the bottom scintillator we have one solid cut line in a plot. We select the events greater than this line to keep higher efficiency than band cut. After this dE/dX cut, we obtained pure helium and antihelium samples with keeping high selection efficiency.

Figure 5.30 to 5.32 show β^--versus-rigidity plots for the samples that passed the preselection and dE/dX cut. ^{3}He and ^{4}He are separated below rigidity of 3 GV as shown in the figure. Compared to figure 5.21 to 5.23, most of the muons/pions/electrons and protons are eliminated after the dE/dX cut. It is also noted that off-timing events scattered in the $\beta^{-1} < 1$ region are clearly swept out. Those events are with having multi-tracks or interactions in the instrument. Although they cannot be removed even by the preselection, they exhibit improper dE/dX behaviors in scintillators and can be rejected by the dE/dX cut. Moreover, the β cut rejects electron and muon/pion events in the rigidity region below 3 GV, which passed the dE/dX cut accidentally, due to interactions in the scintillators or the well known Landau tail effect of dE/dX distribution.

5.9 Antihelium Search

All selections up to this level do not discriminate the positive and negative rigidity (helium and antihelium). Figure 5.33 shows the 1/rigidity distribution with all selections but the track quality cut. Those events that are in the region of negative rigidity are apparently spilling over from the high energy region of positive rigidity due to the finite chamber resolution. Figure 5.34 shows the 1/rigidity distribution after all cuts. In this figure, because of the strict track quality cut criteria, the spillover from the high energy region is suppressed. This spillover can be suppressed more if stricter track quality cuts are applied, however such cuts sacrifice the high selection efficiency. The applied preselection was determined by a trade-off of the suppression of spillover and the high selection efficiency.

The resultant edge of the spillover in the negative rigidity region in Figure 5.34

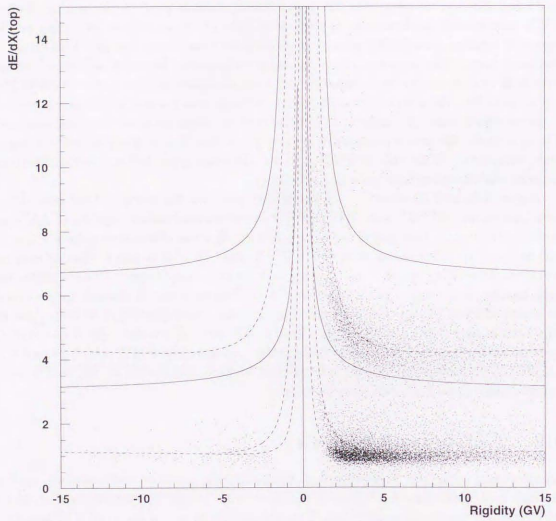

Figure 5.24: $\mathrm{d}E/\mathrm{d}X(\mathrm{top})$ vs. rigidity after β cut ('93).

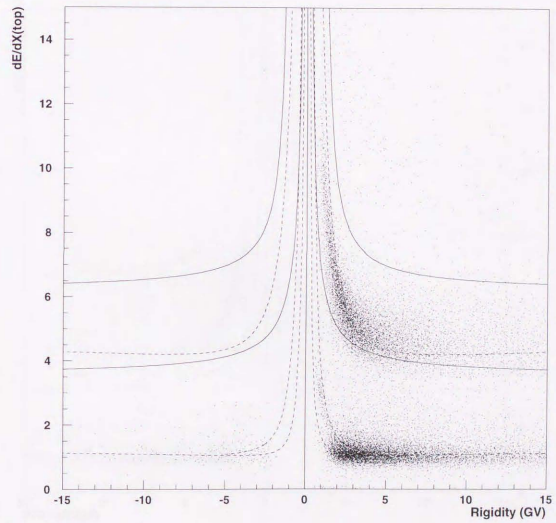

Figure 5.25: $\mathrm{d}E/\mathrm{d}X(\mathrm{top})$ vs. rigidity after β cut ('94).

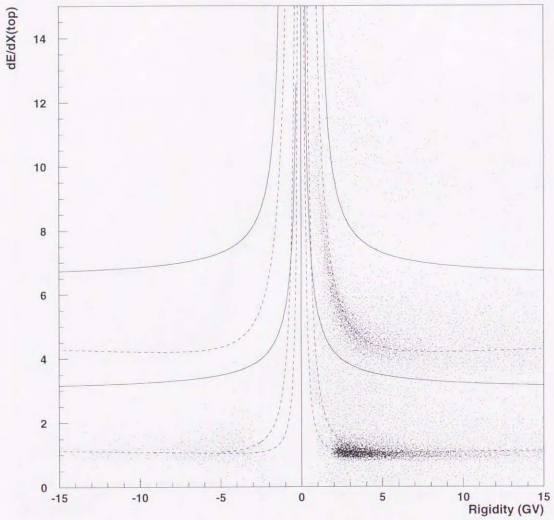

Figure 5.26: $\mathrm{d}E/\mathrm{d}X$(top) vs. rigidity after β cut ('95).

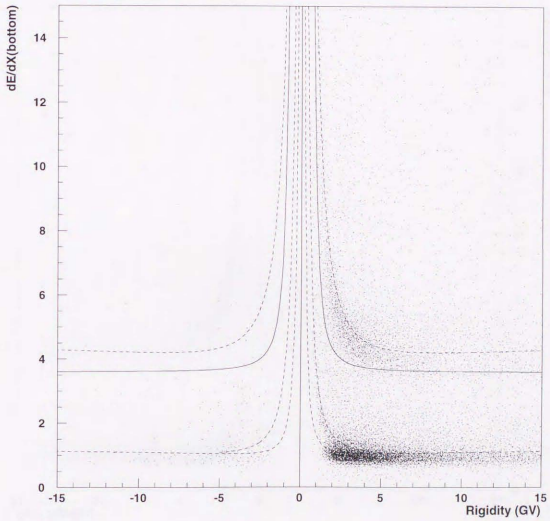

Figure 5.27: $\mathrm{d}E/\mathrm{d}X$(bottom) vs. rigidity after β cut ('93).

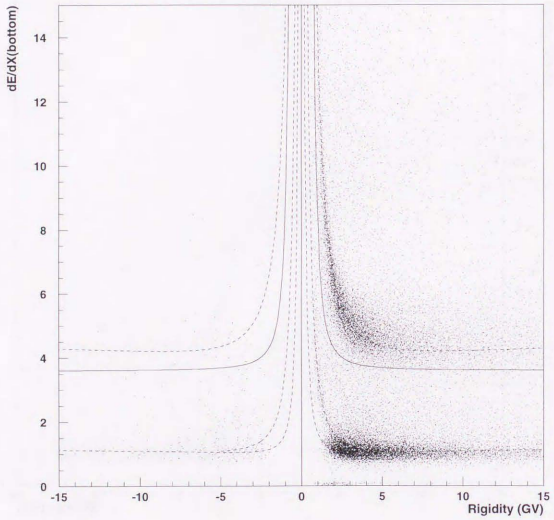

Figure 5.28: $\mathrm{d}E/\mathrm{d}X$(bottom) vs. rigidity after β cut ('94).

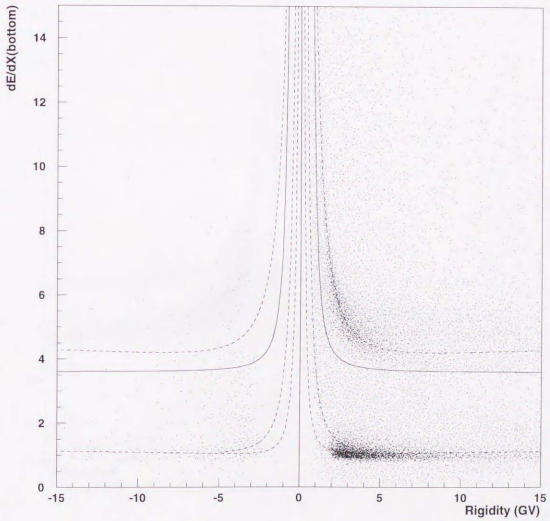

Figure 5.29: $\mathrm{d}E/\mathrm{d}X$(bottom) vs. rigidity after β cut ('95).

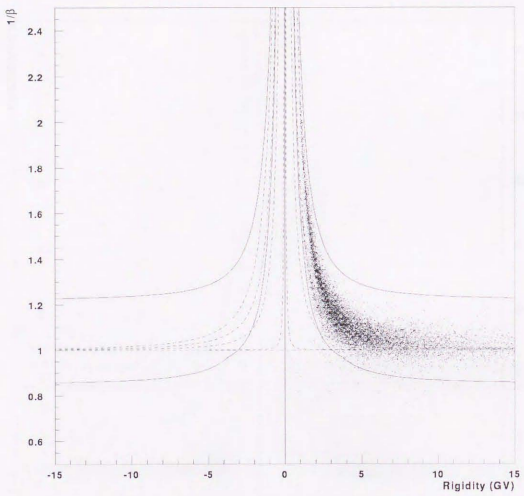

Figure 5.30: $1/\beta$ vs. rigidity after $\mathrm{d}E/\mathrm{d}X$ cut ('93).

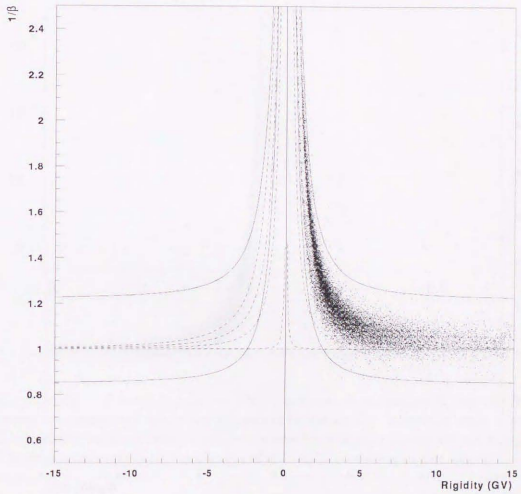

Figure 5.31: $1/\beta$ vs. rigidity after $\mathrm{d}E/\mathrm{d}X$ cut ('94).

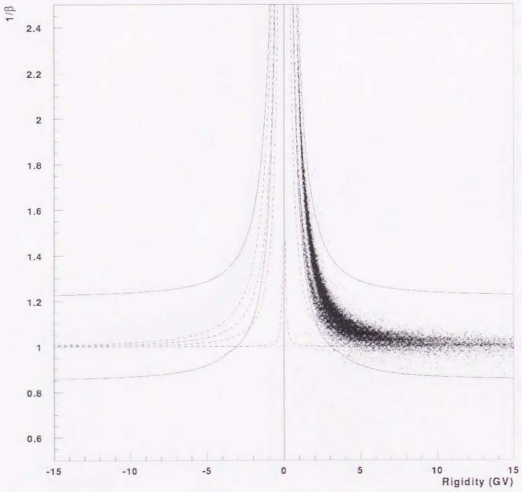

Figure 5.32: $1/\beta$ vs. rigidity after $\mathrm{d}E/\mathrm{d}X$ cut ('95).

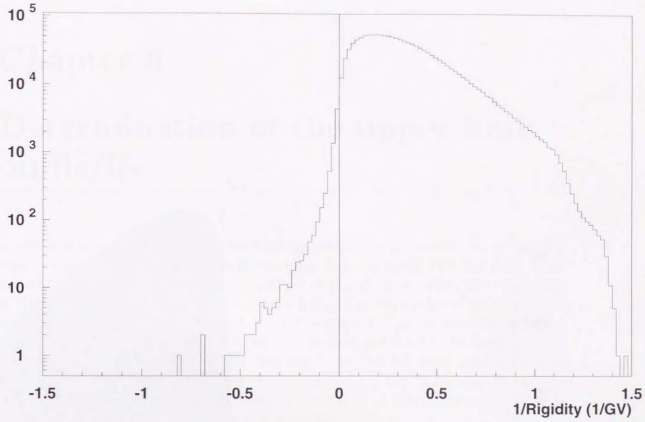

Figure 5.33: 1/rigidity distribution without track quality cut ('93+'94+'95).

corresponds to the rigidity of -16 GV. Therefore, it is concluded that we have no antihelium candidate in the rigidity region below 16 GV. The other edge in the positive rigidity region is determined by the events that stop in the bottom scintillator. The edge corresponds to the rigidity of 0.71 GV, as shown in the figure.

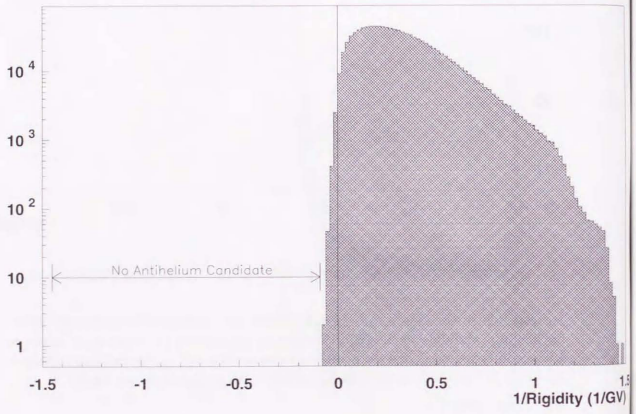

Figure 5.34: 1/rigidity distribution ('93+'94+'95).

Chapter 6

Determination of the upper limit on $\overline{\mathrm{He}}/\mathrm{He}$

In the previous chapter, it is shown that no antihelium is detected in the rigidity region below 16 GV. From this result, the upper limit on the $\overline{\mathrm{He}}/\mathrm{He}$ flux ratio at the top of the atmosphere (TOA) is determined in this chapter. First, the efficiencies of the TT trigger selection are estimated in § 6.1. The efficiencies of the off-line cut selections are approximated in § 6.2. Then the number of the observed heliums are counted in § 6.3. Section 6.4 presents a correction method for the energy loss of particles in the atmosphere and the instrument. Section 6.5 describes a method to estimate the surviving probabilities of heliums and antiheliums in the atmosphere and the instrument. In § 6.6 the upper limit on the $\overline{\mathrm{He}}/\mathrm{He}$ flux ratio at the TOA is calculated using parameters obtained in the above sections.

6.1 Track Trigger Efficiency

Before determining the trigger efficiency and then the upper limit, let us review the trigger selections described in the previous chapters briefly. There were three stages in the trigger selection. The first stage was the T0 trigger which is generated by the coincidence of the top and bottom layers of TOF scintillators. The second stage was the hit-pattern selection in the TT to reject multi- or null-hit-pattern which is inconsistent with the single track. The third stage was the track-rigidity selection in the TT to reject most of positively curved events using IDC and ODC hit-patterns. The events that passed through above three stages of selections were recorded and undergone the further off-line analysis.

If we utilize the unbiased trigger T0 high CD sample, we can obtain T1 trigger pattern and rigidity selection efficiencies for helium events by comparing the numbers of heliums that passed and did not pass the selections. Figure 6.1 shows the efficiency of T1 trigger pattern selection for helium events. In '93 flight the pattern efficiency is less than 25% in the whole energy range. This is because the hit pattern signal from IDCs and ODCs are suffered by cross talk noise. Before '94 flight, this instrumental defect was removed and then the efficiency of pattern selection was modified to

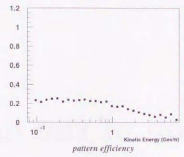

Figure 6.1: Track-pattern selection efficiency ('93).

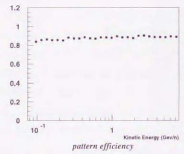

Figure 6.1: Track-pattern selection efficiency ('94).

greater than 85% in both '94 and '95 flights.

The efficiency of the track rigidity selection is estimated by fitting a theoretical efficiency function of track-rigidity selection with helium events in the unbiased trigger T0 high CD sample. Since the real data of helium events reside only in positive rigidity region, we assume that this fitted function is correct even in the negative rigidity region. Figure 6.2 shows the measured efficiency values and fitted efficiency curve of the track-rigidity selection as a function of rigidity^{-1} for the He T1 trigger mode. Boxes are the efficiencies measured using helium events in the unbiased trigger T0 high CD sample. The efficiencies of TT trigger for each flight and for each T1 mode are summarized in Table 6.1. The definition of T1 mode in the table is the same as in Table 2.8, 2.9, and 2.10. The T1 modes in which the numbers of events are small and then were not utilized for the calculation of the upper limit are omitted in the table. $\epsilon_{\text{pattern}}$ is the efficiency of the TT pattern selection for He and $\overline{\epsilon}_{\text{rigidity}}$ is the efficiency of the TT rigidity selection for $\overline{\text{He}}$ in the table. $\overline{\epsilon}_{\text{rigidity}}$ is obtained assuming that the spectrum shape of $\overline{\text{He}}$ is the same as He.

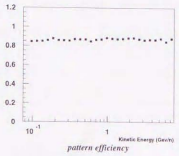

Figure 6.1: Track-pattern selection efficiency ('95).

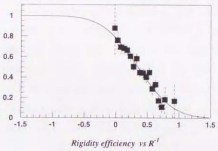

Figure 6.2: Track-rigidity selection efficiency ('93).

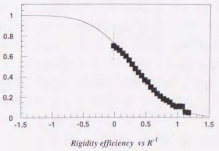

Figure 6.2: Track-rigidity selection efficiency ('94).

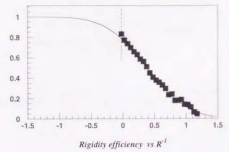

Figure 6.2: Track-rigidity selection efficiency ('95).

Table 6.1: Summary of TT trigger efficiency

flight year	T1 mode	$\epsilon_{\mathrm{pattern}}$	$\bar{\epsilon}_{\mathrm{rigidity}}$
'93	$\overline{He}$	0.13	0.91
	Multi	0.05	0.74
'94 first half	$\overline{He}$	0.86	0.89
'94 last half	$\overline{He}$	0.88	0.88
'95	$\overline{He}$	0.87	0.94

Table 6.2: Summary of the off-line cut efficiencies

flight year	loose He	TRQ cut (ϵ)	TOF cut (ϵ)	BET cut (ϵ)	DEX cut (ϵ)	ϵ_{cuts}
'93	45,338	36,346(0.80)	31,309(0.86)	31,146(0.99)	28,547(0.92)	0.63
'94 first half	44,571	38,186(0.86)	34,295(0.90)	33,515(0.98)	30,763(0.92)	0.69
'94 last half	27,020	23,263(0.86)	20,649(0.89)	20,472(0.99)	18,955(0.93)	0.70
'95	65,373	54,070(0.83)	51,559(0.95)	51,467(1.00)	50,868(0.99)	0.78

6.2 Off-line cut Efficiencies:

The absolute values of the off-line cut efficiencies will not be used in the calculation of upper limits on the $\overline{\mathrm{He}}$/He flux ratio, which will be mentioned in detail later in section 6.6. Thus the values will not affect the result, i.e., the upper limit. But knowing the efficiencies of each off-line cut for each part of flight is very important, because these will show how the cuts were performed and what is the main background for the search.

For this purpose, we first attempted to obtain the efficiencies of the off-line cuts through Monte Carlo simulations, using the GEANT codes. However, we found that the GEANT codes are not describing hadronic interactions for helium and antihelium. Even after exhaustive reading of codes for some months and attempts of adding hadronic interactions of helium and antihelium to them, we could not resolve it. At last we gave up to utilize the GEANT codes and the estimates of efficiencies by Monte Carlo simulations. But we still attempted to somehow approximate the efficiencies of the off-line cuts, where even only the trends might be viewed. Therefore, we defined the starting sample which contains almost all helium events and from which all cuts are applied. The starting sample events were defined as events which survived the TT pattern selection, single track, loose β, and loose $\mathrm{d}E/\mathrm{d}X$ cuts in the unbiased trigger T0 high CD sample.

Figure 6.3, 6.4, and 6.5 show β-versus-rigidity, $\mathrm{d}E/\mathrm{d}X$(top)-versus-rigidity, and $\mathrm{d}E/\mathrm{d}X$(bottom)-versus-rigidity plots, respectively, before the loose β and loose $\mathrm{d}E/\mathrm{d}X$ cuts for a part of the '94 flight data. Figure 6.6, 6.7, and 6.8 show β vs. rigidity, $\mathrm{d}E/\mathrm{d}X$(top) vs. rigidity, and $\mathrm{d}E/\mathrm{d}X$(bottom) vs. rigidity plots, respectively, after the loose β and loose $\mathrm{d}E/\mathrm{d}X$ cuts for a part of the '94 flight data, i.e., plots for the starting sample of the '94 flight data. In these figures, loose cuts are denoted as solid curves and the off-line cuts used in the search are denoted as dashed curves. Then we can obtain estimated values for the cut efficiencies, applying all cuts to this starting sample, where all the events in the negative rigidity region are rejected by these cuts.

The starting sample method was checked using proton events by comparing results from a proton starting sample and results from Monte Carlo simulations using the GEANT codes. This check showed that two different estimates of cut efficiencies are very similar.

Table 6.2 summarizes the estimates of off-line cut efficiencies by the helium starting sample. In the table, "loose He", "TRK cut", "TOF cut", "BET cut", and "DEX cut" denote the starting sample, the track quality cut, the TOF quality cut, the β cut, and the $\mathrm{d}E/\mathrm{d}X$ cut, respectively. The numbers in the table are the numbers of helium events which survived the according off-line cuts shown in the first line. The numbers in parentheses are the off-line cut efficiencies by this starting sample method, where the sequence of applying the cuts are as the left-to-right order of cuts in the table, and the last column, ϵ_{cuts} denotes the total efficiency of the off-line cuts.

From the table it is seen that the $\mathrm{d}E/\mathrm{d}X$ cut for '95 flight data is very efficient as 99 % due to the improvement of the TOF hodoscope time resolution. On the other hand, the $\mathrm{d}E/\mathrm{d}X$ cuts for '93 and '94 flight data are not so efficient, where the efficiency is about 92 % to 93 %. Figure 6.9 and 6.10 show $\mathrm{d}E/\mathrm{d}X$(top)-versus-rigidity and $\mathrm{d}E/\mathrm{d}X$(bottom)-versus-rigidity plots, respectively, for all the '94 flight data with the cuts for the search, except that the $\mathrm{d}E/\mathrm{d}X$ cuts are loosened to the loose $\mathrm{d}E/\mathrm{d}X$ cuts. The meaning of the solid and dashed curves in these figures are the same as Figure 6.7 and 6.8. Then, from these figures, it is seen that the $\mathrm{d}E/\mathrm{d}X$ cuts are set rather tight for the purpose to reject the negative electron/muon/pion background events, which are in the region of -1 to -10 GV. These background events will be furthermore checked in section 7.5 of Chapter 7. The track quality cuts were determined by a trade-off of the suppression of spillover events, which are from the high energy region of the positive rigidity, and the high selection efficiencies, which are 80 %, 86 %, and 83 % for '93, '94, and '95 flight data, respectively, from the table. Figure 6.11 to 6.13 show all these efficiencies as functions of the kinetic energy per nucleon. As shown in the table 6.2 and the figure 6.11 to 6.13, pure helium sample is selected with high efficiencies of about 63 % to 78 % for three flight data.

6.3 Number of Observed Heliums

In the off-line analysis, we applied the selection for the good single track and subsequently the track quality cut and the cut for the good timing measurement. Finally to extract helium and antihelium signals, the β and $\mathrm{d}E/\mathrm{d}X$ cut were applied.

We define here temporarily the "total number of observed heliums" ($\mathrm{N_{helium}}$) as the number of the heliums that passed through the TT pattern selection and would have survived all off-line selections, if they were not rejected by the track-rigidity selection. Simply, $\mathrm{N_{helium}}$ is the number of the helium events that passed through all selections but the TT rigidity selection. The number $\mathrm{N_{helium}}$ is obtained by counting the number of the events in the unbiased trigger T0 high CD sample that survived all of the trigger- and the off-line cut selections except for the track-rigidity selection in the TT, and correcting it by a factor $\mathrm{N_{CD}}$ = 40, 15, 30, and 20 in each part of flights.

If $\epsilon_{\mathrm{pattern}}$ of BESS '93 flight data was not as low as 18 %, the definition of $\mathrm{N_{helium}}$ described above would be satisfactory. However, the low TT pattern efficiency means that such events as did not pass through TT pattern selection are not negligible in

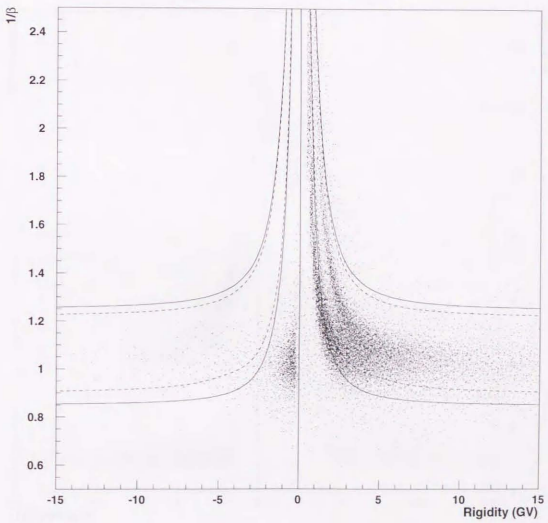

Figure 6.3: Loose β cut ('94).

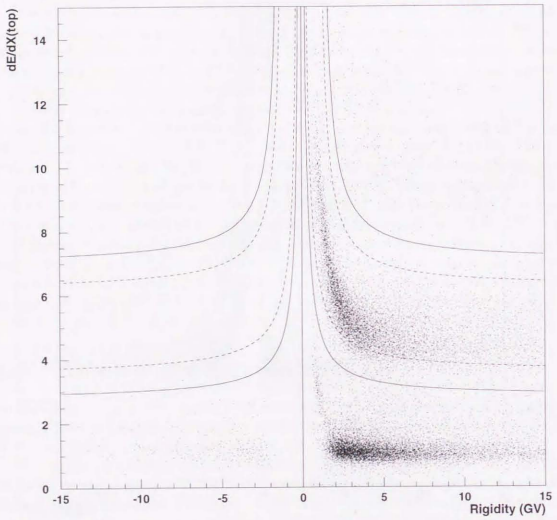

Figure 6.4: Loose $\mathrm{d}E/\mathrm{d}X$ cut for the top scintillator ('94).

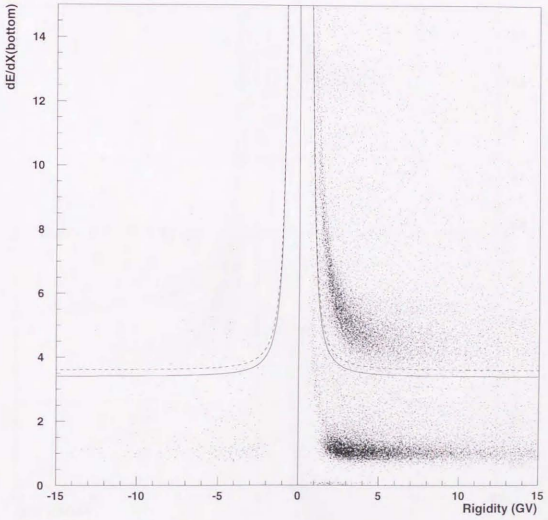

Figure 6.5: Loose $\mathrm{d}E/\mathrm{d}X$ cut for the bottom scintillator ('94).

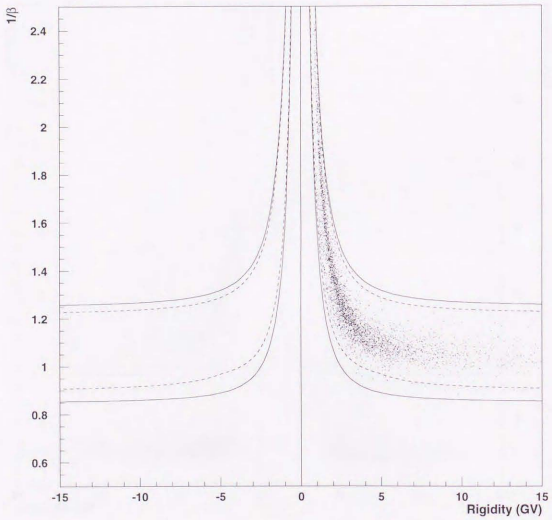

Figure 6.6: β vs. rigidity plot for the starting sample ('94).

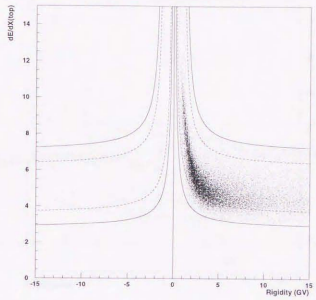

Figure 6.7: $\mathrm{d}E/\mathrm{d}X$(top) vs. rigidity plot for the starting sample ('94).

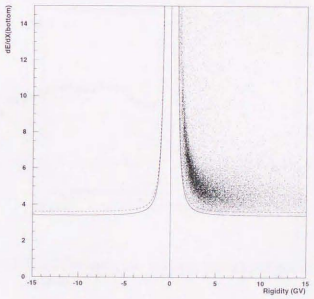

Figure 6.8: $\mathrm{d}E/\mathrm{d}X$(bottom) vs. rigidity plot for the starting sample ('94).

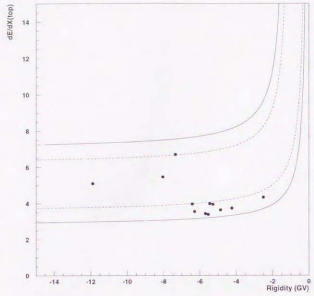

Figure 6.9: $\mathrm{d}E/\mathrm{d}X$(top) vs. rigidity plot with the loose $\mathrm{d}E/\mathrm{d}X$ cut (Rigidity<0, '94).

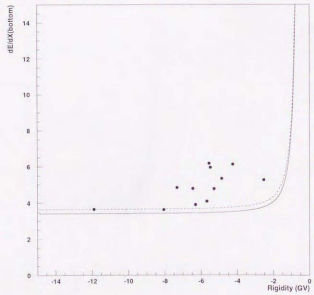

Figure 6.10: $\mathrm{d}E/\mathrm{d}X$(bottom) vs. rigidity plot with the loose $\mathrm{d}E/\mathrm{d}X$ cut (Rigidity<0, '94).

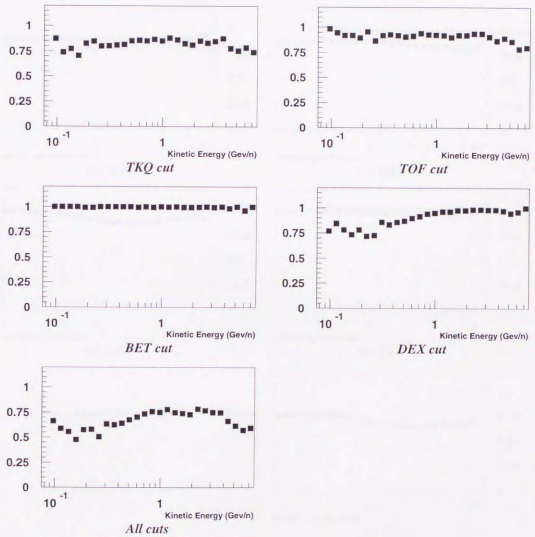

Figure 6.11: Efficiency vs. kinetic energy per nucleon ('93).

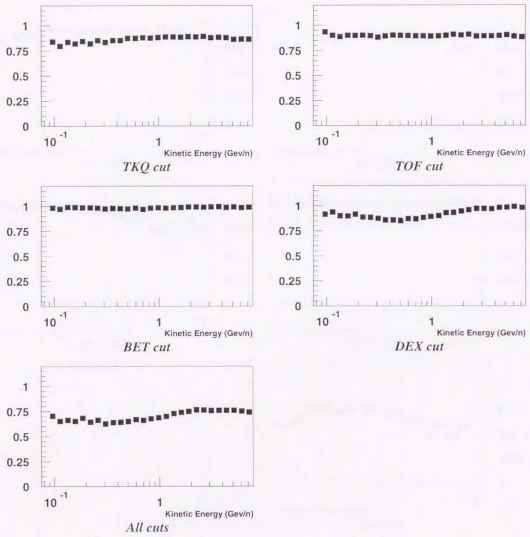

Figure 6.12: Efficiency vs. kinetic energy per nucleon ('94).

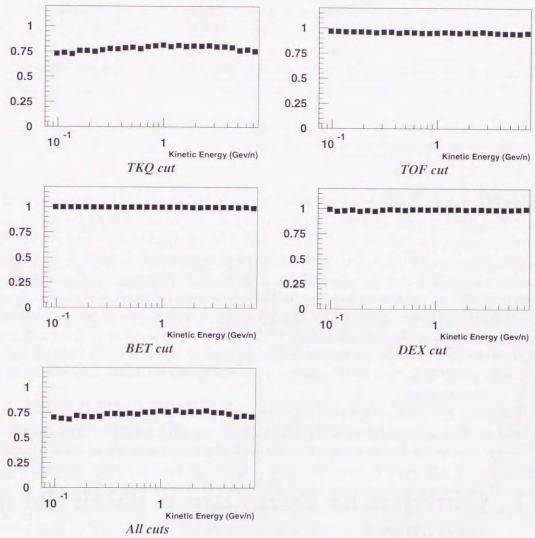

Figure 6.13: Efficiency vs. kinetic energy per nucleon ('95).

Table 6.3: Summary of the number of heliums (0.7 GV < R < 16 GV).

flight year	T1 mode	CD sample	N_{CD}	N_{helium}
'93	$\overline{He}$	3,700	40	148,000
	Multi	1,321	40	52,840
	Not pattern[a]	28,141	–	28,141
'94 first half	$\overline{He}$	25,760	15	386,400
	Not pattern	3,679	–	3,095
'94 last half	$\overline{He}$	15,941	30	478,230
	Not pattern	2,043	–	2,043
'95	$\overline{He}$	42,656	20	853,120
	Not pattern	6,534	–	6,534
Total		129,775	–	1,958,403

[a]Not passed the TT pattern selection

number for BESS '93 flight data, even though these events were not processed by the TT rigidity trigger and then the number can not be corrected by a factor N_{CD}. For this reason, the definition of N_{helium} should be changed to save and utilize these events. Thus we redefine the "total number of observed heliums"(N_{helium}) as the number of the heliums that passed through the TT pattern selection and would have survived all off-line selections, if they were not rejected by the TT rigidity selection, or that were rejected by the TT pattern selection and have survived all off-line selections in the unbiased trigger CD sample. The number of these additional heliums can be obtained by counting the number of the events in the CD sample that were rejected by the track-pattern selection in the TT, and survived all of the off-line cut selections.

Following the redefinition and counting also the additional heliums, the number of heliums N_{helium} is found to be 1,958,403 in the rigidity range between 0.7 and 16 GV. The number of heliums observed for each flight is summarized in Table 6.3.

6.4 Correction for Energy Loss in the air and the instrument

The observed heliums lost their energy while passing through the 5 g/cm^2-thick air and the upper wall of the instrument, where the rigidity is measured in the center of the instrument. We have to correct the measured energy to get the energy at the TOA.

Suppose that the helium or antihelium has a total energy E_0 at the TOA, the energy after passing material with the thickness of x g/cm^2, $E(x)$, is given by the

following equation:

$$E(x) = E_0 - \int_0^x \frac{dE}{dx}(E(x))dx,$$

where $dE/dx(E(x))$ is the energy loss per unit material thickness as a function of the total energy. Differentiation of this equation gives

$$E'(x) = \frac{dE}{dx}(E(x)).$$

By solving this differential equation, the energy after passing through the material thickness can be obtained. The energy before loosing its energy can be also calculated in the same way from the material thickness which are estimated by extrapolating the track into the TOA.

For this calculation, it is assumed that the residential material of the instrument over the jet chamber is equivalent to 7 g/cm^2 aluminum and the thickness of the air is 5 g/cm^2.

By this calculation, the observed lowest rigidity of helium in the instrument, which is 0.71 GV, should be corrected to 1.04 GV at the top of the atmosphere.

6.5 Loss of He and $\overline{\text{He}}$ in the air and the instrument:

Before determining an upper limit on the $\overline{\text{He}}$/He flux ratio at the top of the atmosphere, we must evaluate the loss of He and $\overline{\text{He}}$ in the air and the instrument. For this purpose we need to know the inelastic cross sections of He and $\overline{\text{He}}$ to the air and the instrument. To simplify this evaluation, we assume followings,

- The air is equivalent to a material whose atomic weight A is 14.61 in amu and the thickness of material is 5 g/cm^2.
- The instrument is equivalent to the aluminum whose thickness is 15 g/cm^2.

Then what is necessary for the evaluation is simplified to the inelastic cross sections of He and $\overline{\text{He}}$ to a material with atomic weight A. However, these are not measured experimentally over wide energy range. Thus we started from the inelastic cross sections of p and $\overline{p}$ to nucleus, because these are measured in rather wide energy range. Then we calculated the cross sections of He and $\overline{\text{He}}$ using the model of hard spheres with overlap, which will be mentioned later in detail.

For p to nucleus, from a series of experiments a well known phenomenological formula is given as follows [34]:

$$\sigma = 45A^{0.7}[1 - 0.62e^{-E/200}sin(10.9E^{-0.28})][1 + 0.0016sin(5.32 - 2.63lnA)] \quad (6.1)$$

where E is the kinetic energy of proton in MeV, A is the atomic weight of the nucleus in amu, and σ is the cross section in mb.

Figure 6.14 shows the experimental points of the inelastic cross section of $\overline{p}$ to aluminum and carbon [35, 36, 37, 38, 39, 40, 41]. These experimental points are

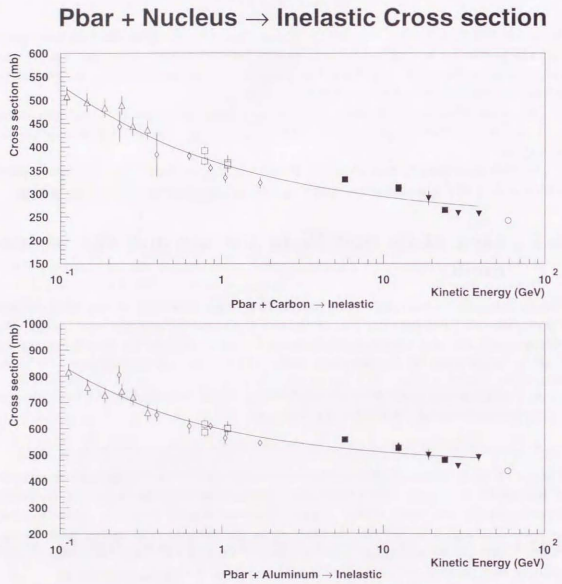

Figure 6.14: Inelastic cross section of $\overline{p}$ to nucleus.

fitted by the function of $a + b\,e^{cx}$, where a, b, and c are parameters to be fitted, and x is the kinetic energy of $\overline{p}$ in GeV. The resultant functions are shown in the figure as solid curves. To obtain the cross section of $\overline{p}$ to air, we used the cross section of $\overline{p}$ to carbon and utilized the $A_t^{2/3}$ dependence, where A_t is the atomic weight of the target nucleus. Then we can calculate $\sigma(\overline{p}, \text{air})$ as follows.

$$\sigma(\overline{p}, \text{air}) = \sigma(\overline{p}, \text{carbon}) \times (14.61^{2/3}/12.00^{2/3}) \tag{6.2}$$

Next, we evaluated the cross sections of He and $\overline{\text{He}}$ to nucleus adopting the model of hard spheres with overlap [42, 43]. This model is derived from simple geometrical consideration and expressed as follows [67, 68].

$$\sigma(A_i, A_t) \propto (A_i^{1/3} + A_t^{1/3} - 0.71 \times (A_i^{-1/3} + A_t^{-1/3}))^2 \tag{6.3}$$

where $\sigma(A_i, A_t)$ is the cross section of an incident particle with atomic weight A_i to a target with atomic weight A_t. Using formula 6.3, all necessary cross sections are obtained as follows.

$$\sigma(\text{He}, \text{air}) = \sigma(p, \text{air}) \times \frac{(4.00^{1/3} + 14.61^{1/3} - 0.71 \times (4.00^{-1/3} + 14.61^{-1/3}))^2}{(1.01^{1/3} + 14.61^{1/3} - 0.71 \times (1.01^{-1/3} + 14.61^{-1/3}))^2} \tag{6.4}$$

$$\sigma(\text{He}, \text{Al}) = \sigma(p, \text{Al}) \times \frac{(4.00^{1/3} + 26.98^{1/3} - 0.71 \times (4.00^{-1/3} + 26.98^{-1/3}))^2}{(1.01^{1/3} + 26.98^{1/3} - 0.71 \times (1.01^{-1/3} + 26.98^{-1/3}))^2} \tag{6.5}$$

$$\sigma(\overline{\text{He}}, \text{air}) = \sigma(\overline{p}, \text{air}) \times \frac{(4.00^{1/3} + 14.61^{1/3} - 0.71 \times (4.00^{-1/3} + 14.61^{-1/3}))^2}{(1.01^{1/3} + 14.61^{1/3} - 0.71 \times (1.01^{-1/3} + 14.61^{-1/3}))^2} \tag{6.6}$$

$$\sigma(\overline{\text{He}}, \text{Al}) = \sigma(\overline{p}, \text{Al}) \times \frac{(4.00^{1/3} + 26.98^{1/3} - 0.71 \times (4.00^{-1/3} + 26.98^{-1/3}))^2}{(1.01^{1/3} + 26.98^{1/3} - 0.71 \times (1.01^{-1/3} + 26.98^{-1/3}))^2} \tag{6.7}$$

Figure 6.15 (1-a) and (1-b) show the resultant inelastic cross sections of He and $\overline{\text{He}}$ to the aluminum and the air, i.e. $\sigma(\text{Al})$, $\overline{\sigma}(\text{Al})$, $\sigma(\text{air})$, and $\overline{\sigma}(\text{air})$, in the unit of $(\text{g/cm}^2)^{-1}$.

When a cross section σ in $(\text{g/cm}^2)^{-1}$ is known, we can calculate the number of surviving particles though a target of thickness d as follows.

$$\text{N}_{\text{survive}} = \text{N}_0 \times e^{-\sigma d} \tag{6.8}$$

where N_0 is the initial number of incident particles. Then η_{air}, $\overline{\eta}_{\text{air}}$, η_{ins}, and $\overline{\eta}_{\text{ins}}$ which are the surviving probabilities of He and $\overline{\text{He}}$ in the air and in the instrument, respectively, are defined as followings.

$$\eta_{\text{ins}} = e^{-(\sigma(\text{Al}) \times 15\,\text{g/cm}^2)}$$
$$\overline{\eta}_{\text{ins}} = e^{-(\overline{\sigma}(\text{Al}) \times 15\,\text{g/cm}^2)}$$
$$\eta_{\text{air}} = e^{-(\sigma(\text{air}) \times 5\,\text{g/cm}^2)}$$
$$\overline{\eta}_{\text{air}} = e^{-(\overline{\sigma}(\text{air}) \times 5\,\text{g/cm}^2)}$$

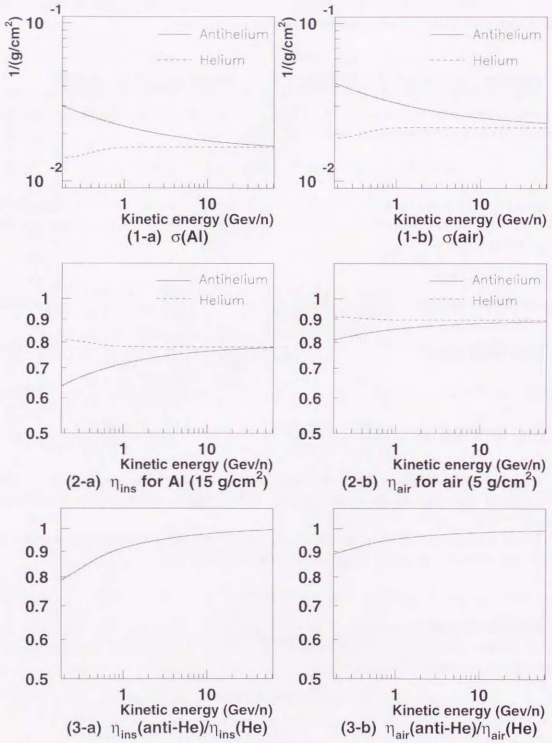

Figure 6.15: Inelastic cross sections of He and $\overline{\mathrm{He}}$ (1-a) to the aluminum (σ(Al), $\overline{\sigma}$(Al)) and (1-b) to the air (σ(air), $\overline{\sigma}$(air)), and surviving probabilities of He and $\overline{\mathrm{He}}$ (2-a) (η_{ins}, $\overline{\eta}_{\mathrm{ins}}$) in 15 g/cm^2 aluminum and (2-b) (η_{air}, $\overline{\eta}_{\mathrm{air}}$) in 5 g/cm^2 air, and probability ratios (3-a) ($\overline{\eta}_{\mathrm{ins}}/\eta_{\mathrm{ins}}$) in 15 g/cm^2 aluminum and (3-b) ($\overline{\eta}_{\mathrm{ins}}/\eta_{\mathrm{ins}}$) in 5 g/cm^2 air.

Figure 6.15 (2-a) and (2-b) show η_{ins} and $\overline{\eta}_{\mathrm{ins}}$, and η_{air} and $\overline{\eta}_{\mathrm{air}}$ as functions of the kinetic energy per nucleon. Then convenient expressions $\eta_{\mathrm{air+ins}}$ and $\overline{\eta}_{\mathrm{air+ins}}$ are defined as follows.

$$\eta_{\mathrm{air+ins}} = \eta_{\mathrm{air}} \times \eta_{\mathrm{ins}}$$
$$\overline{\eta}_{\mathrm{air+ins}} = \overline{\eta}_{\mathrm{air}} \times \overline{\eta}_{\mathrm{ins}}$$

Figure 6.15 (3-a) and (3-b) show $\overline{\eta}_{\mathrm{ins}}/\eta_{\mathrm{ins}}$ and $\overline{\eta}_{\mathrm{air}}/\eta_{\mathrm{air}}$ as functions of the kinetic energy per nucleon. The ratio $\overline{\eta}_{\mathrm{air+ins}}/\eta_{\mathrm{air+ins}} = (\overline{\eta}_{\mathrm{air}}/\eta_{\mathrm{air}}) \times (\overline{\eta}_{\mathrm{ins}}/\eta_{\mathrm{ins}})$ will be used in the calculation of the upper limit on the $\overline{\mathrm{He}}$/He flux ratio in the last section of this chapter.

In order to simplify the calculation of the upper limit, we need another assumption as follows.

- If an inelastic reaction occurred for an incident particle in the air or the instrument, it can not survive the single track, track quality, and TOF quality cuts.

Hereafter, we do not consider heliums and antiheliums that were in inelastic reactions in the calculation of the upper limit.

6.6 Determination of upper limit on $\overline{\mathrm{He}}$/He:

In the previous section we have defined the surviving probabilities of He and $\overline{\mathrm{He}}$ in the air and in the instrument. Now we are ready to calculate the upper limit on the $\overline{\mathrm{He}}$/He flux ratio at the top of the atmosphere. Firstly we determine some conventions as follows.

f_{ta} = The flux of He at the top of the atmosphere.
$\overline{f}_{\mathrm{ta}}$ = The flux of $\overline{\mathrm{He}}$ at the top of the atmosphere.
f_{ob} = The observed flux of He that passed all selections.
$\overline{f}_{\mathrm{ob}}$ = The observed flux of $\overline{\mathrm{He}}$ that passed all selections.
f_{CD} = The flux of He in the unbiased trigger T0 high CD sample that passed all selections but the track trigger rigidity selection.
ϵ = The total efficiency for He.
$\overline{\epsilon}$ = The total efficiency for $\overline{\mathrm{He}}$.
The total efficiencies ϵ and $\overline{\epsilon}$ are expressed as follows.

$$\epsilon = \epsilon_{\mathrm{cuts}} \times \epsilon_{\mathrm{rigidity}} \times \epsilon_{\mathrm{pattern}} \tag{6.9}$$
$$\overline{\epsilon} = \overline{\epsilon}_{\mathrm{cuts}} \times \overline{\epsilon}_{\mathrm{rigidity}} \times \overline{\epsilon}_{\mathrm{pattern}} \tag{6.10}$$

where ϵ_{cuts} and $\overline{\epsilon}_{\mathrm{cuts}}$ are the total off-line cut efficiencies of He and $\overline{\mathrm{He}}$. Then we have following relations between these values.

$$f_{\mathrm{ob}} = \epsilon\, \eta_{\mathrm{air+ins}}\, f_{\mathrm{ta}} \tag{6.11}$$
$$\overline{f}_{\mathrm{ob}} = \overline{\epsilon}\, \overline{\eta}_{\mathrm{air+ins}}\, \overline{f}_{\mathrm{ta}} \tag{6.12}$$

As done at the last of section 6.1, we assume again that $\overline{f}_{\mathrm{ta}}$ has the same energy spectrum as f_{ta}. Therefore these two spectrum are related by one constant k, which is the flux ratio, as follows.

$$\overline{f}_{\mathrm{ta}} = k\, f_{\mathrm{ta}} \tag{6.13}$$

Using this k, $\overline{f}_{\mathrm{ob}}$ is also related to ϵ, $\overline{\epsilon}$, $\eta_{\mathrm{air+ins}}$, $\overline{\eta}_{\mathrm{air+ins}}$ and f_{ob} as follows.

$$\overline{f}_{\mathrm{ob}} = \overline{\epsilon}\,\overline{\eta}_{\mathrm{air+ins}}\,\overline{f}_{\mathrm{ta}} = \overline{\epsilon}\,\overline{\eta}_{\mathrm{air+ins}}\,k\,f_{\mathrm{ta}} = k\,f_{\mathrm{ob}}\,(\overline{\epsilon}/\epsilon)\,(\overline{\eta}_{\mathrm{air+ins}}/\eta_{\mathrm{air+ins}}) \tag{6.14}$$

Furthermore, f_{ob} is expressed as follows.

$$f_{\mathrm{ob}} = \epsilon_{\mathrm{rigidity}}\mathrm{N_{CD}}f_{\mathrm{CD}} \tag{6.15}$$

where $\mathrm{N_{CD}}$ is T0 high CD number, i.e. 40, 15, 30, and 20 according to numbers in table 2.8 to 2.10 of subsection 2.8.1. In actual calculations, we used equation 6.15 and then did not use f_{ob} and $\epsilon_{\mathrm{rigidity}}$. This can be understood from following equation.

$$\begin{aligned}\overline{f}_{\mathrm{ob}} &= k\,\overline{\epsilon}\,(f_{\mathrm{ob}}/\epsilon)\,(\overline{\eta}_{\mathrm{air+ins}}/\eta_{\mathrm{air+ins}}) = k\,\overline{\epsilon}\,(\mathrm{N_{CD}}f_{\mathrm{CD}}/\epsilon')\,(\overline{\eta}_{\mathrm{air+ins}}/\eta_{\mathrm{air+ins}}) \\ &= k\,(\mathrm{N_{CD}}f_{\mathrm{CD}})\,\overline{\epsilon}_{\mathrm{rigidity}}\,(\overline{\epsilon}'/\epsilon')\,(\overline{\eta}_{\mathrm{air+ins}}/\eta_{\mathrm{air+ins}})\end{aligned} \tag{6.16}$$

where

$$\epsilon' = \epsilon/\epsilon_{\mathrm{rigidity}} = \epsilon_{\mathrm{cuts}} \times \epsilon_{\mathrm{pattern}} \tag{6.17}$$

$$\overline{\epsilon}' = \overline{\epsilon}/\overline{\epsilon}_{\mathrm{rigidity}} = \overline{\epsilon}_{\mathrm{cuts}} \times \overline{\epsilon}_{\mathrm{pattern}} \tag{6.18}$$

Then we have

$$\int \overline{f}_{\mathrm{ob}}\,dE = k\int(\mathrm{N_{CD}}f_{\mathrm{CD}})\,\overline{\epsilon}_{\mathrm{rigidity}}\,(\overline{\epsilon}'/\epsilon')\,(\overline{\eta}_{\mathrm{air+ins}}/\eta_{\mathrm{air+ins}})\,dE \tag{6.19}$$

where E is the kinetic energy of incident particle, and the region of integral should correspond to the rigidity region of 0.7 to 16 GV. Since no antihelium candidate is found, we take 3.0 as the number of antiheliums for the calculation of the 95 % confidence level upper limit. This means that we assume a Poisson distribution with the mean value of 3.0 for the expected number of antiheliums, where zero observed result will be expected at the probability of 5 %. Then we obtain following equation.

$$\int \overline{f}_{\mathrm{ob}}\,dE = 3.0\ (95\ \%\ \mathrm{C.L.}) \tag{6.20}$$

Therefore, we obtain

$$k = \frac{3.0}{\int \mathrm{N_{CD}}f_{\mathrm{CD}}\,\overline{\epsilon}_{\mathrm{rigidity}}\,(\overline{\epsilon}'/\epsilon')\,(\overline{\eta}_{\mathrm{air+ins}}/\eta_{\mathrm{air+ins}})\,dE} \tag{6.21}$$

as the formula of the 95 % C.L. upper limit. Considering this formula, what we need to calculate the upper limit are only f_{CD}, $\overline{\epsilon}_{\mathrm{rigidity}}$, the ratio of $\overline{\mathrm{He}}$ efficiency to He one, and the ratio of $\overline{\mathrm{He}}$ surviving probability to He one. This means we need not calculate the absolute value of $\overline{\epsilon}'$ and ϵ'. Especially if the efficiencies between He and

$\overline{\mathrm{He}}$ are the same, they are canceled so that we may forget them in the calculation. We assume that the efficiencies of various off-line cuts and track trigger pattern efficiencies are the same between He and $\overline{\mathrm{He}}$. Then only $\eta_{\mathrm{air+ins}}$, $\overline{\eta}_{\mathrm{air+ins}}$, $\overline{\epsilon}_{\mathrm{rigidity}}$, and f_{CD} are used in the calculation, and equation 6.21 is simplified to follows.

$$k = 3.0/\int \mathrm{N_{CD}}f_{\mathrm{CD}}\,\overline{\epsilon}_{\mathrm{rigidity}}\,(\overline{\eta}_{\mathrm{air+ins}}/\eta_{\mathrm{air+ins}})\,dE \tag{6.22}$$

Moreover, we have some track trigger modes for each of which the rigidity efficiency is different. Then equation 6.22 is modified to

$$k = 3.0/\int \sum_k \mathrm{N_{CD}}f^k_{\mathrm{CD}}\,\overline{\epsilon}^k_{\mathrm{rigidity}}\,(\overline{\eta}_{\mathrm{air+ins}}/\eta_{\mathrm{air+ins}})\,dE \tag{6.23}$$

where $\overline{\epsilon}^k_{\mathrm{rigidity}}$ is the TT rigidity efficiency of antihelium for the k-th track trigger mode. As seen in the equation, $(\overline{\eta}_{\mathrm{air+ins}}/\eta_{\mathrm{air+ins}})$ is common for all track trigger modes because it is calculated only from cross sections as described in the previous section. For each mode TT rigidity efficiency was evaluated as described in section 6.1 and used in the calculation of the upper limit. Figure 6.16 shows the flux of helium in He T1 trigger mode for (a) BESS '93, (b) '94, and (c) '95 flight data. The open histograms are for the observed flux of heliums divided by $\epsilon_{\mathrm{rigidity}}$ in He T1 trigger mode, i.e., $\mathrm{N_{CD}}f_{\mathrm{CD}}$ in He T1 trigger mode, and the hatched histograms are for $\mathrm{N_{CD}}f_{\mathrm{CD}}\overline{\epsilon}_{\mathrm{rigidity}}$, and the shadowed histograms are for $\mathrm{N_{CD}}f_{\mathrm{CD}}\overline{\epsilon}_{\mathrm{rigidity}}\,(\overline{\eta}_{\mathrm{air+ins}}/\eta_{\mathrm{air+ins}})$ in He T1 trigger mode.

Since $\epsilon_{\mathrm{pattern}}$ was as low as 18 % for BESS '93 flight data, we also utilized the events in the unbiased trigger CD sample which did not pass through TT pattern selection. Although the number of these events cannot be multiplied by $\mathrm{N_{CD}}$ because these events had not been processed by the TT rigidity selection, the number is not negligible in BESS '93 flight data. Then, in order to obtain better limit, we extend equation 6.23 as follows.

$$k = 3.0/\int(\sum_k(\mathrm{N_{CD}}f^k_{\mathrm{CD}}\,\overline{\epsilon}^k_{\mathrm{rigidity}}) + f_{\mathrm{CD}\overline{\mathrm{pat}}})(\overline{\eta}_{\mathrm{air+ins}}/\eta_{\mathrm{air+ins}})\,dE \tag{6.24}$$

where $f_{\mathrm{CD}\overline{\mathrm{pat}}}$ is defined as the flux of He in the unbiased trigger CD sample that did not pass TT pattern selection and passed all off-line cut selections. This equation can be obtained if we assume $(1-\epsilon_{\mathrm{pattern}}) = (1-\overline{\epsilon}_{\mathrm{pattern}})$ and $\epsilon_{\mathrm{cuts}} = \overline{\epsilon}_{\mathrm{cuts}}$, and then consider again in the same way as done in equation 6.21 and 6.22.

Using equation 6.24 combined with all BESS-flight data, the resultant 95 % confidence level upper limit on the $\overline{\mathrm{He}}$/He flux ratio is 2.0 $\times 10^{-6}$ in the rigidity region from 1 to 16 GV at the top of the atmosphere. The numbers used in the calculation of the upper limit are summarized in table 6.4, where E is the kinetic energy of incident helium nuclei, and the region of integral is corresponding to the rigidity region of 0.7 to 16 GV.

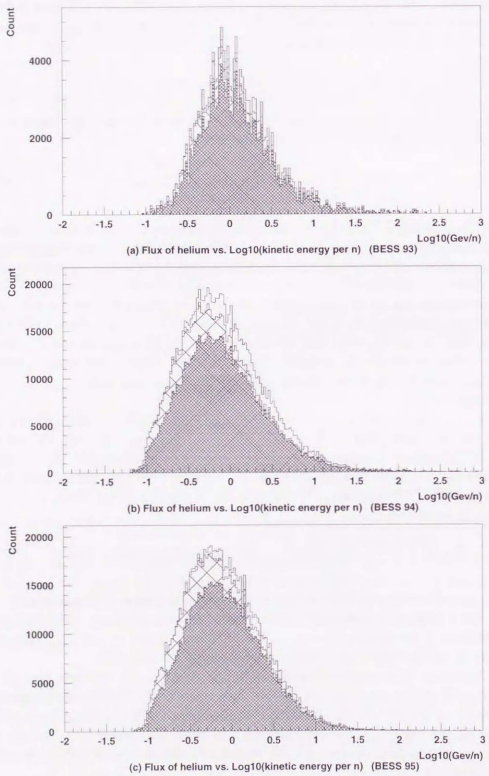

Figure 6.16: Flux of helium in He T1 trigger mode for (a) BESS '93, (b) '94, and (c) '95 flight data, where the open histograms are for $N_{CD} f_{CD}$, the hatched histograms are $\overline{\epsilon}_{\mathrm{rigidity}} \times$ the open histograms, and the shadowed histograms are $(\overline{\eta}_{\mathrm{air+ins}}/\eta_{\mathrm{air+ins}}) \times$ the hatched histograms.

Table 6.4: Summary of the calculation of upper limit.

flight year	T1 mode	N_{CD}	$\int N_{CD} f_{CD} \overline{\epsilon}_{\mathrm{rigidity}}\, dE$	$\int N_{CD} f_{CD} \overline{\epsilon}_{\mathrm{rigidity}} (\overline{\eta}_{\mathrm{air+ins}}/\eta_{\mathrm{air+ins}})\, dE$
'93	$\overline{He}$	40	135,675	117,311
	Multi	40	39,442	33,555
	Not pattern[a]	–	28,141[b]	23,643[c]
'94 first half	$\overline{He}$	15	344,414	285,029
	Not pattern[a]	–	3,679[b]	3,095[c]
'94 last half	$\overline{He}$	30	425,821	352,969
	Not pattern[a]	–	2,043[b]	1,723[c]
'95	$\overline{He}$	20	802,968	669,018
	Not pattern[a]	–	6,534[b]	5,492[c]
Total		–	1,788,716	1,491,833

[a] Not passed the TT pattern selection
[b] $\int f_{CD\overline{pat}}\, dE$
[c] $\int f_{CD\overline{pat}} (\overline{\eta}_{\mathrm{air+ins}}/\eta_{\mathrm{air+ins}})\, dE$

Chapter 7

Results and Discussion:

This chapter provides the results of this work and the discussion. In § 7.1 the results are presented and from section 7.2 to 7.4 the meaning of the results is discussed. In section 7.5 we consider the possible background processes and the rejection strategy using the JET chamber dE/dX information. In the last section, the long duration flights being planned are discussed.

7.1 Results:

The total number of helium nuclei observed in the BESS '93, '94, and '95 flight data is 1.96×10^6 in the rigidity region from 0.7 GV to 16 GV. Since we found no antihelium candidate with a rigidity below 16 GV, only the upper limit can be set using equation 6.24 in this rigidity region. Taking into account the detector efficiencies and the absorption of heliums and antiheliums in the air and the instrument, the resultant 95 % confidence level upper limit on the $\overline{\mathrm{He}}/\mathrm{He}$ flux ratio at the top of the atmosphere is 2.0×10^{-6} in the rigidity range from 1 to 16 GV, which is equivalent to a region from 0.14 to 7 GeV per nucleon in terms of kinetic energy. This result is shown in figure 7.1 and compared with previous limits. As seen in the figure, this work has obtained about a factor of 45 improvement over Golden et al. [27], whose rigidity range is comparable to this work.

The experiments of Golden et al., Badhwar et al. [26], Smoot et al. [24], and Eventson [23] can be all categorized as a "magnetic spectrometer experiment". BESS is also this type of experiment. On the other hand, the data of Buffington et al. [25] were obtained without a magnetic spectrometer. Their instrument was designed to utilize the tracking topology of annihilation in the spark chamber to identify antimatter. Although Buffington's group has been keeping the best limit before our result, this should be viewed cautiously because their antiproton flux measurement using the same instrument is not consistent with a series of experiments carried out recently [18, 19, 20, 49, 50]. Now there seems questions about their evaluation of annihilation efficiency in the instrument, on which their result is essentially based. Then it should be emphasized that this work is the first experiment that reached below 10^{-5} level, and also is performed with the magnetic spectrometer technique.

Except for Buffington's and Golden's groups, none of the previous experiments

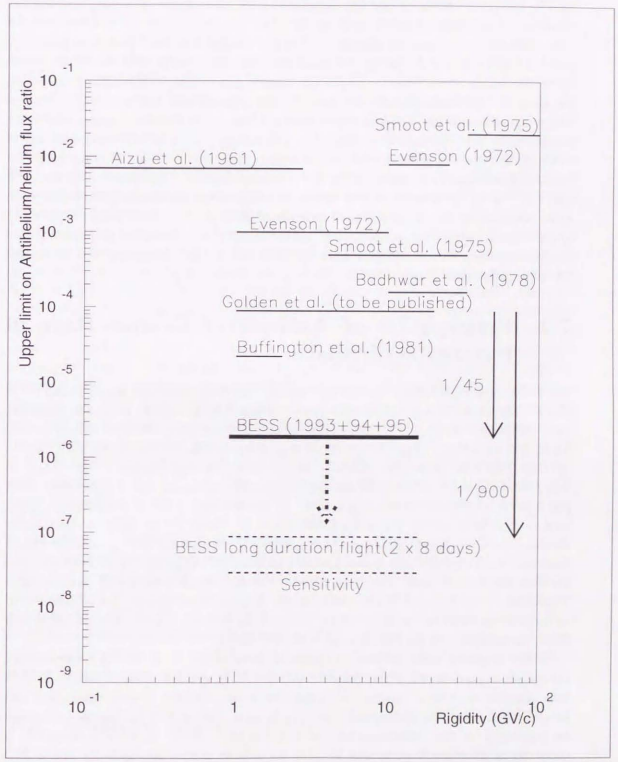

Figure 7.1: The resultant upper limit on the $\overline{\mathrm{He}}/\mathrm{He}$ flux ratio together with previous efforts.

corrected their results for the absorption of matter and antimatter in the atmosphere and in the instruments. From the estimate of the absorption of helium and antihelium in the previous chapter, their upper limits will be from 1.2 to 2 times worse if corrected for the absorption, depending on the thickness of the residual atmosphere and the instruments. As far as the antimatter flux from outside of the solar system is concerned, it is much better to present results after correcting for the absorption, because the residual atmosphere over the instruments and the material of instruments are different for different experiments. However, one of the reasons why these results have been presented without the correction was that the cross sections of antihelium were not precisely known. Recently the cross sections of antiproton has been well measured as mentioned in the previous chapter. Then, assuming the $A^{2/3}$ and $(A_t^{1/3} + A_i^{1/3})^2$ dependence of the cross sections for antimatter, the antihelium cross sections can be estimated with an error of 20 % or less. With such a reasonably good estimate of the cross sections of antihelium, it is preferable that one presents results in a form that is corrected for the absorption: the meaning of the limits can be then understood more clearly.

7.2 Propagation of Antimatter Cosmic Rays in Extragalactic Space:

The leaky box model describes the propagation of the cosmic rays in our Galaxy [52] and well agrees with a series of experiments measuring the cosmic rays. For example, the predictions of the $\bar{p}/p$ ratio by Gaisser and Maurer [65], and by Protheoroe [66] using this model, are in good agreement with the current experiments [18, 19, 20, 49, 50, 21]. The B/C ratio from HEAO-3 experiment [51] also supports the model. In this model the mean amount of matter that cosmic rays pass through between their production and observation is given as 15 g/cm^2, and after a confinement time, cosmic rays leak out to the extragalactic space. Then, if the leaky box model is correct, the intergalactic space may be filled with cosmic rays after a time far longer than the confinement time. Some galaxies have an active nuclei which produces jets accelerating cosmic rays. They can also be the sources of intergalactic cosmic rays. Therefore, if there exists matter-antimatter domain structure in the Universe and antimatter galaxies in the antimatter domains, antimatter cosmic rays may also leak from the antigalaxies and fill the intergalactic space.

If the magnetic field of the extragalactic space is less than 10^{-20} G, the Larmor radius of α-particle with the rigidity of 10 GV is greater than 1 Gpc. In this case, cosmic rays from antidomains can reach our Galaxy directly, and they can be detected. But if the magnetic field is greater than 10^{-20} G, cosmic rays may be scattered by the inhomogeneity of the magnetic field. In such a situation, a question is whether they might be able to diffuse across intergalactic space and enter our Galaxy in the transit time scale which is less than the age of the Universe t_u. Here the diffusion coefficient becomes very important.

The temperature of the intergalactic medium (IGM) affects the diffusion coefficient. Stecker et al. discussed the propagation of extragalactic cosmic rays [47] using

the data of diffuse X ray background from HEAO 1 [46], which showed a possibility that the intergalactic space may be filled with gas whose temperature is 10^8 K. Based on these data they concluded that there is no difficulty for extragalactic particles reaching our Galaxy in a Hubble time from other clusters or superclusters. Now there seems to exist no hot gas among intergalactic space from the data of COBE [44, 45], which give the high-temperature limit of about 10^7 K, based on the distortion of the cosmic microwave background spectrum (the Compton y-parameter). By the traditional Lyα Gunn-Peterson test and an X-ray Gunn-Peterson test, cold temperature of intergalactic medium (IGM) is ruled out [48], where the temperature should be greater than 10^5 K. The traditional Lyα Gunn-Peterson test is based on the fact that neutral hydrogen in the IGM can cause absorption in the spectrum of a quasar blueward of the Lyα emission line. The limit on absorption optical depth is converted into a constraint on the temperature and density of the IGM by determining the neutral hydrogen fraction, assuming ionization equilibrium. On the other hand, an X-ray Gunn-Peterson test is based on the usage of edge and line opacity in the soft-X-ray, i.e., X-ray transitions in heavy elements, which can constrain the IGM at higher temperature than the original Lyα Gunn-Peterson test. Then the temperature of IGM is likely to be between 10^5 to 10^7 K. The mean distance that cosmic rays diffuse in time t_u is $\langle R \rangle \simeq (2Dt_u)^{1/2}$ where $D = (1/3)lv$ is the diffusion coefficient and $t_u \sim 10^{10}$ yr. Since $v \sim 10^{10}$ cm/s, the largest uncertainty lies in the determination of the length scale l. l is of the order of the scale of inhomogeneity of the intergalactic magnetic field, which is not less than the intergalactic particle mean free path. Then $l \geq (n\sigma)^{-1}$, where n is the density of the gas and σ is the cross section in the gas. Because the mean mass density of baryons in the Universe is estimated about 10^{-30} g/cm^3, $n \sim 10^{-6}$ cm^{-3}. In an ionized gas $\sigma \simeq 3 \times 10^{-6} T^{-2} ln(600T/n^{1/3})$, which for $T \sim 10^5 - 10^7$ K and $n \sim 10^{-7} - 10^{-5}$ cm^{-3} gives $l \geq 10^{19} - 10^{25}$ cm. The corresponding lower limits for the diffusion distance $\langle R \rangle$ is then in the range 0.05 to 50 Mpc. Since the radius of cluster is about 10 Mpc, if the magnetic field in the extragalactic space is greater than 10^{-20} G, it cannot be easily determined whether extragalactic particles can reach our Galaxy from other clusters and super clusters. However, this is only the estimate of the lower limits, and then still there is no intrinsic difficulty for extragalactic particles reaching our Galaxy from other clusters and super clusters. Even if in the future the magnetic field in the extragalactic space is measured as greater than 10^{-20} G and $\langle R \rangle$ is determined as much less than 10 Mpc, the search for cosmic antihelium will be still important, because it could lead to a discovery of the superconducting strings in our Galaxy or very exotic phenomena near the Earth.

7.3 Galactic Modulation:

The existence of galactic winds has been discussed by many people. If the galactic winds of our Galaxy is so strong, the cosmic rays in the intergalactic space can not enter our Galaxy. Matthew and Baker [55] have found that the absence of interstellar matter in elliptical galaxies could be explained by the existence of spherical galactic

winds powered by supernova explosions. They also argued that spiral galaxies are less likely to be able to support galactic winds because of their deeper gravitational potential well. Faber and Gallagher [56] have considered the existence of winds in spiral galaxies and noted the difficulty of constructing wind models in these galaxies. Bregman [57] has concluded that a total wind from the disk of our Galaxy is not possible, although a partial wind may exist. Chevalier and Oegerle [58] concluded that supernovae energy is more likely to be dissipated by radiative cooling than by galactic wind.

While there is very little direct evidence to support or rule out a galactic wind in our Galaxy, there were several attempts to estimate it indirectly using certain models. Jones [59] has adopted the dynamical halo model of Jokipii [60] and concluded that the convection velocity V of our Galaxy is 8 km/s. Similar results were obtained by Kota and Owens [61] (from 9 to 17 km/s). Webber et al. [63] concluded that a galactic wind convection velocity is less than 20 km/s from the study of propagation of cosmic rays in our Galaxy. Leche and Schlickeiser [62] have considered the state transport or relativistic electrons subject to diffusion, convection, and radiation losses in disk galactic winds. By applying their results to the radio observations of edge-on galaxies, Leche and Schlickeiser were able to deduce parameters corresponding to winds in our Galaxy. Their value of $V = 7.8$ km/s was in good agreement with the other estimates given above.

Concerning the galactic wind, at this time the only model which enables quantitative predictions is the dynamical halo model. If the dynamical halo model is valid, one would expect that extragalactic cosmic rays at low energy would be repulsed by galactic wind. Assuming the same parameters as Jones used, extragalactic cosmic rays with energy less than $\sim$ 770 MeV/n (for $A/Z = 2$) would be in the convection-dominated regime, where the diffusion coefficient is no longer the determining parameter and the convection is dominated. Then extragalactic cosmic rays with such low energy would be efficiently swept out of the Galaxy. Thus, for example, the $\overline{\mathrm{He}}$/He upper limit of the calorimeter experiment carried out by Buffington, Schindler, and Pennypacker [25] might apply only to the sources in our Galaxy, because their energy band for He was 130 $\sim$ 370 MeV/n near the Earth. In the region of energy from 0.14 to 7 GeV/n, the accessibility, which is defined as the ratio of the extragalactic cosmic rays at the center of the Galaxy and those in the extragalactic space, varies from about 0 % to 50 %. Then, assuming that the spectrum shape of antihelium is the same as that of helium, the attenuation of the extragalactic antiheliums by the galactic modulation is at most about 1/10 in this energy region. Therefore, it is concluded that an increase of the sensitivity of antihelium search by an order of magnitude would compensate for the effect of the galactic wind.

7.4 Antimatter in Extragalactic Space around our Galaxy:

Using some crude arguments on energies, one can estimate that leakage from normal galaxies would produce an extragalactic cosmic-ray component with a flux $(I_{\mathrm{ex}}/I_{\mathrm{gal}})_{\mathrm{NG}} = \xi_{\mathrm{NG}} \sim 10^{-4} - 10^{-5}$ [53, 54]. For active galaxies, these estimates yield a higher value: $\xi \sim 10^{-3}$. If the attenuation of extragalactic cosmic rays by galactic wind is taken in account, this becomes $\xi \sim 1/10 \times 10^{-3}$, from the discussion described in the previous section. Therefore, if the half of extragalactic cosmic rays are antimatter and they pass through 15 g/cm^2 interstellar medium before the observation, the flux ratio of $\overline{\mathrm{He}}$/He would be about $0.5 \times 0.5 \times 10^{-4} = 2.5 \times 10^{-5}$ near the Earth, where the second factor of 0.5 is obtained from similar consideration of the absorption cross section of antihelium as described in the previous chapter. Concerning the solar modulation, the solar wind may not change the flux ratio, assuming that the spectra shapes of antihelium and helium are the same.

The above discussion is based on very rough arguments. Nevertheless, if this discussion is correct, it is very interesting because this work sets 2.0×10^{-6} as the upper limit on the $\overline{\mathrm{He}}$/He flux ratio at the top of atmosphere. This means that BESS is the first experiment that is sensitive to the signal from the extragalactic space, and that less than 10 % of extragalactic cosmic rays are antimatter components. Taking into account what are mentioned in section 7.2, if the magnetic field of the extragalactic space is less than 10^{-20} G, there exists no antidomain within 1 Gpc $\sim t_u \times c$, where t_u is the age of the Universe and c is the velocity of light.

7.5 Background consideration:

In this section the background processes which may fake antihelium and then decrease the efficiency will be considered. In addition, a study of JET $\mathrm{d}E/\mathrm{d}X$ for particle identification is described.

First, we categorized the background processes into the following two cases:

i) Helium spillover

Heliums with high rigidity spillover onto the negative rigidity side due to the finite resolution of the rigidity measurement. These events can be suppressed if stricter track quality cuts are applied but it will degrade the selection efficiency as mentioned in section 5.9. This background can also be suppressed if the resolution of the rigidity measurement is improved. The new JET chamber, which is now being designed, is expected to have an improved rigidity resolution by increasing the number of sense wires. This will contribute to a further rejection of these spillover background events, and will also extend the observable energy range to a higher region.

ii) Negative muons/pions/electrons

The only weak point of the BESS detector is the material thickness of the magnet, that is 4 g/cm^2 per wall. The rigidity of an incident particle is measured in the central tracking detector inside the magnet. On the other hand, the charge of the incident particle is measured by the dE/dX of the TOF counter outside the magnet. But what happens between the central tracking detector and the TOF counter can not be monitored. This means that the measured charge in TOF counter can not be associated directly to the particle which made the track in the central tracking detector, even though the track is extrapolated to the TOF counter and the matching of the hits and the track is confirmed in the analysis.

If more than one particles hit the same scintillator while only one of them passes through the tracking detector, the measured dE/dX can be larger than expected. If both top and bottom scintillators have such accidental hits, negative particles with charge = 1 can fake antihelium. Or what is more likely to happen is that a particle with charge = 1 interacts in both top and bottom scintillators. For these background events, much stricter β and dE/dX cuts should be applied. In the future long duration flight, where eight-day exposure will be expected for one scientific flight, this kind of background events will become a serious problem. In such a situation, the most reasonable solution is to identify particle's charge by the dE/dX of the JET chamber. Then the charge information of particles can be directly associated to the track in the JET chamber.

We tried to calibrate the JET chamber dE/dX information for '95 flight data. The dE/dX is calculated from the charge measured in each wire of the JET chamber and the path length. For the JET chamber, the number of the charge measurement points is equivalent to the $N_{r\phi fit}$ or less, and at each point the dE/dX can be calculated. We applied a truncated mean method in which lower 15 % and higher 45 % of measured dE/dX values are removed and the rest of the measured dE/dX values are used to calculate the mean dE/dX. This effectively removes the well known Landau tail effect in the dE/dX distribution.

However, after the first trial of rough calibration of the JET chamber dE/dX, it was found that a space charge effect degrades the resolution, particularly in the high charge region. Figure 7.2 shows the plot of the JET dE/dX versus the rigidity for one-run data of the BESS '95 flight after the rough calibration. The theoretical values for muon/electron, proton, deuteron, and helium are indicated in dashed lines. As seen in the figure, data for the helium events are much lower than the theoretical value and the separation of particles with charge = 1 and particles with charge = 2 is almost impossible.

This effect, where the observed charge is saturated, can be explained in the following way: The initially arriving electrons, which make the first avalanche in the strong electrical field near the wire, shield and weaken the electrical field so much that the rest of the drifting electrons cannot make avalanches efficiently. As a result, the observed charge values are saturated, i.e., the measured charge of particle by the JET chamber becomes smaller than expected.

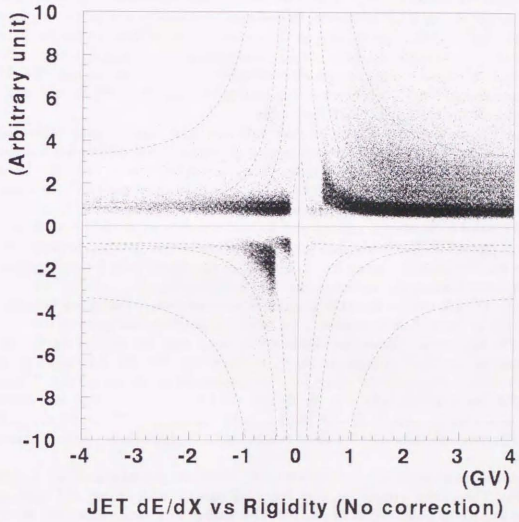

Figure 7.2: JET dE/dX vs. rigidity for BESS '95 flight data (No correction).

After an exhaustive study of the effect, it turned out that the degree of the saturation greatly depends on the inclination of the track towards the z-direction. It was found that, if the track of incident particle is perpendicular to the z axis the ionized charge density, which is expressed as the charge per unit length along the wire, is higher than the track inclined. Then the degree of the saturation becomes larger for the perpendicular tracks. In other words, as the ionized charge density per unit length along z increases, the degree of the saturation increases. Moreover, the effect depends on the ionized charge value itself because the initial drift-charge becomes larger as the charge itself increases. In addition, it turned out that the degree of the saturation slightly depends also on the inclination of the track in the $r\phi$-plane. This is caused by variations of the charge density along the drifting direction. After all, we have the three parameters (track-inclination towards the z-direction "TKIZ", measured charge "MQ", and track-inclination in $r\phi$-plane "TKIP") to correct the saturation of the charge in the JET chamber.

Pure helium and proton samples were extracted and used to make calibration functions depending on the three parameters. First a dE/dX calibration function of "TKIZ" and "MQ" was obtained by fitting to the data as a two-dimensional function. Since the "TKIP" dependence is smaller than the other two parameters, it was fitted as a simple one parameter calibration function later. The result of the JET dE/dX versus the rigidity plot for one-run data of the BESS 95 flight is shown in figure 7.3. The theoretical values for muon/electron, proton, deuteron, and helium are indicated in dashed lines. As seen in the figure, data for each particle species are well along the corresponding theoretical curves.

If the dE/dX cut for top TOF counter is loosened, where the upper boundary of the cut in figure 5.26 is removed, we have two potential background events in BESS '95 flight data. These two events are in run 8 and run 19, and the dE/dX values of the top TOF counter are shown in figure 7.4. The dE/dX values of the bottom TOF counter and $1/\beta$ values for these two events are shown in figure 7.5 and figire 7.6, respectively. As seen in the figures, the two potential background events give values that are consistent with particles with charge > 1. Then we have made the calibration functions only for these two-run data to check these two background events.

For the check, we utilized two data samples which are named proton and helium samples. The proton sample includes events of particle with charge = 1, and the helium sample includes events of particle with charge = 2, being extracted by the preselection, TOF dE/dX, and β selections. To ensure the good quality of the JET dE/dX, the number of charge measured points in the JET chamber, N_{hit}, should be greater than 12. The cut positions for N_{hit} for both the proton and helium samples are shown in figure 7.7.

The JET chamber dE/dX distributions after the N_{hit} cut for both the proton and helium samples for the rigidity region from 5 to 8 GV are shown in figure 7.8. The open histogram is for the proton sample and the shadowed histogram for the helium sample. As shown in the figure, the particle identification without the JET chamber dE/dX makes mis-identifications for some events of particle with charge = 1, which is seen as the shadowed histogram inside the open histogram. This means

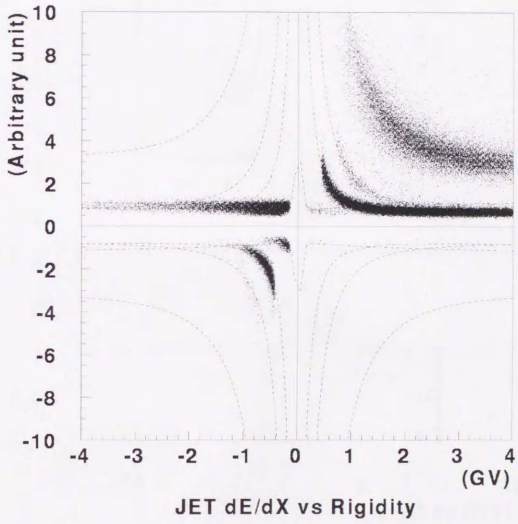

Figure 7.3: JET dE/dX vs. rigidity for BESS '95 flight data.

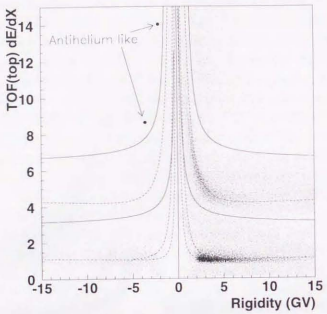

Figure 7.4: Two potential background events in TOF(top) dE/dX vs. rigidity plot ('95).

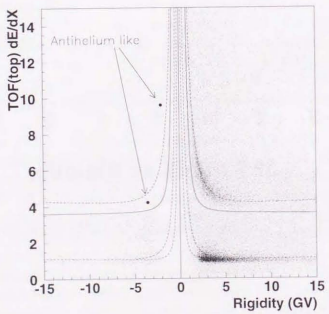

Figure 7.5: Two potential background events in TOF(bottom) dE/dX vs. rigidity plot ('95).

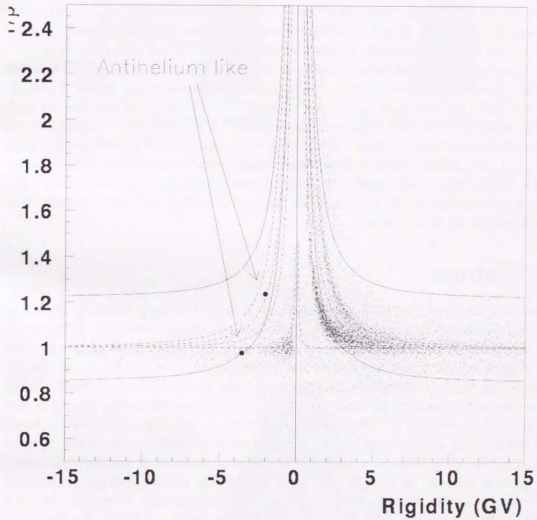

Figure 7.6: Two potential background events in $1/\beta$ vs. rigidity plot ('95).

that some protons or muons/pions/positrons are identified as heliums by the TOF dE/dX and β selections.

In the rigidity region from -16 to -1 GV, which is the region of antihelium search, the JET chamber dE/dX distribution after the same N_{hit} cut for all data of run 8 and run 19 is shown in figure 7.9. The two potential background events are denoted as a shadowed histogram. As shown in the figure, the two background events are identified as particles with charge = 1 clearly. Then no antihelium candidate is found in the two-run data of BESS '95 flight, even when the TOF dE/dX cut is loosened. In '93, '94, and '95 flight data, all of potential background events are checked with the loose dE/dX cuts which were mentioned in section 6.2 of chapter 6, and we found no antihelium candidate even with such loosen TOF dE/dX cuts.

In this stage of the antihelium search in BESS, the JET chamber dE/dX is not necessary because the current identification method described in chapter 5 is sufficient and the high efficiency should not be sacrificed for the JET chamber dE/dX cut. However, the new JET chamber, which is now being designed, is expected to be free from the space charge effect. Then if the new chamber is installed and the high efficiency of N_{hit} cut is confirmed, we expect that the identification by the chamber dE/dX will be utilized efficiently. Because the electron/muon/pion background will be much more serious in the long duration flights planned in the future, the chamber dE/dX will be an essential tool.

7.6 Future:

A sensitivity level of 3 $\times 10^{-8}$ can be achieved with two long duration flights of eight days each when combined with envisaged improvements in the efficiencies. This sensitivity is shown in Figure 7.1 along with the upper limit obtained from these flights, which is about a factor 900 improvement over Golden et al. As far as the background is concerned, it seems possible to reach this sensitivity level, because no serious source of background has been observed in the course of the analysis of '93, '94 and '95 flight data, and even at this higher sensitivity level, those background events that might start to come in will be efficiently rejected by the particle identification with the dE/dX measurement of the JET chamber. The rejection strategy described in the previous section will be furthermore studied by the first long duration flight. According to the discussion in section 7.4, this sensitivity level corresponds to 5 $\times 10^{-3}$ of the upper limit on the $\overline{He}/He$ flux ratio in the extragalactic space just around our Galaxy.

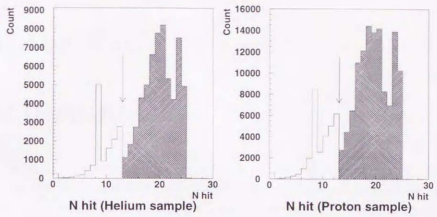

Figure 7.7: Cut position of N_{hit} for JET dE/dX.

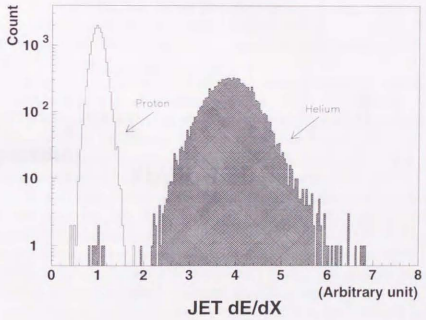

Figure 7.8: JET dE/dX for BESS '95 flight data (5 GV < *rigidity* < 8 GV).

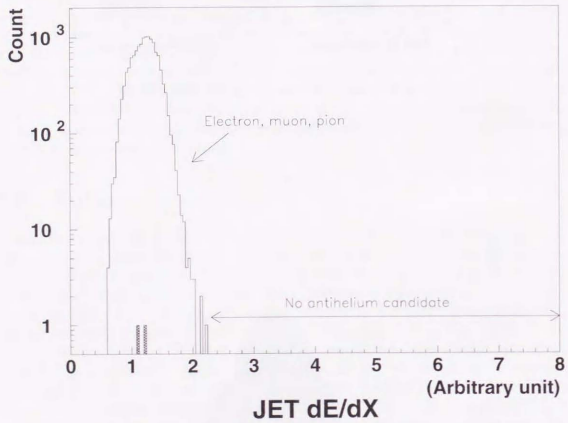

Figure 7.9: JET dE/dX for BESS '95 flight data (-16 GV < *rigidity* < -1 GV).

Chapter 8

Conclusions

This dissertation describes the search for antihelium in cosmic rays by the analysis of the data obtained from the three balloon flights of BESS[1] which were performed in 1993, 1994, and 1995. In the analysis, events with a single track in the tracking chamber were selected and identification of heliums and antiheliums were based on the measurements of magnetic rigidity, time of flight, and energy loss in the plastic scintillators. The selected events were further checked on the quality of data, especially the tracking qualities, and also on the consistency among the responses from the different detectors. After these careful checks and the quality requirements, no antihelium candidate was found below rigidity of 16 GV. Taking into account the detector efficiencies and the absorption of antiheliums and heliums in the air and the instrument, this analysis sets a 95% confidence level upper limit on the $\overline{\mathrm{He}}/\mathrm{He}$ flux ratio of 2.0 $\times 10^{-6}$ at the top of the atmosphere in the rigidity region from 1 to 16 GV, which is equivalent to a region from 0.14 to 7 GeV per nucleon in terms of kinetic energy. This result is about a factor of 45 improvement over the previous best limit by Golden et al.

From this result, if the magnetic field of the extragalactic space is less than 10^{-20} G and the flux ratio of (extragalactic cosmic rays)/(galactic cosmic rays) is about 10^{-3}, it is concluded that there exists no matter-antimatter domain structure within 1 Gpc $\sim t_u \times c$, assuming the dynamical halo model, where t_u is the age of the Universe and c is the velocity of light. If the magnetic field of the extragalactic space is greater than 10^{-20} G, whether cosmic rays can reach our Galaxy depends on the temperature and density of the gas in the extragalactic space, which have not been well measured yet, and then it cannot be determined from our result whether matter-antimatter domain structure exists beyond the scale of 10 Mpc. However, even in such a situation, the detection of antihelium might mean the existence of the superconducting strings in our Galaxy or very exotic phenomena near the Earth. Then further search for antihelium should be encouraged.

It is noted that a sensitivity level of 3 $\times 10^{-8}$ can be achieved with two long duration flights of eight days each when combined with envisaged improvements in the efficiencies. As far as the background is concerned, it seems possible to reach this sensitivity level, because no serious source of background has been observed in

[1] Balloon-borne Experiment with a Superconducting magnet rigidity Spectrometer

the course of the analysis of '93, '94 and '95 flight data, and even at this higher sensitivity level, those background events that are negative muons/pions/electrons will be efficiently rejected by the particle identification with the dE/dX measurement of the JET chamber. If the flux ratio of (extragalactic cosmic rays)/(galactic cosmic rays) is about 10^{-3}, this sensitivity level corresponds to the upper limit on the $\overline{\mathrm{He}}$/He flux ratio of 5×10^{-3} in the extragalactic space near our Galaxy, assuming the dynamical halo model.

Acknowledgments

I wish to extend my sincere gratitude to Professor S. Orito who has led the BESS experiment, for his guidance in my studies, especially for his giving me the great opportunity to join the experiment. I also wish to gratefully acknowledge A. Yamamoto who has managed the experiment and led it to a success. The analysis were done owing a lot to Prof. S. Orito and K. Anraku. I would like to thank them for their suggestions and helpful discussions at the various stages of the analysis.

I would like to thank all the other BESS colleagues for their effort to make a success of the experiment, especially M. Nozaki, M. Imori, T. Yoshida and K. Yoshimura for their overall contributions; I. Ueda, H. Matsunaga, M. Motoki, N. Takimi, H. Matsumoto, T. Sanuki, and M. Otoba for their excellent works on the experiment. D. Righter is also thanked for his professional technical support. I wish to acknowledge the contributions to the analysis from I. Ueda, H. Matsunaga, M. Motoki, T. Sanuki and Y. Nishihara. I am also indebted to Y. Makida, K. Tanaka, M. Kimura, and the other staffs who have worked on the superconducting magnet; to J. Suzuki, Y. Higashi, Y. Ajima, S. Koizumi, and all the other KEK staffs who contributed to the construction of the BESS instruments; and to K. Shimamura, T. Haga, T. Tsunoda, and all the other people who was once involved in the experiment. It is a pleasure to express my appreciation to J. Ormes, R. Streightmatter, J. Mitchell, N. Yajima, T. Yamagami, R. Golden, and B. Kimbell who were the collaborators of the experiment.

At last, but not least, I am grateful to the balloon campaign team from the National Scientific Balloon Facility for their professional and excellent work in carrying out the BESS flights, and to International Center for Elementary Particle Physics of University of Tokyo for kindly allowing me to use their workstations. I also thank the people in Lynn Lake for their kind hospitality during our stay in Canada. The presented analysis were performed on RS/6000 workstations supplied by IBM Japan, Ltd. under their "Partnership Program." The BESS experiment was supported by Monbusho International Scientific Research Grant and Scientific Research Grant, Kurata Research Grant, and Sumitomo Research Grant.

References

[1] P. A. M. Dirac, Theory of electron and positrons, Nobel Lecture, (Dec. 12, 1933).

[2] C. D. Anderson, The production and properties of positrons, Nobel Lecture, (Dec. 12, 1936).

[3] O. Chamberlain, The early antiproton work, Nobel Lecture, (Dec. 11, 1959).

[4] D. E. Dorfan, Phys. Rev. Lett. **14**, 1003 (1965).

[5] T. Massam, Nouvo Cimento **39**, 10 (1965).

[6] Y. M. Antipov, Soviet J. Nucl. Phys. **12**, 171 (1971).

[7] M. G. Albrow, Nucl. Phys. B **97**, 189-200 (1975).

[8] H. Albrecht, Phys. Lett. B **157**, 326 (1985).

[9] R. W. Brown and F. W. Stecker, Phys. Rev. Lett. **43**, 315 (1979).

[10] K. Sato, Phys. Lett. B **99**, 66 (1981).

[11] I. Affleck and M. Dine, Nucl. Phys. B **249**, 361 (1985).

[12] A. Dolgov and J. Silk, Phys. Rev. D **47**, 4244 (1992).

[13] E. Witten, Nucl. Phys. B **249**, 557-592 (1985).

[14] G. Steigman, Ann. Rev. Astron. Astrophys. **14**, 339 (1976).

[15] F. W. Stecker, Nature **273**, 493 (1978).

[16] F. W. Stecker, Nucl. Phys. B **252**, 25-36 (1985).

[17] Y. T. Gao, F. W. Stecker, et al., Astrophys. J. **361**, L37-L40 (1990).

[18] R. L. Golden et al., Phys. Rev. Lett. **43**, 1196 (1979).

[19] E. A. Bogomolov et al., Proc. 20th Intern. Cosmic Ray Conf. (Moscow), **2**, 72 (1987).

[20] E. A. Bogomolov et al., Proc. 21th Intern. Cosmic Ray Conf. (Adelaide), **3**, 288 (1990).

[21] K. Yoshimura et al., Phys. Rev. Lett. **75**, 3792 (1995).

[22] H. Aizu et al., Phys. Rev. **121**, 1206 (1961).

[23] P. Evenson, Astrophys. J. **176**, 797-808 (1972).

[24] G. F. Smoot, A. Buffington, and C. D. Orth, Phys. Rev. Lett. **35**, 258 (1975).

[25] A. Buffington, S. M. Schindler, and C. R. Pennypacker, Astrophys. J. **248**, (1981) 1179.

[26] G. D. Badhwar, R. L. Golden et al., Nature **274**, 137 (1978).

[27] R. L. Golden et al. (to be published); R. L. Golden et al., *Proceedings of the 3rd Workshop on BESS*, KEK, Japan, Feb. 24-25 (1992), Editor A. Yamamoto, 3.

[28] A. Yamamoto et al, IEEE Trans. on Magnetics **24**, 1421 (1988).

[29] T. Massam CERN 76-21 (1996)

[30] M. Imori, et al. IEEE Transactions on Nuclear Science **39**, 1389

[31] T. Saeki et al., NIM A, 506-514 (1995)

[32] M. Goossens *ZEBRA manual* (1991)

[33] V. Karimäki, Report of University of Helsinki, HU-SEFT-1991-10.

[34] J. R. Letaw, R. Silberberg and C. H. Tsao, Astrophys. J. Supp. **51**,271(1983)

[35] V. F. Kuzichev, Yu. B. Lepikhin and V. A. Smirnitsky, Nucl. Phys. A **576**,581-602 (1994)

[36] V. F. Afonasiev et al., Yad. Fiz. **47**, 1656-1662 (1988)

[37] K. Nakamura et al., Phys. Rev. Lett. **52**, 731 (1984)

[38] V. F. Afonasiev et al., Yad. Fiz. **40**, 34-42 (1984)

[39] A. S. Carrol et al., Phys. Lett. B **80**, 319 (1973)

[40] S. P. Denisov et al., Nucl. Phys. B **61**, 62(1973)

[41] J. C. Allaby et al., Yad. Fiz. **12**, 538-556 (1970)

[42] H. L. Bradt, B. Peters, Phts. Rev.**77**,54(1950); **80**,943(1950)

[43] T. F. Cleghorn, P. S. Preier, C. J. Wadington, Can. J. Phys. **46**,572(1968)

[44] E. L. Wright, J. C. Mather, et al. Astrophys. J. **420**,450-456 (1994)

[45] J. C. Mather, E. S. Cheng, et al. Astrophys. J. **420**,439-444 (1994)

[46] F.E.Marshall, E.A.Boldt, S.S.Holt, R.B.Miller, R.F.Mushotzky, L.A.Rose, R.E.Rothschild, and P.J.Serlemitsos, Astrophys. J. **235**,4-10(1980)

[47] F.W.Stecker, R.J.Protheroe, and D.Kazanas, Astrophysics and Space Science **96**, 171-177 (1983).

[48] Thomas Aldcroft, et al. Astrophys. J. **437**,584-596 (1994)

[49] M. H. Salamon et al., Astrophys. J. **349**, 78 (1990).

[50] S. J. Stochaj, Ph. D. thesis, Univ. of Maryland, (1990)

[51] J. J. Engelmann et al., Astron. Astrophys. **233**, 96-111 (1990).

[52] V. S. Berezinskii, S. V. Bulanov, V. A. Dogiel, V. L. Ginzburg (ed.), and V. S. Ptuskin, "Astrophysics of Cosmic Rays," Amsterdam, North-Holland (1990).

[53] V. L. Ginzburg and S. I. Syrovatskii, "Origin of Cosmic Rays," Pergamon Press, London (1964).

[54] S. Hayakawa, "Cosmic Ray Physics," Wiley & Sons, New York (1969).

[55] W. G. Matthews and J. C. Baker, Astrophys. J. **170**, 241 (1971).

[56] S. M. Faber and J. S. Gallagher, Astrophys. J. **204**, 365 (1976).

[57] J. Bregman, Astrophys. J. **224**, 768 (1978).

[58] R. A. Chevalier and W. R. Oegerle, Astrophys. J. **227**, 398 (1979).

[59] F. C. Jones, Astrophys. J. **229**, 747 (1979).

[60] J. R. Jokipii, Astrophys. J. **208**, 900 (1976).

[61] J. Kota and A. J. Owens, Astrophys. J. **237**, 814 (1980).

[62] I. Lerche and R. Schlickeiser, Astrophys. J. **239**, 1089 (1980).

[63] W. R. Webber, M. A. Lee, and M. Gupta, Astrophys. J. **390**, 96 (1992).

[64] M. M. Shapiro and R. Silberberg, Astrophys. J. **265**, 570 (1983).

[65] T.K. Gaisser, and R.H. Maurer, Phys. Rev. Lett. **30**, 1264 (1979).

[66] R. J. Protheroe, Astrophys. J. **251**, 387 (1981).

[67] E. O. Abdrahmanov et al., Z. Physik C, Particles and Fields 5, 1-8 (1980)

[68] N. S. Grigalashvili et al., Yad. Fiz. **48**, 476-482 (August 1988)